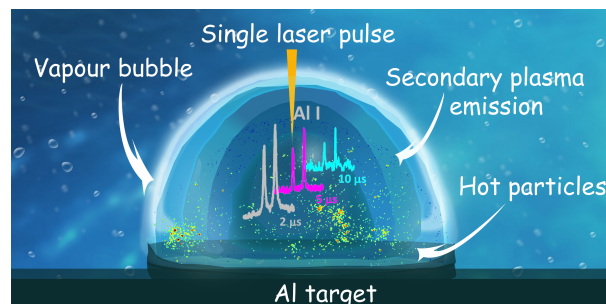


UNIVERSITY OF BELGRADE
SCHOOL OF ELECTRICAL ENGINEERING

Marijana R. Gavrilović

Interplay of cavitation bubble and plasma emission during single pulse laser induced breakdown on submerged target

Doctoral Dissertation



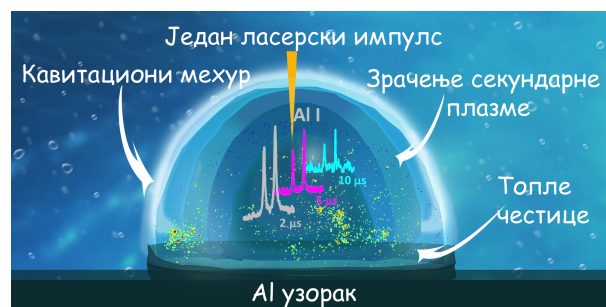
Belgrade, 2017.

УНИВЕРЗИТЕТ У БЕОГРАДУ
ЕЛЕКТРОТЕХНИЧКИ ФАКУЛТЕТ

Маријана Р. Гавриловић

Узајамно дејство кавитационог мехура и
зрачења плазме код пробоја индукованог
једним ласерским импулсом на мети у
течности

Докторска дисертација



Београд, 2017.

Committee members

PhD Jovan Cvetić, thesis advisor

Professor

School of Electrical Engineering, University of Belgrade

PhD Petar Matavulj,

Professor

School of Electrical Engineering, University of Belgrade

PhD Marko Cvejić

Research Associate Assistant

Institute of Physics, University of Belgrade

Day of the defense:

To my parents...

Firstly, I would like to express my sincere gratitude to my thesis supervisor professor Jovan Cvetić and my thesis committee professor Petar Matavulj and dr Marko Cvejić for the knowledge having been communicated and help in improving the final version of this thesis.

Special thanks to dr Sonja Jovićević, who introduced me into the world of the experimental physics, and underwater plasma in particular and who conceptualised the experiment presented in this thesis.

My sincere thanks go to my dear colleagues from the laboratory of the Plasma Spectroscopy and Lasers at the Institute of Physics, University of Belgrade: dr Miliwoje Ivković, Vladimir Simjanović, Stanko Milanović, Milica Vinić and Biljana Stankov, for the help in my work and inspirational discussions.

It has been a great honour for me to cooperate closely with acad. Nikola Konjević, on which I'm very grateful.

Helpful discussions with dr Violeta Lazic and advices obtained during the course of the investigations presented here, are greatly acknowledged

Thanks to my friends for the appreciation and support. Last, but not least, thanks to my family for unselfish support.

Marijana R. Gavrilović

Belgrade, March 2th, 2017.

Желела бих да изразим искрену захвалност ментору докторске дисертације професору Јовану Цветићу и члановима Комисије професору Петру Матавуљу и др Марку Цвејићу на пренесеном знању и помоћи да ова дисертација добије свој финални облик.

Посебно се захваљујем др Соњи Јовићевић која ме је увела у свет експерименталне физике, нарочито у свет плазме у води и која је осмислила експеримент представљен у овој дисертацији.

Искрено се захваљујем драгим колегама из Лабораторије за Спектроскопију Плазме и Физики Ласера Института за Физичку, Универзитета у Београду, др Миливоју Ивковићу, Владимиру Симјановићу, Станку Милановићу, Милици Винић и Биљани Станков на помоћи у раду и инспиративним дискусијама.

Велика ми је част што сам имала прилике за блиску сарадњу са академиком Николом Кођевићем, на чему сам веома захвална.

Велику захвалност исказујем др Виолети Лазић на корисним дискусијама и саветима у току трајања овог истраживања.

Захваљујем се пријатељима на разумевању и подршци. И на крају, захваљујем се својој породици на несебичној подршци

Маријана Р. Гавриловић

Београд, 02. март 2017.

Interplay of cavitation bubble and plasma emission during single pulse laser induced breakdown on submerged target

Abstract

Although the experimental setup needed for the plasma and cavitation bubble creation with the laser is relatively simple, enormous variety of physical processes take place in this experiment, covering the topics from fluid dynamics, to heat and mass transfer, to chemical reactions, plasma physics and light emission. Laser induced plasma (LIP) shows a wide range of characteristics depending on the experimental parameters used for its creation. In addition to the complexity of the LIP itself, when such a plasma is created inside the liquid environment several extra factors come into play, making both the experimental and theoretical investigation highly challenging tasks. In a liquid environment, besides plasma formation due to the laser action, the shock wave and cavitation bubble are created, all of them sharing the input laser energy. Due to the interrelation of the phenomena occurring after laser induced breakdown (LIB) in liquid environment, shock wave, bubble and plasma emission, in order to get real insight into the physics of the processes, one need to study more than one effect at the same time.

In this study main focus was on the last two aspects of the LIB, i.e. cavitation bubble and plasma emission, while the subject of the shock wave emergence and propagation was also discussed in short. The mutual impact of these two extremely interesting phenomena, laser produced plasma and the cavitation bubble, is considered very important for numerous applications, the production of nanoparticles being one of the more popular recently. Cavitation bubble plays a crucial role in determining the size, shape and chemistry of the products of laser ablation in liquid. Although its importance have been recognized and many research groups are dealing with this topic, a lots of speculations about the role of the cavitation bubble in nanoparticles production still exist. Another point on which the opinions about the cavitation bubble are divergent regards the question of double pulse laser induced breakdown spectroscopy (DP-LIBS). Plasma-bubble relations in DP-LIBS are still not very well documented, while the relation between the plasma and bubble in sin-

gle pulse laser induced breakdown spectroscopy (SP-LIBS) are almost completely missing.

In this work precisely those intermediate time scales in SP LIBS at which the bubble starts to appear and the plasma radiation is present, ranging from nanoseconds to millisecond, were studied by several experimental methods. Plasma was studied using the fast photography and optical emission spectroscopy (OES), the shock wave propagation was recorded with the Schlieren technique and cavitation bubble evolution was captured using shadowgraphy and probe beam techniques. In underwater single pulse laser ablation of alumina and aluminium, a long lasting optical emission of several hundreds of μs duration was detected for the first time. Duration of emission on the pure aluminium coincided with the first bubble cycle, while on the alumina further prolonging of optical emission was detected and it was explained through the material related properties. Based on the unique observations of the glowing particles inside the cavitation bubble on aluminium and thin glowing layer in contact with the target on alumina, the temperature of the bubble was estimated to be more than 1000 K throughout the whole bubble lifetime. In the early phases of the bubble evolution it's temperature was determined from the molecular AlO bands and it was around 4000 K, which agrees well with the theoretical models.

Besides having extremely long durations, plasma obtained in this study shows another particular feature, namely it is evolving in the two characteristic phases. The LIBS spectra from the secondary plasma contain the lines from low excited levels and have a good quality, with very narrow transitions almost free of the continuum component. Using these findings it is recommended to record plasma emission after delay of 1–2 μs . Important conclusion is that with the proposed experimental approach, SP LIBS detection of underwater plasma is feasible both on metallic and ceramic samples, also by using a not gated and a relatively cheap detector. In the process of the sustaining and detecting the plasma emission the role of the cavitation bubble proved to be the of unique importance.

Keywords:

SP LIBS, underwater plasma, cavitation bubble, OES

Scientific field: Electrical and Computer Engineering

Research area: Nanoelectronics and Photonics

UDC number: 621.3

Узајамно дејство кавитационог мехура и зрачења плазме код пробоја индукованог једним ласерским импулсом на мети у течности

Резиме

Експериментална поставка потребна за стварање плазме и мехура у води релативно је једноставна, али је разноврсност физичких процеса који се одигравају у овом експерименту огромна, обухватајући поља од динамике флуида, преноса топлоте и масе, хемијских реакција, физике плазме и емисије светлости. Ласерски произведена плазма ЛПП може имати широк спектар карактеристика у зависности од коришћених експерименталних параметара. Поред сложености саме ЛПП, када се таква плазма формира унутар течности, неколико додатних фактора постаје релевантно, што чини и теоријска и експериментална истраживања изазовним задатком. У течном окружењу, поред формирања плазме долази и до формирања ударног таласа и кавитационог мехура од којих сваки процес троши део енергије. Услед међусобне повезаности ових појава, како би се добио прави увид у физику процеса, потребно је проучавати више процеса истовремено.

У овом раду главни акценат истраживања је на кавитационом мехуру и зрачењу плазме, док је питање појављивања ударног таласа и његовог простирања дискутовано у кратким цртама. Узајамно дејство ова два веома интересантна феномена, ласерски произведене плазме и кавитационог мехура, веома је важно за велики број примена, од којих је у последње време производња наночестица најпопуларнија. Кавитациони мехур има пресудну улогу у одређивању величине, облика и хемије производа ласерске аблације у течности. Иако је важност мехура препозната и многе истраживачке групе се баве овом тематиком и даље постоји доста нејасноћа око улоге кавитационог мехура у производњи наночестица. Друга тема око које такође постоје неслагања око кавитационог мехура је спектроскопија ласерски индукованог пробоја са два ласерска импулса. (ДП ЛИБС). Односи између плазме и мехура у ДП ЛИБС-у још увек нису довољно документовани, док је такав однос код ласерског пробоја једним импулсом (СП

ЛИБС) апсолутна непознаница.

У овом раду проучаване су управо те временске скале код СП ЛИБС на којима се мехур појављује, а зрачење плазме још увек постоји, од микро до мили секунди, помоћу више експерименталних техника. Плазма је проучавана помоћу брзе фотографије и оптичке емисионе спектроскопије, ударни талас помоћу шлирен методе док је еволуција кавитационог мехура разлучена уз помоћ шадографије и техника са пробним снопом. У подводној аблацији алумине и алуминијума, први пут је детектована дуготрајна оптичка емисија трајања од неколико стотина микросекунди. Трајање зрачења на чистом алуминијуму се поклапа са првим циклусом мехура, док је код алумине детектовано даље продужење емисије које је објашњено преко особина материјала мете. На основу јединствених опажања светлећих честица унутар мехура на алуминијуму и танког светлећег слоја у контакту са метом од алумине, процењено је да је температура у мехуру већа од 1000К током читавог првог циклуса еволуције мехура. У раним фазама еволуције, температура мехура одређена је из алуминијум оксид молекулских трака и износи око 4000К, што је у складу са резултатима теоријских модела.

Поред екстремно дугог живота плазме још једна нова карактеристика плазме је откривена, наиме плазма се развија у две фазе. СП ЛИБС спектар секундарне плазме садржи линије које потичу са побуђених стања ниских енергија и имају добар квалитет, јер су детектоване линије готово без континуумске компоненте. Користећи ова сазнања препоручено је снимање емисије плазме са кашњењем од 1–2 микросекунде. Важан закључак је да је са предложеним експерименталним приступом, могућа СП ЛИБС детекција под водом и на металним и на керамичким узорцима, чак и уз коришћење релативно јефтиних детектора без опције временског одабира. У процесу одржавања плазме и детектовања њеног зрачења, улога кавитационог мехура се показала као изузетно битна.

Кључне речи: СП ЛИБС, плазма под водом, кавитациони мехур, ОЕС

Научна област: Електротехничко и рачунарско инжењерство

Ужа научна област: Наноелектроника и фотоника

УДК број: 621.3

Contents

List of Figures	xiii
1 Introduction	1
1.1 Cavitation bubble	2
1.2 General aspects of the laser induced plasma	3
1.3 Mutual impact of the cavitation bubble and plasma emission	5
2 Laser beam propagation in the liquid environment	7
2.1 Influence of matter on laser light propagation	7
2.2 Applications	11
3 Shock wave production and bubble formation	17
3.1 Laser induced shock wave	17
3.1.1 Physics of shock waves	18
3.1.2 Techniques of studying shock waves in LIB	19
3.2 Cavitation bubble	20
3.2.1 Process of cavitation	20
3.2.2 Simple model of spherical bubble dynamics	22
3.2.3 Laser induced bubble on a solid target	26
3.2.4 Interaction of light with bubbles	29
4 Plasma formation in liquid ambient	32
4.1 Plasma creation through the LIB	33
4.2 Properties of the laser produced plasma in liquid environment	39
4.2.1 Optical emission spectroscopy of laser-induced plasmas in liquid (LIBS)	40

5	Experimental techniques for underwater Laser Induced Breakdown diagnostics	44
5.1	Fast imaging techniques	47
5.1.1	Plasma imaging	47
5.1.2	Shadowgraphy and Schlieren techniques	47
5.2	Transmission and scattering with the probe beam	49
5.3	Optical emission spectroscopy (OES)	50
5.4	Data acquisition and processing	52
 6	 Results	 55
6.1	Plasma evolution	55
6.2	Bubble dynamics	62
6.2.1	Plasma and bubble relations	62
6.2.2	Optical effects of the laser induced bubble	63
6.2.3	Bubble sizing	68
6.2.4	Probe techniques for investigation of the bubble's dynamic	70
6.3	Shock wave propagation	78
6.4	Optical emission spectroscopy results	78
6.4.1	Primary plasma phase	79
6.4.2	Secondary plasma phase	86
6.5	Influence of the target material on the laser induced breakdown in liquid medium	94
 7	 Conclusion	 100
	Bibliography	105
	Biography	129
	List of publications	130

List of Figures

1.1	Scheme of the physical processes associated with optical breakdown	2
1.2	Main stages occurring during the LIB on submerged target	3
2.1	Interaction of light with medium	8
2.2	Reflection and refraction	9
2.3	Optical properties of the water	10
2.4	On site trials on the Mediterranean Sea	15
2.5	Deep sea in-situ multi-element chemical analysis	16
3.1	Schematic of a spherical bubble in an infinite liquid.	22
3.2	Influence of the target shape on the bubble evolution	28
3.3	Collapsing bubble and jet formation	28
3.4	Different scattering regimes depending on the particle size	30
4.1	Dependence of the LIB on submerged target on the focusing conditions	38
4.2	Initiation of plasma by laser and subsequent relaxation and recombination	41
5.1	Optimizing the focusing conditions	45
5.2	Photograph of the interaction chamber and the target holder	46
5.3	Experimental setup for fast imaging techniques	48
5.4	Experimental setup for probe techniques	49
5.5	Experimental setup for OES with lens	50
5.6	Wavelength calibration of the Jarrel-Ash spectrometer with the mounted iCCD camera	51
5.7	Intensity calibration	51
5.8	Example of the image cropping	53
5.9	Spectral data manipulation	53

LIST OF FIGURES

6.1	Fast photography of plasma evolution in air and water	56
6.2	Fast photography of plasma evolution	57
6.3	GUI for plasma integral intensity calculations	59
6.4	Gain calibration	60
6.5	Temporal dependence of integral plasma intensity	60
6.6	Early plasma decay	61
6.7	Position of the maximum intensity plasma region	62
6.8	Superimposed images of plasma photography and shadowgraphy-pure Al.	64
6.9	Superimposed images of plasma photography and shadowgraphy-alumina.	64
6.10	Bubble and plasma size relation	65
6.11	Optical effect of the bubble	66
6.12	Formation of the glare circle from the N=3 rays	66
6.13	Steps in determining bubble size	68
6.14	Size determination for bubbles with irregular shapes	69
6.15	Output of the procedure for the bubble sizing	69
6.16	Probe beam techniques on alumina sample	71
6.17	Transmission techniques on aluminium sample	72
6.18	Scattering technique on aluminium sample	73
6.19	Transmission with the slit	74
6.20	Transmission with the slit – explanation	75
6.21	Calibrated scatter for calculating the bubble size	76
6.22	Images of the shock wave on Al target obtained using the Schlieren technique	78
6.23	Overall spectra on alumina with fitted continuum contribution	79
6.24	Illustration of the continuum component for the pure Al target	80
6.25	GUI for the continuum subtraction and temperature evaluation based on the Planck’s law	81
6.26	Absence of line emission in primary plasma phase on aluminium	82
6.27	H $_{\alpha}$ and oxygen I emission in the first plasma phase on the alumina	83
6.28	Example of the H $_{\alpha}$ line fit and determined N $_e$	84
6.29	Example of the oxygen I line fit and determined N $_e$	87
6.30	Temperature determination from vibrational AlO band	87
6.31	Determination of the temperature inside the bubble	88
6.32	Temporal evolution of vibrational temperature	89

LIST OF FIGURES

6.33	Spectra from the secondary plasma phase on the pure Al target . . .	90
6.34	Intensity and SNR evolution of the excited species on the pure Al . .	91
6.35	Spectra in the secondary plasma phase from the impurities in alumina	92
6.36	Long lasting emission of the secondary plasma	93
6.37	Plasma evolution on different targets	95
6.38	Comparison of LIBS emission in primary plasma phase on two differ- ent materials	96
6.39	Images of the shock wave on alumina target obtained using the Schlieren technique	97
6.40	Bubble evolution on different targets	97
6.41	Bubble size on different materials	98
6.42	Comparison of LIBS emission in secondary plasma phase on two dif- ferent materials	99
7.1	Graphical comparison of the timescale of LIB processes	102
7.2	Sketch of the processes occurring after LIB on the Al target	103

Chapter 1

Introduction

While the subject of a laser produced plasma is relatively new area of the research dating from the invention of the laser in 1960, cavitation bubble has been in the research focus almost two centuries. This lasting interest in the dynamics of the cavitation bubbles follows from the early recognition of the potential damage caused by the cavitation bubble collapse and destruction of pressure pipes, hydraulic machineries and turbine structures due to the presence of the bubbles in liquid. Relevance of both research fields dramatically increased with the widespread use of the lasers in medicine(Niemz, 2004,2007),(Vogel and Venugopalan, 2003)(Shangguan *et al.*, 1997) especially in ophthalmology(Vogel, 1998)(Kennedy, 1995)(Kennedy *et al.*, 1995). Although the experimental setup needed for the plasma and cavitation bubble creation with the laser is rather simple, enormous variety of physical processes take place in this simple experiment, covering the topics from fluid dynamics, to heat and mass transfer, to chemical reactions, plasma physics and light emission. Scheme of the physical processes associated with laser induced breakdown (LIB) on the tissue is given in the Fig.1.1, where the fraction of the input energy spent on the different processes is given in the percents, while the typical timescale at which these events occur on as solid target is given in the Fig. 1.2

Due to the interrelation of the phenomena occurring after LIB in liquid environment, shock wave, bubble and plasma emission, in order to get real insight into the physics of the processes, one need to study more than one effect at the same time. In this study main focus was on the last two aspects of the LIB, i.e. cavitation bubble and plasma emission, while the subject of the shock wave emergence and propagation was also discussed in short. In the following, brief overview of the research dealing with one of the phenomena of interest in this study (cavitation bubble or

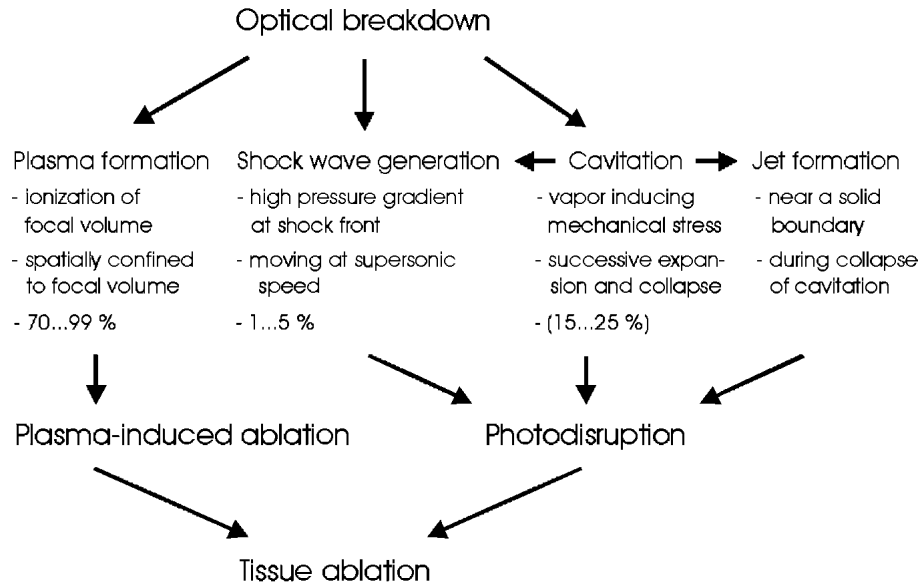


Figure 1.1: Scheme of the physical processes associated with optical breakdown(Niemz, 2004,2007)

plasma) is given in sect.1.11.2, while in the sect.1.3 the research where both effects are simultaneously considered is reviewed.

1.1 Cavitation bubble

Interest in the cavitation bubble dynamics arose due to their destructive effects on the solid surfaces, and it was studied first by lord Rayleigh(Rayleigh, 1917) in an effort to explain the damage of propellers of high speed boats and submarines. Acoustic cavitation has been an important area of research as a potential candidate responsible for kidney stone comminution and tissue damage in shock-wave lithotripsy (SWL).(Zhong *et al.*, 2001) High intensity sound can induce cavitation in the soft tissue and bubbles formed in this way can affect to a great extent the distribution of the ultrasound energy. It is of crucial importance to understand the behaviour of these bubbles in order to improve the quality of results of medical ultrasound in clinics.

To study the cavitation erosion laser produced bubbles are employed frequently (Isselin *et al.*, 1998)(Vogel *et al.*, 1989)(Takada *et al.*, 2010) due to the ease of production and different attainable sizes. Severity of the damage produced by the bubble is determined by its collapse phase in which the micro jet and collapse shock wave can be formed, and it depends on the parameter $\gamma=d/R_{max}$, where d is the distance between initial location of the bubble center and the wall and the R_{max} is

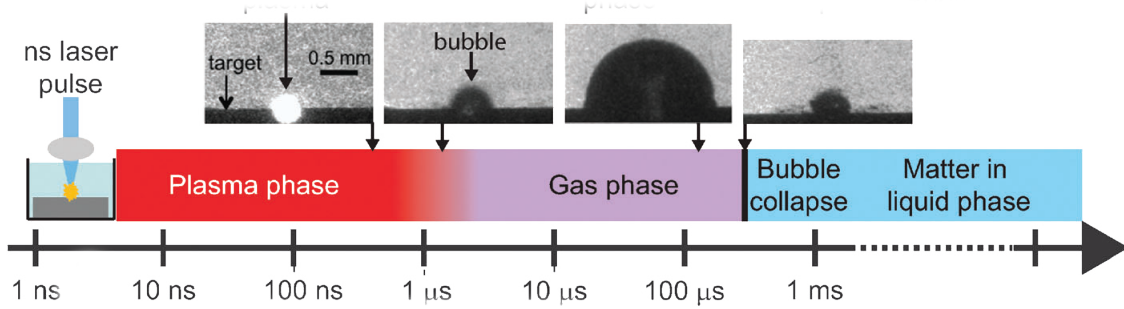


Figure 1.2: Main stages occurring during the LIB on submerged target, (Lam *et al.*, 2014)

the maximum bubble radius. General understanding of the bubble behaviour is useful for characterisation and identification of underwater explosions using seismic and/or acoustic signature based on spherical models of explosion bubbles. (Krieger and Chahine, 2005). Cavitation in the liquid has also been used for control of nanoparticles synthesis with the ultrasound. (Bang and Suslick, 2010) Studies of bubbles in liquid are crucial for explaining the striking phenomena of sonoluminescence, discovered relatively recently and studied intensively from then on. (Gaitan and Holt, 1999) (Brenner *et al.*, 2002) (Margulis and Margulis, 2006) (Chu *et al.*, 2009) Although the majority of application include cavitation in the water, bubble dynamics in other liquids has also been studied. In (Jomni *et al.*, 2009) bubble dynamics in viscous liquids used for electrical insulators for high voltage applications were studied. Comparison of bubble formation by laser in water and different types of alcohol is given in (Kovalchuk *et al.*, 2010). Encapsulated gas microbubbles found applications in medical ultrasound as contrast agents for imaging and as a therapeutic tool for drug delivery. (Delale (Ed.), 2013) More applications of the laser produced cavitation bubble are given in the Chap.2.2

1.2 General aspects of the laser induced plasma

Laser induced plasma (LIP) shows a wide range of characteristics depending on the experimental parameters used for its creation. Influence of the laser wavelength, energy, pulse duration (Bai *et al.*, 2013), (Detalle *et al.*, 2003) focusing conditions and the focal spot size (Ohata *et al.*, 2002), different background gases (Harilal *et al.*, 2006) (De Giacomo *et al.*, 2012), target materials (Hwang *et al.*, 1991) on plasma formation and properties are in addition intertwined, increasing the complexity of experimental studies. Large variety of experimental parameters that can be changed

are at the same time the advantage and the drawback of the LIP. On the plus side, by changing some or all parameters listed above, plasmas of significantly different conditions can be obtained. As a drawback, it is hard to perform any systematic comparison between the results of different research groups, and hence to pinpoint the influence of one specific parameter when, at the same time, large number of them are affecting plasma's behaviour.

Due to the large potential for variations of experimental parameters, LIP is not studied thoroughly and its properties are still interesting topic for many investigations. Its transient nature with complex propagation of the ablation plume into the background gas,(Harilal *et al.*, 2002)(Harilal *et al.*, 2003)(Wen *et al.*, 2007a)(Wen *et al.*, 2007b) where electron number density and temperatures change very fast, make hard to obtain the same quality of experimental results as in the case of the arcs or some other well studied plasma source. But, on the other hand, it enables excitation of almost all elements in periodic system, which are hard to introduce in conventional plasma sources. Furthermore, by using time resolved studies, range of electron number density and temperatures that can be obtained in LIP is larger than with any other source of plasma radiation, which lead to the large popularity of LIP as a source for Stark parameters measurements. (Cvejić *et al.*, 2013)(Cirisan *et al.*, 2014)(Cvejić *et al.*, 2014) Plasma created by short and intense laser radiation focused on a solid, liquid or gaseous sample is the essence of the laser induced breakdown spectroscopy (LIBS) technique. Plasma emission detected after passing through some dispersing element, enables determination of elements present in the material without any sample preparation and with quite simple experimental configuration which is the main advantage of LIBS.

Due to the numerous applications of the LIBS technique , a lot of research is going on in this area, which resulted in several books on the subject(Cremers and Radziemski, 2006)(Miziolek *et al.*, 2006)(Singh and Thakur, 2007)(Noll, 2012)(Musazzi and Perini, 2014). Still, as pointed out in several review papers(Konjević *et al.*, 2010)(Hahn and Omenetto, 2010)(Hahn and Omenetto, 2012)(Gaudiuso *et al.*, 2010)(Fortes *et al.*, 2013), great deal of research is devoted purely to the applications, while the research of fundamentals of the technique is lagging behind. This is partially, a consequence of the extreme complexity of the laser induced breakdown (LIB) in media and extremely short timescales on which the events are occurring after laser action.

1.3 Mutual impact of the cavitation bubble and plasma emission

In addition to the complexity of the LIP itself, when such a plasma is created inside the liquid environment several extra factors come into play, making both the experimental and theoretical investigation extremely complicated. In a liquid environment, besides plasma formation due to the laser action, the shock wave and cavitation bubble are created, all of them sharing the input laser energy. Formation of the shock waves happens also in the gaseous surrounding, but these mechanical effects of the laser action are more pronounced when the interaction is occurring in the liquid. Although the cavitation bubble was detected in some experiments performed in the gaseous hydrogen(Kielkopf, 2000), the cavitation bubble is usually considered to be the unique property of the LIB in the liquid. The mutual impact of these two extremely interesting phenomena, laser produced plasma and the cavitation bubble, is considered very important for numerous applications, some of which are listed in the Sect. 2.2. Recently the most emphasized is the production of nanoparticles by laser ablation in liquid, during which the cavitation bubble plays a crucial role in determining the size, shape and chemistry of the products. (Yang, 2012)(Amendola and Meneghetti, 2013)DellAglio *et al.* (2015)(Ibrahimkutty *et al.*, 2015)(Sasaki and Takada, 2010). Although its importance have been recognized and many research groups are dealing with this topic, a lots of speculations about the role of the cavitation bubble in nanoparticles production still exist. Another point on which the opinions about the cavitation bubble are divergent regards the question of double pulse laser induced breakdown spectroscopy (DP-LIBS). DP-LIBS is applied both in the gaseous and liquid surrounding, but its importance in liquids is tremendous. Namely, the first laser pulse in liquid or target in liquid, serves to produce the cavitation bubble as a more suitable gaseous surrounding inside which the second laser pulse is then sent after certain delay.(Nyga and Neu, 1993)(Michel and Chave, 2008) (Pu and Cheung, 2003). Depending on the conditions inside the cavitation bubble, the quality of the spectra obtained after the second laser pulse differs, and thus it is necessary to optimize the delay between the pulses and the spatial alignment of the beams, so as to obtain the largest enhancement of the useful signal. (Cristoforetti *et al.*, 2012)(Lazic *et al.*, 2013a)(De Giacomo *et al.*, 2007). Plasma-bubble relations in DP-LIBS are still not very well documented, while the relation between the plasma and bubble in single pulse laser induced breakdown

spectroscopy (SP-LIBS) are almost completely missing. Example to the contrary is the study of the very early times of bubble appearance in (Tamura *et al.*, 2015), where the authors compared the plasma-bubble relations for two different pulse durations. Possible explanation for the lack of the studies of interplay of the cavitation bubble and plasma emission in SP-LIBS is short plasma duration, as usually quoted in the literature.(De Giacomo *et al.*, 2007)

In this work precisely those intermediate time scales at which the bubble starts to appear and the plasma radiation is present, ranging from nanoseconds to millisecond, will be studied by several experimental methods. The structure of the thesis is as follows. In the Chapter 2 brief overview of the light-liquid interaction is given and some applications where laser-liquid interact are listed. Chapter 3 gives short theoretical background on the phenomena of the shock wave and cavitation bubble, with little accent on the specific case of the laser produced shock wave and bubble. In the Chapter 4 characteristic of the breakdown in pure liquid and on a submerged target are closely examined and implication on the optical emission spectroscopy of such plasmas are explained. In the chapter 5 complete description of all experimental methods used in this study is given, and in the Chapter 6 the results of different applied techniques are laid out and compared. At the end, in Chapter 7 the conclusions are given.

Chapter 2

Laser beam propagation in the liquid environment

Matter can act on light (electromagnetic radiation in general) in manifold ways. Light propagation through the media can be affected by three main mechanisms: reflection and refraction, absorption, and scattering. These mechanisms of interaction will be described in the following, with special emphasis on the specifics of the water impact on the light propagation. Besides, they are also relevant during interactions of light with cavitation bubbles which are described in Sections 3.2.4 and 6.2.2. At higher values of energy density, e.g. when focused laser beam propagates through the medium, the breakdown and plasma formation occurs. Plasma formation is accompanied by shock wave emergence and cavitation bubble formation in the case of the water (or any other liquid) as a propagation medium. In these situations, it can be stated that interaction is going in the opposite direction, namely light acts on the matter and induces changes inside of it. These phenomena are described in Sect.3 and Sect. 4.

2.1 Influence of matter on laser light propagation

When laser beam propagates through any type of medium, it suffers several types of losses inside of it. Which of the losses - reflection, absorption, or scattering is dominant determines the type of medium and the laser wavelength. The sketch of the ray of light interacting with the slice of matter is given in Fig.2.1

Reflection – Reflection is defined as the returning of electromagnetic radiation by surfaces upon which it is incident.(Niemz, 2004,2007). According to the simple

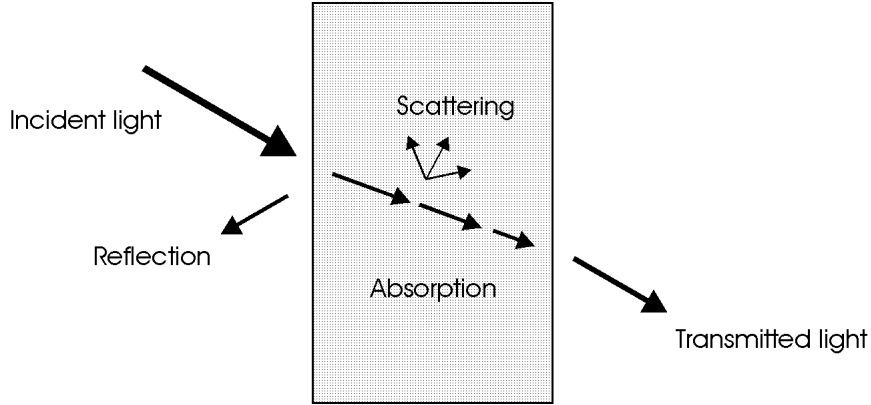


Figure 2.1: Mechanisms of light interaction with the medium during its propagation, (Niemz, 2004,2007)

law of reflection, the wave normals of the incident and reflected beams and the normal of the reflecting surface all lie within the plane of incidence. It also applies that the reflection angle is equal to the angle of incidence $\theta = \theta'$, see Fig.2.2.

Refraction – Refraction is the consequence of the different propagation speeds of light wave in different media and it occurs on the surfaces which separate two media of different index of refraction, see Fig. 2.2. The correlation between the angles in the reflection is given by the Snell's law

$$\frac{\sin\theta}{\sin\theta''} = \frac{v'}{v''} \quad (2.1)$$

where θ'' is the angle of refraction, and v and v' are the speeds of light in the media before and after the reflecting surface, respectively. Since the corresponding indices of refraction can be related to the propagation speed through the relations $n=c/v$ and $n'=c/v'$ the Snell's law 2.1 can be written in different form

$$n\sin\theta = n'\sin\theta'' \quad (2.2)$$

Total reflection will occur when $\sin\theta > n'/n$.

Absorption – Absorption arises due to the partial conversion of light energy into heat motion of the molecules of the absorbing material, which results in decreasing intensity of an incident light beam. If light propagates through the perfectly transparent medium no absorption will occur. Opposite of the transparent are opaque media, inside which the incident radiation is almost completely absorbed. Of course, not a single material is completely transparent or completely opaque. In addition, those properties depend very strongly on the wavelength of the incident radiation.

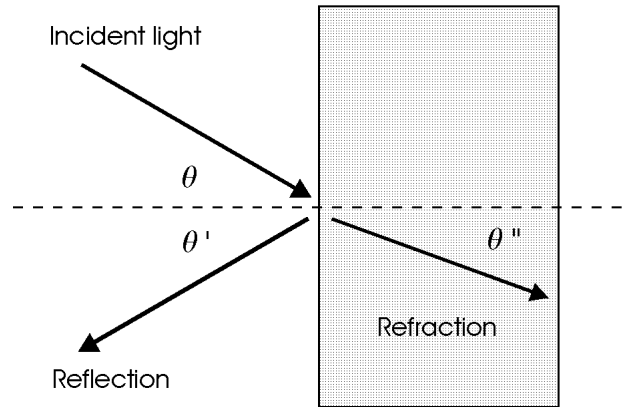


Figure 2.2: Reflection and refraction of the incident beam,(Niemz, 2004,2007)

The ability of a medium to absorb the radiation is usually expressed through the Beer-Lambert law

$$I(z) = I_0 \exp(-\alpha z) \quad (2.3)$$

where z denotes the optical axis, $I(z)$ is the intensity at a distance z , I_0 is the incident intensity and α is the absorption coefficient of the medium.

Scattering – Scattering is occurring when frequency of the electromagnetic radiation impinging on the elastically bound charged particles doesn't correspond to the natural frequencies of particles. Resulting forced vibration will have the same frequency and direction as that of the electric force of the incident wave, but with much smaller amplitude compared to the case of the resonance, i.e. the same frequencies. In addition, the phase of the forced vibrations is different, which causes the photon to slow down when penetrating into denser medium. Two types of scattering can be distinguished, elastic and inelastic, depending if the part of the incident photon energy is converted during the process. One of the forms of the elastic scattering, in which the photon doesn't change its energy, is Rayleigh scattering which is inversely proportional to the fourth power of wavelength.(Niemz, 2004,2007) In order that the Rayleigh scattering be valid, the scattering particles must be smaller than the wavelength of the light. If the size of the scattering particles becomes comparable with the wavelength Mie scattering occurs. Mie scattering and geometrical optics approximation is frequently used to describe the scattering of light by bubbles and it is mentioned briefly in Sect.3.2.4

Looking again the Fig. 2.1, only the photons that have not undergone reflection

and absorption, and forward scattered photons can be detected on the other side of the slice. In the case of LIBS on submerged target this implies that only the portion of the laser energy actually reaches the target, while large part of the input energy is spent on the optical path through the liquid. Wavelength of the input radiation is extremely important parameter, since it determines the index of refraction and absorption and scattering coefficients. This is illustrated on the example of the water as one of the most commonly used liquid in underwater LIBS and almost all laser material processing applications, see Fig. 2.3. If using the laser with the wavelength inside the water transmission window, which lies in the blue-green spectral region, the penetration depth of the laser beam in clear water can be ~ 10 m. (Musazzi and Perini, 2014).

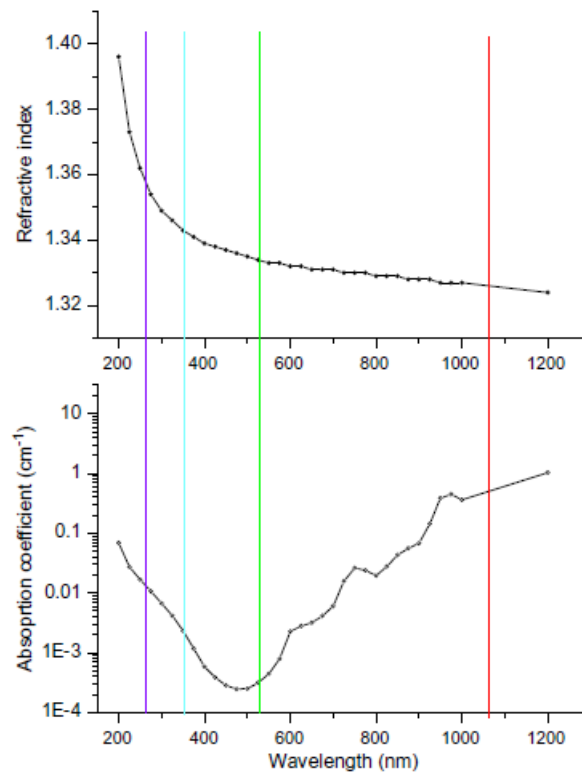


Figure 2.3: Refractive index (top) and absorption coefficient (bottom) of pure water at room temperature and pressure as a function of wavelength; the vertical lines indicate the wavelengths of Nd:YAG laser: 1064 nm (red), 532 nm (green), (Lazic and Jovićević, 2014)

By observing the wavelength dependence of water absorption it can be concluded that the absorption is the highest in the infrared part of the spectrum, which makes this wavelength favourable for the plasma formation on the water surface. On the other side, in order to decrease the losses of laser energy in the water it is neces-

sary to use the shortest possible optical paths. When choosing the optical paths and suitable optics one has to bear in mind that focal length of the lenses increases inside the water due to its higher refractive index (~ 1.33) compared to the air ~ 1 . In real applications however, the water is not of the highest purity and there are always suspended particles and gas bubbles present which scatter the light strongly, making the use of long range in underwater applications impossible. For example, frequently studied is the sea water which contains sea salts in part per million (ppm) concentrations. These concentrations for the visible light don't have an influence on the absorption or refraction, but increase the molecular scattering significantly (Lazic and Jovićević, 2014) thereby decreasing the beam transmission and aggravating the plasma formation. This also occurs in natural waters which are rich with the inorganic particulates and different types of organic materials with sizes in the range from $0.1 \mu\text{m}$ to $100 \mu\text{m}$ (from small colloids to large phytoplanktons). Since they scatter the incoming light strongly, general recommendation is to work with the shortest possible optical paths in turbid water. The scattering coefficient decreases with water pressure and grows with its temperature. In laser surgery it is very important to know the absorbing and scattering properties of the tissues in order to perform optimally. Knowledge of the refraction index is usually necessary when applying the laser radiation on the highly reflective surfaces. The refractive index determines the overall reflectivity and it is usually wavelength dependent only in the regions of high absorption. Scattering on the other hand, can scale universally with the fourth power of wavelength (Niemz, 2004,2007). Important thing to remember when performing LIBS measurements in the water is to correct the detected spectrum for the wavelength dependent absorption of the water before determining the plasma parameters from it.

2.2 Applications

Application in which the laser beam propagates through the liquid are numerous, and some of them are described in the following. Several main groups of applications are elaborated, namely medical, nanoparticles production, material processing, material characterisation, environmental ecological and marine applications.

Medical applications

One of the main causes for huge interest in the area of laser induced breakdown LIB in liquid is the ophthalmic surgery, which started to develop since 1980s mainly for cataract surgery or for relieving intraocular pressure as a treatment for glaucoma, see (Hammer *et al.*, 1997) and references therein. Numerous studies have been devoted to understand and quantify LIB in ocular media, not only because of the application but also due to the potential ocular damage.(Kennedy *et al.*, 1997) Great deal of the research was devoted to determination of the breakdown threshold with nanosecond and picosecond pulses at 1064 nm, motivated by their use in ophthalmology These wavelengths are favoured since they don't dazzle the patient, they are well transmitted in the eye, and they possess the minimal risk to the retinal damage since the absorption coefficient of the retinal pigment epithelium is small. (Vogel, 1997) In the following years, the transition towards the shorter laser pulses is continued to the femtosecond regime, in order to minimize the collateral tissue damage and obtain the same surgical effect with the lower threshold pulse energies (Heisterkamp *et al.*, 2002)(Nuzzo *et al.*, 2010), but nanosecond and picosecond laser pulses are still in use in clinical practice.

After the ophthalmology, one of the oldest medical applications of the laser is in the dentistry, but with much less success, and discussions about its usefulness is still going on, where possible enhancement of the results can be expected with the use of very short pulse durations(Muoz *et al.*, 2010). One of the most significant disciplines for laser application is gynecology, since the CO₂ lasers have proven to be very effective in removing unnecessary cervical tissue. In urology CO₂ laser is also very frequently applied for high precision cutting, while argon ion and Nd:Yag lasers are used for the coagulation of highly vascularized tumors or malformations. Nd:Yag lasers are in addition the most common choice in lithotripsy and photo dynamic therapy.

Besides the studies on the breakdown threshold, the physical after effects produced by the LIB were intensively studied for all pulse durations, since they largely determine the degree of the tissue damage. These after effects include plasma, shock wave, bubbles, jets etc.(Vogel *et al.*, 1990) (Vogel *et al.*, 1996)(Docchio and Sacchi, 1988)(Vogel and Venugopalan, 2003) (Niemz, 2004,2007). Studies of the underlying mechanisms of the bubble and plasma formation during laser action on the tissue are very useful when determining optimal parameters of the laser for the specific applications. For example, bubbles in absorbing liquids and on submerged targets were investigated in the context of controlled drug delivery with microsecond laser

pulses.(Shangguan *et al.*, 1998) or to estimate the damage on the tissue during the laser microsurgery *in vivo*.(Hutson and Ma, 2007)

More extensive list of the different laser applications in medicine can be found in (Niemz, 2004,2007)

Nanoparticles production

Laser ablation in the liquid as a route for nanoparticles (NPs) production is experiencing increasing popularity over the last two decades. Number of publications on the subjects also speaks in the favour of this statement.(Barcikowski *et al.*, 2009) Production of different types of NPs and use of different experimental conditions during the production is described extensively in the recent book(Yang, 2012). Also several review articles give excellent overview of the current achievements of the technique (Zeng *et al.*, 2012)(Sasaki and Takada, 2010)(Venugopal Rao *et al.*, 2014)(Barcikowski and Compagnini, 2013) It can be seen from the literature survey that this method of the NPs production is quite versatile, clean or so called "green" process and particles produced by ablation in a liquid are free of chemical side products or specific ligands which can compromise the further applications of NPs.(Salminen, 2013) But, at the same time, there remain a lot of unknowns about the process, leaving place for improvement of the efficiency and yield, by gaining insight into the physics of the underwater ablation. In recent years, the lot of attention was devoted to the use of femtosecond laser for NPs production. Complexity of the parameters governing the femtosecond laser ablation efficiency for nanoparticles production is discussed in (Menéndez-Manjón *et al.*, 2011)(Povarnitsyn *et al.*, 2013). The importance of the optimal focusing and liquid levels is emphasized for maximum ablation rate, while several factors which complicate the optimization of the process, e.g. self-focusing, vaporization of liquid, refraction at the air-liquid boundary and optical breakdown in the liquid are analysed. The general recommendation of the authors of (Menéndez-Manjón *et al.*, 2011) for effective fabrication of colloids via ultrashort laser ablation in liquid is to use tightly focused beams.

The importance of the bubble as a reservoir of particles has been recognized in several independent investigations(Wagener *et al.*, 2013)(Soliman *et al.*, 2010)(Chen *et al.*, 2017)(Reich *et al.*, 2017)(Ibrahimkutty *et al.*, 2015)(Amendola and Meneghetti, 2013)(Lam *et al.*, 2016) It has also been documented that the target shape and rigidity can largely determine the yield of NPs through its influence on the bubble

dynamics. (De Giacomo *et al.*, 2013)(Kohsakowski *et al.*, 2016) In (Al-Mamun *et al.*, 2013) several physical and chemical factors which influence the size of obtained NPs are investigated, among which the relative position (inclination) of the target was concluded to contribute to smaller size of obtained NPs. Many open questions and large number of independent parameters that can be changed during the NPs production, which on the other hand have increasing number of applications, make every research dealing with the fundamentals of underwater ablation relevant and important.

Material processing

The potential of processing material with lasers have been recognized almost as soon as the lasers were invented. Optimization of the processes demanded thorough dedicated studies which resulted in great deal of knowledge, systematised in several great books (Gladush and Smurov, 2011)(Kannatey-Asibu, 2009)(Peter Schaaf, 2010). The wide variety of laser material processing in which the interaction of the laser and material is occurring through the layer of liquid is described in great detail in two sequential publications (Kruusing, 2004a)(Kruusing, 2004b), which have formed the basis for the subsequently published book (Kruusing, 2008). Systematic overview of advantages and disadvantages of liquid assisted laser processing can be found there. Huge interest in under liquid material processing arose from several advantages that such processing is offering. During processing in liquid, significantly high pressures and temperatures can be achieved which introduces additional mechanical component to the process and increase the amount of the material removed from the surface of material(Hopp *et al.*, 2000)(Zhu *et al.*, 2001), e.g eight times for the case of aluminium (Wook Kang— *et al.*, 2008). Besides increasing the ablation efficiency , the liquid serves to cool the surface of the liquid and for efficient debris removal, leading to the less recast of material in the working zone.(Garcia-Giron *et al.*, 2016) This has additional beneficial impact since the emission in the atmosphere is reduced and the process is much safer for the operator due to the cleaner working area. Material present in the liquid is also useful product, e.g. NPs discussed in previous section. Purpose with which the liquid is introduced in the process of laser processing are numerous. Liquid has been used as a photo mask during backside etching of transparent materials, as a waveguide, for photochemical processes, removal of particles from the surface, subtractive processing (cutting,

drilling)(Tsai and Li, 2009) (Krstulović *et al.*, 2013), shock processing (peening, densification)(Martí-López *et al.*, 2011)(Peyre *et al.*, 1998). Beside the use of the shock wave impact, the cavitation bubble is sometimes also used, e.g for laser induced forward transfer for fabrication of diverse functional devices such as microbatteries, solar cells, organic light-emitting diodes, or biosensors (Duocastella *et al.*, 2009)

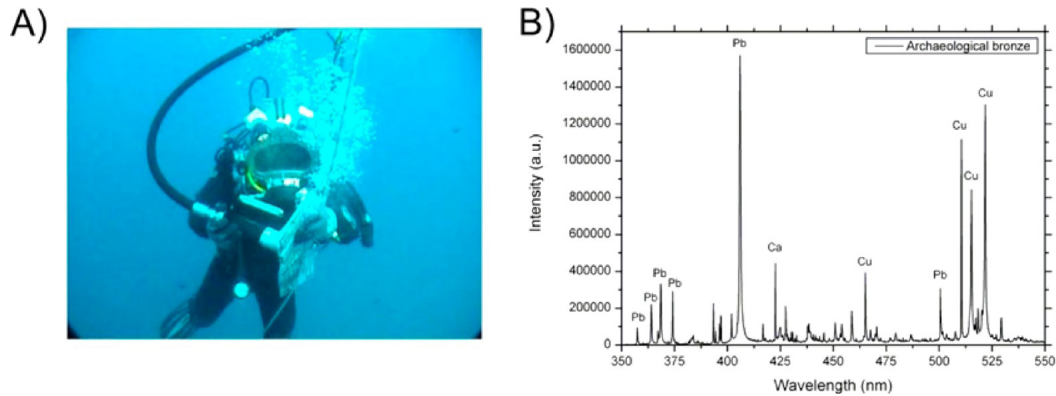


Figure 2.4: Pictures taken during the on-site trials on the Mediterranean Sea: A) display of the remote LIBS instrument on the research vessel and B) the diver working at a 30 meter depth.(Fortes *et al.*, 2013)

Material characterisation and applications in environmental, ecological and marine surveys

LIBS measurements are often performed on water solutions or inside the same. Due to the specific properties of the plasmas in liquid, usually only continuum emission and few very broad lines are detected in the spectrum when applying single laser pulse, i.e. in SP LIBS. To overcome the limitations of working underwater, a gas flow over the submerged target was deployed in (Beddows *et al.*, 2002) and also in on-site trials in the Mediterranean sea (Guirado *et al.*, 2012), see Fig. 2.4, or ablation of liquid jets was preferred (Rai and Rai, 2008)(Yueh *et al.*, 2002). Archaeological materials underwater were also the subject of study in (Lazic *et al.*, 2005) (Lazic, Colao, Fantoni, Spizzicchino and Jovićević, 2007) but there the DP LIBS technique was used to obtain the usable spectra. This method of the sensitivity increase (DP LIBS or multiple pulse LIBS) was used by many research groups, both for the submerged target and for bulk liquid, which resulted in rich and resolved spectra (Koch *et al.*, 2004)(Michel and Chave, 2008) (De Giacomo *et al.*, 2005)(Pichahchy *et al.*, 1997) (De Giacomo *et al.*, 2006)

Recently, effort was made to extend the applicability of the LIBS technique for the stand off applications underwater (Fortes *et al.*, 2015) which is extremely

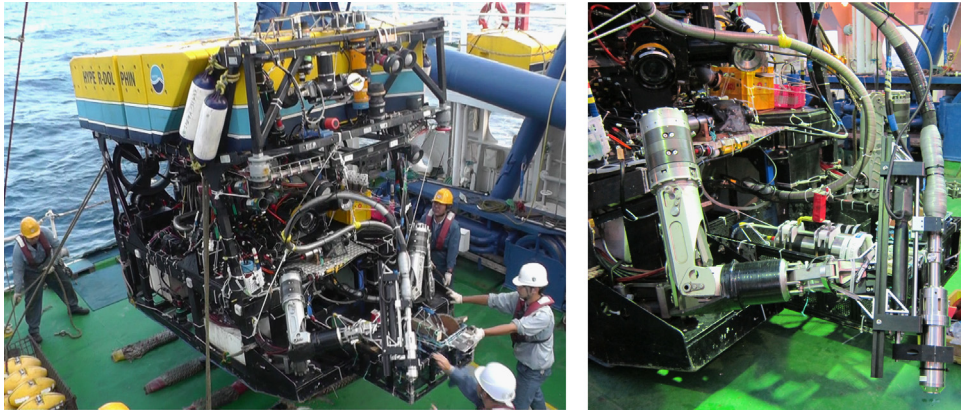


Figure 2.5: (A) ChemiCam mounted on the ROV Hyper-Dolphin 3000 about to be deployed in the Okinawa trough, and (B) a close-up of the linearly actuated focusing probe held by the ROVs manipulator.(Thornton *et al.*, 2015)

complicated task due to the large energy losses of the laser beam, presence of the impurities and bubbles, and dispersion of the useful optical signal in the long optical path. The successful application of the SP LIBS was only documented for long duration nanosecond pulses (Matsumoto *et al.*, 2013a)(Sakka *et al.*, 2006) which resulted in impressive ChemiCam apparatus(Thornton *et al.*, 2015), dedicated for deep sea research, see Fig.2.5. In the construction of the ChemiCam the greatest attention was devoted to building the long-pulse laser, which have also significantly increased the cost of the project. The commercial applications of this and similar devices would be significantly easier and readily available if the standard commercial laser can be used. One of the main tasks of the present thesis is to discover whether or not is possible to obtain the spectra of sufficiently good quality for material characterisation using the SP LIBS technique.

Chapter 3

Shock wave production and bubble formation

High energy density reached in the focal volume during the interaction of the laser with the material in the liquid environment leads to sudden increase of the temperature and the pressure, which causes powerful expansion of the plasma. Plasma expansion at supersonic speeds leads to the formation of the shock front surrounding the plasma. Afterwards, a cavitation bubble is generated, and it oscillates several times until all of its energy is spent. Basic theory behind the shock wave and bubble formation are given in the following, while the characteristics of laser plasma produced in liquid are described in the Chap.4

3.1 Laser induced shock wave

Fundamentals on the phenomena of the shock wave and the physics behind it are given in e.g. (Zel'dovich *et al.*, 1966). Brief survey, based on more specific considerations of shock wave emergence in the cases of laser ablation in liquid where also the cavitation bubble emerges ((Vogel, 1998)), are given in 3.1.1. Afterwards, the overview of the experimental techniques used for the shock wave characterisation is given, with more emphasis on the optical and imaging techniques, some of which were also employed in this study 6.3.

3.1.1 Physics of shock waves

Since it is quite hard to calculate the shock profile in the vicinity of the plasma, simple formulation of an idealized shock front are used instead, as a simpler method for determination of the pressure at the shock front. Shock front, in its essence, represents discontinuity in the fluid, where the pressure, density, particle velocity and internal energy of fluid are experiencing abrupt changes. Still, the conservation laws for mass, momentum and energy need to be fulfilled for the quantities behind and in the front of the shock front. For a medium at rest in front of the shock front ($u_p=0$) it can be written

$$u_s \rho_0 = (u_s - u_p) \rho_s \quad (3.1)$$

$$p_s - p_0 = u_s u_p \rho_0 \quad (3.2)$$

and

$$p_s u_p = \frac{1}{2} \rho_0 u_s u_p^2 + \rho_0 u_s (\varepsilon_s - \varepsilon_0) \quad (3.3)$$

Here ρ_0 and ρ_s are the densities and p_0 and p_s are the pressures in front of and behind the compression, u_s is the shock speed, u_p is the particle velocity behind the shock front, and $(\varepsilon_s - \varepsilon_0)$ is the increase in the specific internal energy of the fluid as it crosses the shock front.

Combination of the eq. 3.1 and eq. 3.2 eliminates the u_s and u_p from the eq. 3.3 and the Rankine-Hugoniot equation is obtained

$$\varepsilon_s - \varepsilon_0 = \frac{1}{2} \left(\frac{1}{\rho_0} - \frac{1}{\rho_s} \right) (p_s + p_0) \quad (3.4)$$

Equations 3.1-3.3 coupled with the material-specific equation, provide complete description of the relationships between all of the shock front parameters (p_s , ρ_s , u_s , u_p). This makes possible determination of all the parameters by measuring just one of them. Material specific equation can be either equation of state of medium, which connects the p_s and ρ_s or the Hugoniot curve for the medium, which describes the relationship between u_s and u_p . If the Hugoniot curve determined by Rice and Walsh is used as a material-specific equation

$$u_p = c_1 (10^{(u_s - c_0)/c_2} - 1) \quad (3.5)$$

relation between the pressure and the velocity of the shock front is obtained

$$p_s = c_1 \rho_0 u_s (10^{(u_s - c_0)/c_2} - 1) + p_{stat} \quad (3.6)$$

where $c_0 = 1483$ m/s is the sound speed and $\rho_0 = 998$ kg/m³ the density of the undisturbed water. $c_1 = 5190$ m/s and $c_2 = 25\,306$ m/s are empirical constants determined from Rankine-Hugoniot data for water by Rice and Walsh, and p_{stat} is the static pressure in the liquid (Delale (Ed.), 2013) (Tagawa *et al.*, 2016) (Vogel *et al.*, 1996).

3.1.2 Techniques of studying shock waves in LIB

Different experimental techniques used to characterize the shock waves and possibility to obtain various information about the shock wave characteristics in laser induced breakdown in liquid are discussed in (Vogel, 1998) and (Delale (Ed.), 2013). Usual path to reveal the propagation of the shock waves is to study the pressure amplitude p_s at the shock front and the shock wave profile as a function of the distance r from the emission centre of the shock wave. If the $p_s(r)$ is determined, energy transfer from the shock wave to the surrounding can be assessed, which is especially important in medical applications where the shock wave impacts the tissue. Direct measurements of the pressure in the vicinity of the emission centre are much harder than the far field measurements, and due to this fact, it is important to obtain knowledge of the scaling laws for the shock pressure with increasing distance from the emission centre. This enable one to calculate the pressure in the vicinity of the plasma based on the far field measurements. Shock pressure in the far field can be measured very simply using the piezoelectric pressure probes with sufficient fast response times (Vogel and Lauterborn, 1988). Numerous studies of the subject have shown that the shock speed decreases very fast in a first few hundreds of nanoseconds and over a distances of a few hundreds of micrometers (Alloncle *et al.*, 1994) (Martí-López *et al.*, 2011) (T. Tsuji *et al.*, 2007). The largest energy depositions is actually occurring before the speed of the shock wave decreases to the sound speed, in the region very near to the emission center and in the very short time, thus measurements of high temporal and spatial resolution are required to resolve the properties of the shock wave in this early phase.

Unfortunately, the shock pressure close to the plasma can not be measured with hydrophones since they can easily be damaged due to the strong pressure transients

or due to the cavitation events. Much better option are optical diagnostic methods, either photographic or some probe beam technique. The spatial resolution of these methods is limited only by the resolution of the imaging optics or the size of the probe beam focus, which can be as little as few μm . Fundamental principle on which all optical techniques for shock wave detection are relying is the change of refractive index of a fluid as a consequence of the pressure change (Abraham *et al.*, 2000). The change of refractive index results in a phase shift or change in direction of the light that is proportional to the pressure gradient. (Alloncle *et al.*, 1994) The optical techniques in which the deflection of light through the shock wave is used qualitatively for detection of the shock front location can be also applied for measurements of the shock pressure in the vicinity of the plasma. These techniques actually measure the velocity of the shock front and based on the equations of state of the fluid, the pressure jump at the shock front is then determined (Alloncle *et al.*, 1994) (T. Tsuji *et al.*, 2007). The disadvantage of the probe techniques is that they provide one-dimensional picture of the shock propagation, and any fluctuations in the breakdown position (which can not be recognized) increase the inaccuracies in the measurements. This problem can be overcome by employing photographic techniques, where the shock wave propagation is determined from the series of photographs, taken at different delays after the laser pulse. This procedure was also applied in this experiment, 5.1.26.3. Further improvement can be obtained with a streak camera, which make possible to record complete evolution of the shock front from one laser shot. (Noack *et al.*, 1998)

3.2 Cavitation bubble

3.2.1 Process of cavitation

The process of cavitation represents the emergence of the vapour cavities inside the liquids, or alternatively it can be defined as a breakdown of a liquid medium under very low pressures. (Franc and Michel, 2004). The process can occur both in the static liquid and in the liquid flows. Essential requirement for cavitation is a region of liquid in which the absolute pressure is less than or equal to the vapour pressure of the liquid. Very thorough description of the fundamental physics behind the cavitation process can be found in the (Brennen, 1995). There, the description of the processes starts from the very pure liquids and clean environments, to separate

the effects of the liquid itself and different impurities and inceptions that can be found in the industrial and engineering systems. Unclean environments are also found in the conditions of the laser ablation in the liquid, where a large amount of the ablated material is present.(Cristoforetti *et al.*, 2012)(Chen *et al.*, 2017). Usual practice in the engineering applications is to separate the two mechanisms of bubble creation in liquid: cavitation and boiling. A simple way to distinguish between these two routes of bubble emergence in the liquid is to define the cavitation as a process of nucleation when the pressure falls below the vapour pressure, and boiling as a process of nucleation when the temperature is raised above the saturated vapour/liquid temperature. But in its essence, there is not much difference between the two processes and they are mostly reviewed simultaneously.

In the case of the laser created bubble on a submerged target, both the pressure and the temperature conditions are experiencing large and sudden changes(De Giacomo *et al.*, 2004) and, irrespective of the thermodynamic route leading to the bubble creation, the bubble will be referred as cavitation bubble as is usual done in the literature(Petkovšek *et al.*, 2007)(Sakka *et al.*, 2014)(Ibrahimkutty *et al.*, 2012).

The problem of the spherical cavity in an infinite medium was solved first for a non-viscous liquid by (Rayleigh, 1917) to interpret the phenomenon of cavitation erosion, while viscous and non-compressible liquid was considered later on in (Plesset, 1949)(Plesset and Prosperetti, 1977). Although rather simple, Rayleigh's analysis proved as quite useful in many practical cases such as bubble collapse, bubble formation from a nucleus, bubble oscillations, and also for laser produced bubbles of interest here. Very often, this simple model is used in describing the dynamics of the laser induced bubble (Peel *et al.*, 2011)(Gregorčič *et al.*, 2012)(Tomita and Kodama, 2003)(Vogel *et al.*, 1989) or with some additional conditions to account for different effects(Gregorčič *et al.*, 2007), the bubble content(Akhatov *et al.*, 2001) and often compared with other models(Nath and Khare, 2011). Extensions of the Rayleigh-Plesset equations 3.16 have also been used in explanations of highly interesting effect of single bubble sonoluminescence.(Brenner *et al.*, 2002)(Margulis and Margulis, 2006)(Ohl *et al.*, 1999). In (Matula *et al.*, 2002), modified Rayleigh–Plesset bubble dynamics equation of motion with incorporated mass and heat transfer across the bubble boundary and with chemical reactions included was applied to describe the behaviour of individual bubbles exposed to shock wave lithotripsy. This approach was used also for describing the phenomenon of sonoluminescence.

In the following simple model of the dynamic evolution of a spherical bubble in an

infinite domain of liquid at rest far from the bubble and with uniform temperature far from the bubble will be considered. (Franc and Michel, 2004) (Brennen, 1995) More thorough explanation can be found in the aforementioned books. Later on, some modification of the theories of bubble evolution, suited better for the case of underwater laser ablation will be described 3.2.3.

3.2.2 Simple model of spherical bubble dynamics

Starting point of the simple model is a spherical bubble of radius, $R(t)$ in an infinite domain of liquid whose temperature and pressure far from the bubble are T_∞ and $p_\infty(t)$ respectively, see Fig. 3.1. The temperature, T_∞ , is assumed to be a simple constant while the pressure, $p_\infty(t)$, is assumed to be a known input which regulates the growth or collapse of the bubble. The liquid density ρ_L and viscosity μ_L are considered constant and uniform (incompressible liquid), while the content of the bubble is considered to be homogeneous, with uniform pressure $p_B(t)$ and temperature $T_B(t)$ inside the bubble.

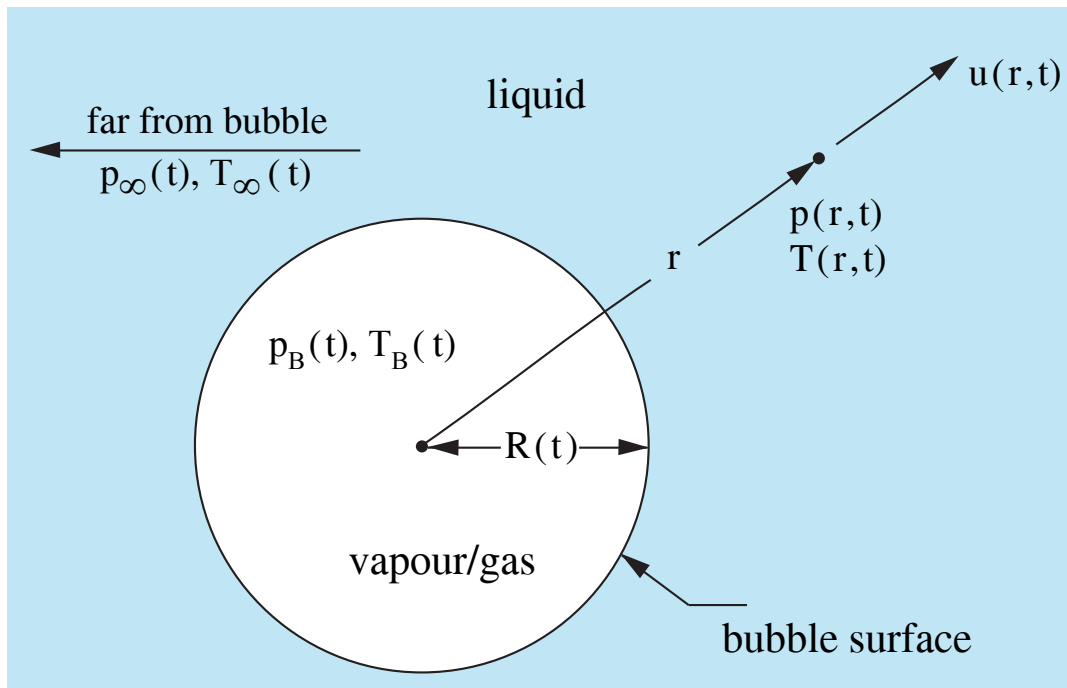


Figure 3.1: Schematic of a spherical bubble in an infinite liquid.

The primary goal of the analysis is to obtain the expression for the temporal dependence of the bubble radius, $R(t)$. Conservation of mass leads to the relation:

$$u(R, t) = \frac{F(t)}{r^2} \quad (3.7)$$

where $F(t)$ is related to $R(t)$ by a kinematic boundary condition at the bubble surface. When the mass transport across the interface (bubble surface) is zero, radial outward velocity can also be expressed as $u(r,t) = dR/dt$, leading to the:

$$F(t) = R^2 \frac{dR}{dt} \quad (3.8)$$

Although eq.3.8 is derived under the assumption of the zero mass transport, it is often fairly good approximation in the cases where evaporation and condensation occur at the interface. This is supported by the following reasoning. The rate at which the bubble size grows must be equal to the volume rate production of the vapour, $4\pi R^2 dR/dt$, hence mass rate of evaporation is equal to $\rho_V(T_B)4\pi R^2 dR/dt$, where $\rho_V(T_B)$ is the saturated vapour density at the bubble temperature T_B . On the other hand, this must be balanced by inward mass flow of the liquid relative to the interface, which yields for the inward velocity of the liquid $\rho_V(T_B)(dR/dt)/\rho_L$. Resulting outward velocity is then given by:

$$u(R, t) = \frac{dR}{dt} - \frac{\rho_V(T_B)}{\rho_L} \frac{dR}{dt} \quad (3.9)$$

which gives

$$F(t) = \left(1 - \frac{\rho_V(T_B)}{\rho_L}\right) R^2 \frac{dR}{dt} \quad (3.10)$$

Since in the most of the practical situations the $\rho_V(T_B) \ll \rho_L$ the use of the eq.3.8 is justified even in the cases when there exist some evaporation and condensation on the surface. Having this in mind, in continuance of derivation of simple model for spherical bubble dynamics it will be assumed that eq.3.8 is valid.

Motion in the r direction can be written using the Navier-Stokes equation for the Newtonian liquid as

$$-\frac{1}{\rho_L} \frac{\partial p}{\partial r} = \frac{\partial u}{\partial t} + u \frac{\partial u}{\partial r} - \nu_L \left[\frac{1}{r^2} \frac{\partial}{\partial r} \left(r^2 \frac{\partial u}{\partial r} \right) - \frac{2u}{r^2} \right] \quad (3.11)$$

where ν is kinematic viscosity. After substituting u with eq.3.7 in eq.3.11 it follows

$$-\frac{1}{\rho_L} \frac{\partial p}{\partial r} = \frac{1}{r^2} \frac{dF}{dt} - \frac{2F^2}{r^5} \quad (3.12)$$

If the eq.3.12 is integrated and the boundary conditions $p \rightarrow p_\infty$ as $r \rightarrow \infty$ it obtains the following form:

$$\frac{p - p_\infty}{\rho_L} = \frac{\partial}{\partial r} \frac{1}{dt} \frac{dF}{dt} - \frac{1}{2} \frac{F^2}{r^4} \quad (3.13)$$

Interesting thing to note that viscous term vanishes from the equation 3.12. The only viscous term that still needs to be taken into account comes from the dynamic boundary condition on the bubble surface. To find this boundary condition thin volume on the interface is observed. The net force on this thin volume in the outward radial direction per unit area is given as

$$(\sigma_{rr})_{r=R} + p_B - \frac{2S}{R} \quad (3.14)$$

or, since the stress tensor σ_{rr} is $\sigma_{rr} = -p + 2 \mu_L \partial u / \partial r$, the force per unit area can be written as

$$p_B - (p)_{r=R} - \frac{4\mu_L}{R} \frac{dR}{dt} - \frac{2S}{R} \quad (3.15)$$

If, again, the evaporation and condensation across the interface do not occur the net force given by eq.3.15 needs to be zero. Substitution of the value $(p)_{r=R}$ from eq.3.13 with the value of F given by eq.3.8 the generalize form of the *Rayleigh-Plesset* equation is obtained:

$$\frac{p_B(t) - p_\infty(t)}{\rho_L} = R \frac{d^2 R}{dt^2} + \frac{3}{2} \left(\frac{dR}{dt} \right)^2 + \frac{4\mu_L}{R} \frac{dR}{dt} + \frac{2S}{\rho_L R} \quad (3.16)$$

If we neglect the liquid viscosity eq.3.16 is known as a RAYLEIGH equation. Since in the problem of the bubble collapse bubble behaviour is mostly determined by inertial forces, liquid viscosity and surface tension can be neglected. Then much simpler RAYLEIGH equation can be solved to obtain the bubble collapse time. To be able to do that, it is necessary to estimate also the contents of the bubble. Under general assumptions it is usually considered that the bubble contains some quantity of the gas with the partial pressure p_{G0} at reference size R_0 and temperature T_∞ .

$$p_B(t) = p_V(T_B) + p_{G0} \left(\frac{T_B}{T_\infty} \right) \left(\frac{R_0}{R} \right)^3 \quad (3.17)$$

This relation for the bubble pressure eq.3.17 is substituted in the 3.16, which gives Rayleigh-Plesset equation in the following general form:

$$\frac{p_V(T_\infty) - p_\infty(t)}{\rho_L} + \frac{p_V(T_B) - p_V(T_\infty)}{\rho_L} + \frac{p_{G0}}{\rho_L} \left(\frac{T_B}{T_\infty} \right) \left(\frac{R_0}{R} \right)^3 = R \frac{d^2 R}{dt^2} + \frac{3}{2} \left(\frac{dR}{dt} \right)^2 + \frac{4\mu_L}{R} \frac{dR}{dt} + \frac{2S}{\rho_L R} \quad (3.18)$$

The first term in eq.3.18 is the instantaneous tension or driving term determined by the conditions far from the bubble. The degree to which the bubble temperature, T_B , departs from the remote liquid temperature, T_∞ , can have a major effect on the bubble dynamics. To determine this departure it is necessary to solve the heat diffusion equation, and there is no exact solution. But, in the cases when the thermal effects need to be taken into account, the approximate solution of Plesset and Zwick is often good enough. This is beyond the simple model presented here, and in the further discussion, the thermal term (term 2 in the eq.3.18) will be neglected. This is so called "inertially controlled" bubble behaviour. In addition, the behaviour of the gas in the bubble will be assumed polytropic so that

$$p_G = p_{G0} \left(\frac{R_0}{R} \right)^{3k} \quad (3.19)$$

where k is approximately constant. With $k=1$ the bubble temperature would be constant, while $k=\gamma$ would correspond to adiabatic expansion, where γ is the ratio of specific heats. Introducing these approximations, the *Rayleigh-Plesset* equation becomes:

$$\frac{p_V(T_\infty) - p_\infty(t)}{\rho_L} + \frac{p_{G0}}{\rho_L} \left(\frac{R_0}{R} \right)^{3k} = R \frac{d^2 R}{dt^2} + \frac{3}{2} \left(\frac{dR}{dt} \right)^2 + \frac{4\mu_L}{R} \frac{dR}{dt} + \frac{2S}{\rho_L R} \quad (3.20)$$

In order to perform the integration, the viscous term, tension term and noncondensable gas will be neglected. With these simplifications, and having in mind that $R\ddot{R} + \frac{3}{2}\dot{R}^2 = \frac{1}{2R\dot{R}^2} \frac{d}{dt} [\dot{R}^2 R^3]$ the integration of eq. 3.20 gives

$$\rho_L \dot{R}^2 R^3 = -\frac{2}{3} (p_\infty - p_V) (R^3 - R_0^3) \quad (3.21)$$

Since \dot{r} is negative during the collapse, it follows:

$$\frac{dR}{dt} = -\sqrt{\frac{2}{3} \frac{p_\infty - p_V}{\rho_L} \left[\frac{R_0^3}{R^3} - 1 \right]} \quad (3.22)$$

The numerical integration of equation 3.22 gives the characteristic collapse time or *Rayleigh* time:

$$\tau = \sqrt{\frac{3}{2} \frac{\rho_L}{p_\infty - p_V}} \int_0^{R_0} \frac{dR}{\sqrt{\frac{R_0^3}{R^3} - 1}} \cong 0.915 R_0 \sqrt{\frac{\rho_L}{p_\infty - p_V}} \quad (3.23)$$

The constant 0.915 is the approximate value of $\sqrt{\frac{\pi}{6}} \frac{\Gamma(5/6)}{\Gamma(4/3)}$ where Γ is the factorial gamma function.

The equation 3.23 is very often employed in laser induced breakdown on a submerged target studies to estimate the maximum bubble radius from the measured time of the bubble collapse from optical or acoustic measurements(Lazic, Jovicic, Fantoni and Colao, 2007)(Huber *et al.*, 1998)(Vogel *et al.*, 1989). Eq.3.23 will also be employed in this study in order to assess the amount of the input laser energy stored in the bubble, see chap.6.2.3.

3.2.3 Laser induced bubble on a solid target

The phenomenon of laser-induced cavitation over a target surface differs from the ideal case of a spherical bubble produced in bulk water since the ablation products influence the evolution of the bubble, which can, in addition, interact with the target surface via heat or mechanical energy transfer. Although dynamics of the cavitation bubble formed after laser ablation in liquid is more complex than this simple model described in 3.2.2, as pointed out in (Cristoforetti *et al.*, 2012), it is often reproduced satisfactorily with it and, in the absence of dedicated experimental and theoretical investigations about the dynamic of the bubble over target surface, it is often applied in the literature. This might appear incorrect, since the bubble produced by laser ablation in liquid is of approximately hemispherical shape and simple model in 3.2.2 was derived for spherical bubble in infinite domain of liquid. But, due to the symmetry of the problem, if the surface tension effects at the rigid boundary are neglected, the hemispherical bubble should collapse in the similar manner as in the spherical case away from all boundaries. To enhance the agreement between theoretical predictions and measured bubble parameters, usually several additional effects are included in the models. In (Casavola *et al.*, 2005) the Rayleigh-Plesset equation is generalized to account for the liquid compressibility and Keller-Miksis formulation is used instead(Brenner *et al.*, 2002). For the estimation of the conditions inside the bubble, an adiabatic Van der Waals equation of state is assumed and solved together with the Keller-Miksis equation. This model of bubble dynamics had a goal to determine the optimal timing between the pulses in DP-LIBS, since the characteristics of the spectra produced by the second laser pulse are largely dependent on the temperature and pressure conditions inside the bubble. The optimal timing between the successive laser pulses in DP-LIBS has been the subject

of discussion in preceding years, where several research groups came to slightly different conclusions (Sakka *et al.*, 2012) (Cristoforetti *et al.*, 2012) (De Giacomo *et al.*, 2007) (Lazic *et al.*, 2013a) (Lazic *et al.*, 2013b)

When dealing with the cavitation bubble formed over a target surface it is supposed that, due to the inherent asymmetry of the bubble collapsing on the surface of the target, some deviation from experimental observation during the bubble collapse phase will occur. Indeed, when the bubble is created near the boundary or on the surface, the shrinking phase of the bubble is difficult to model due to the breaking of some assumptions used to derive the Rayleigh-Plesset equation and their improved versions. Importance of the bubble collapse phase is recently emphasized in the context of the nanoparticles production in the liquid (Ibrahimkuty *et al.*, 2015) (Ibrahimkuty *et al.*, 2012) The question of whether the material is trapped inside the bubble and if it is released during the collapse are still not completely understood, although recent experimental results suggest that the bubble confines material inside and also partially redeposit material back to the target surface (Ibrahimkuty *et al.*, 2015). The influence of different target shapes on the successive bubble evolution and hence the nanoparticle yield was investigated in (De Giacomo *et al.*, 2013). The authors applied multiple experimental techniques, Optical Emission Spectroscopy for the plasma characterization, fast shadowgraph for plasma and cavitation bubble dynamics and laser scattering for the mechanisms of delivery of the produced materials in the liquid. They discovered unusual arrow-bow ejection phenomena when the cavitation bubble was formed on the wire shaped target, which they connected with the suppressed material back-deposition and more efficient ejection of ablated matter into the liquid, see fig. 3.2

On the other side, according to the recent investigations of the bubble dynamics in the frame of the nanoparticles production through the laser ablation in the liquid, system evolution is found to be mostly inertial and adiabatic (Lam, 2015). In addition, the authors also dealt with the "hot-topic" regarding the content of the bubble, arriving to the conclusion that the inside of the bubble is mostly occupied by solvent molecules whose number is not changing dramatically. These several examples illustrate the high interest and still large number of unresolved issues regarding the relation of the cavitation bubble and ablated material, which will be to some extent addressed here.6.10 although the primary interest of this investigation are relations between the bubble and the plasma.

Collapse of the cavitation bubble and formation of jets or additional shock waves

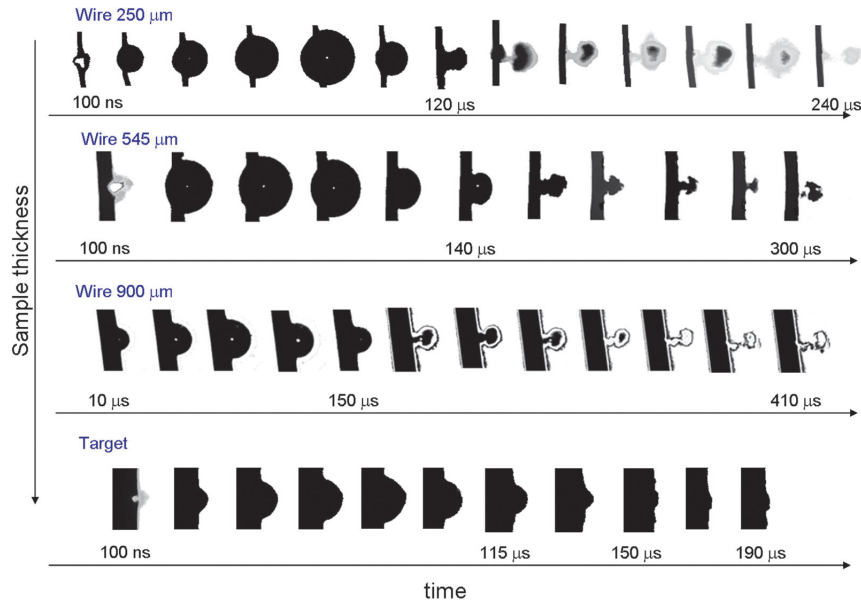


Figure 3.2: Influence of the target shape on the bubble evolution: comparison between laser ablation of the wire and bulk target (De Giacomo *et al.*, 2013)

upon the bubble collapse is another interesting subject that has been investigated over the years (Ellis, 1953) (Benjamin and Ellis, 1966) (Vogel *et al.*, 1989) (Ohl *et al.*, 1999) and example of the emergence of the jet is given in the fig.3.3.

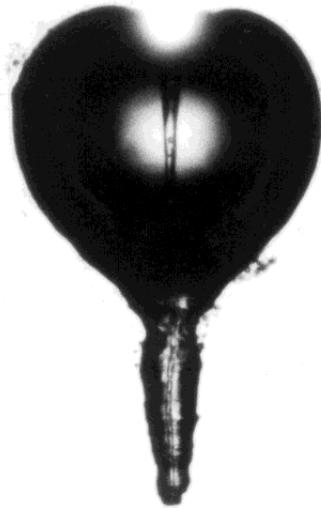


Figure 3.3: Example of the jet formation during the collapse of the laser induced bubble near solid boundary (Vogel and Venugopalan, 2003)

These research are mostly relevant for medical application of laser ablation (Brujan *et al.*, 2001) and laser-material processing where the impact of the cavitation bubble is very often undesired side-effect. Today's held view is that the most of the cavitation damage is induced primarily due to the asymmetrical bubble col-

lapses, where distinctive jet and counter propagating jet are formed (Takada *et al.*, 2010). The strong influence of the bubble collapse will also be documented in this experiment, through the second shock wave and ,in some cases, intensity emission enhancement detected in the period of the bubble collapse.6.5

3.2.4 Interaction of light with bubbles

Other than its great influence on the material and plasma trapped inside, cavitation bubble impacts quite significantly rays that are encountering the bubble surface. (Langley and Marston, 1991) This is of big importance for optical diagnostics techniques, since the information obtained might be modulated by the presence of the bubble in liquid, which has significantly different refractive index (~ 1) from the surrounding liquid(~ 1.33 for distilled water). The bubble inside the liquid acts as a negative lens, whose focal length measured in (Lazic *et al.*, 2012) at the moment of the maximal expansion is only $f = -11$ mm at the wavelength of 1064 nm. Defocusing and refraction of the light by vapour cavity increases at shorter wavelengths. This defocusing power of the bubble needs to be taken into account when performing DP LIBS experiment, since it enlarges the ablation craters and decreases the ablation efficiency.(Lazic and Jovićević, 2014). Apart from defocusing effect on the incoming laser beam, the optical effects of the bubble also lead to the spatial redistribution of the plasma radiation created by the second laser pulse. This can lead to very large signal losses, since more than 50% of the plasma radiation can escape the detector depending on the optical collecting system employed. In addition, the bright central spot in the proximity of the bubble center is formed due to the multiple reflections from the bubble wall, which can partially recover the signal intensity Optical effects of the bubble, relevant for the DP LIBS, will be analysed here 6.2.2 also in the view of the SP LIBS for the first time, since the duration of the plasma emission in this experiment is of the same order of magnitude as the bubble duration, which enables to study their mutual influences.

Interaction of the spherical bubble and light has been studied intensively due to numerous applications in which the measurements of the radius and lifetime of the bubble were of interest. In the beginning they were mostly dealing with the stationary bubbles in water and refined over time to suit better the measurement of nonlinear pulsation of bubbles, as those encountered in the sonoluminescence(Barber and Putterman, 1992)(Crum *et al.*, 1999). When the diameter of the scattering ob-

ject is small compared to the wavelength of the probing laser beam, the dominant contribution to the scattering signal is Rayleigh scattering and in the 90° direction to the probe beam. As the diameter of the scattering object increases scattering law starts to change to Mie's scattering, and the preferential direction of the scattering is in the forward direction.(Huber *et al.*, 1998). Since the laser produced bubbles are known to have a diameter in the range of 0.01 to few mm (Kennedy *et al.*, 1997)) the scattering from them can be described by Mie's theory,see Fig.3.4.

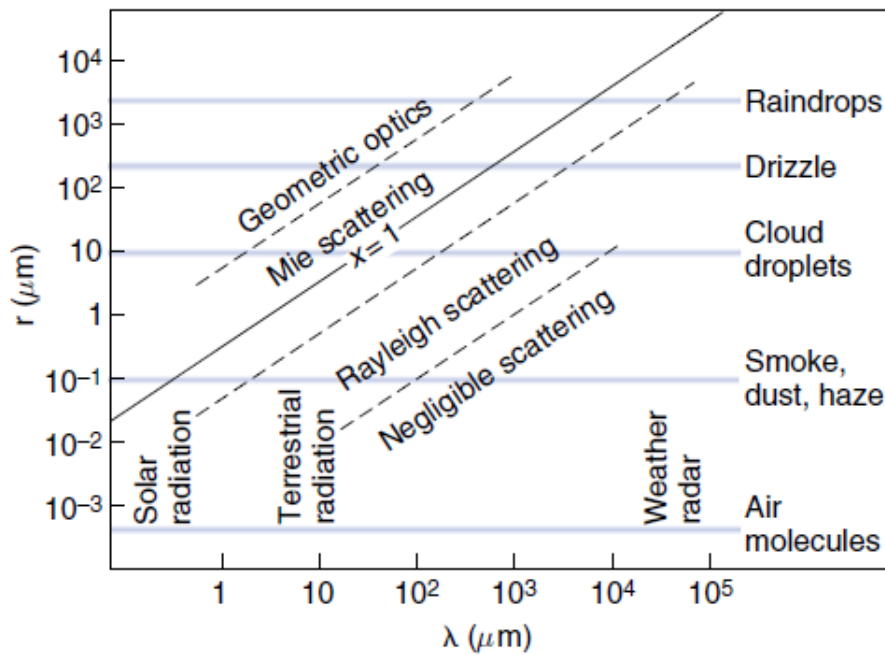


Figure 3.4: Size parameter x as a function of wavelength λ of the incident radiation and particle radius r .(Wallace and Hobbs, 2006)

If the size, shape and composition of the scatterer are assumed, classical electrodynamics can be used to determine the size of the bubble based on the scattered signal intensity.(Yu *et al.*, 2008). An exact solution for the scattering of electromagnetic waves from a spherical dielectric body was first obtained by Mie(Mie, 1908), and hence the term Mie's scattering. In (Lentz *et al.*, 1995) laser-scattering technique has been developed to size sonoluminescing bubbles in water by the use of Mie scattering lobe clusters. Comparison of the measured and calculated intensities of the scattered light according to the Mie's scattering theory is given in (Holt and Crum, 1990). Scattering of electromagnetic radiation from a sphere, so-called Mie scattering, requires calculations that can become lengthy, hence great deal of work was devoted to improvement and optimization of the Mie scattering algorithms ,see

e.g. (Wiscombe, 1980)(Mätzler, 2002). If the diameter of the scatterer is further increased the process of the scattering can be described with much simpler geometrical optics approximation, see Fig.3.4. This is especially convenient since the numerical calculations of the Mie coefficients becomes time consuming and difficult as the size of the scatterer is increased. For a large particles, geometrical optics approximation in which the scattered light intensity is obtained as the superposition of the reflected, refracted and diffracted rays, is considered advantageous since it avoids the difficulties with Bessel functions of high orders in the Mie coefficient calculations. General characteristics of the geometrical light scattering by spheres is given in (McK. Ellison and Peetz, 1959). Theoretical investigation of the scattering from the large air bubbles in water (Yu *et al.*, 2008) in which the total reflection was taken into account proved that geometrical optics approximation approach agree well with the results obtained from Mie theory for those particles with relative refractive index $m < 1$ and dimensionless particle size parameter $\alpha > 50$, where $m = m_2/m_1$ is the relative refractive index, viz. the ratio of the refractive index of the particle m_2 to that of the medium m_1 , and $\alpha = 2\pi a/\lambda$ is the dimensionless particle size parameter, where a is the radius of spherical particle and λ is the wavelength of the incident light in the medium. Comparison of the results of the Mie theory and geometrical optics approximations yielded good agreement for the case of the spheroidal bubble in (He *et al.*, 2012) and for critical angle scattering (Dean and Marston, 1991).

Amplitude of the measured scattered signal is largely dependent on the angle between the laser and the detector. In the geometrical optics approximation, intensity of the light scattered by the spherical bubble or radius R is proportional to R^2 for all scattering angles (Barber and Putterman, 1992)(Matula *et al.*, 2002)(Lazic, Jovievic, Fantoni and Colao, 2007). Thus, if the intensity of the scattered probe beam on the bubble is measured on the opposite side with suitable detector (photomultiplier or photo diode), the bubble radius will be proportional to the square root of its voltage. As radius varies, the exact Mie's result for the light scattered into a fixed angle also follows approximately the square dependence but with many additional fringes. This problem can be easily avoided in the measurement by using the short focal length lenses with large aperture which averages the result across the large angle and thus the fringes disappear. It was found in (Barber and Putterman, 1992) that the deviation from the R^2 dependence is less than 10 % for bubbles with radius larger than $1 \mu\text{m}$. This property was used for the scattering measurements described in 5.2 and the results are given in the Sect.6.2.4

Chapter 4

Plasma formation in liquid ambient

The fourth state of the matter called plasma, can be created in a number of ways, one of which is the laser induced breakdown (LIB). During the LIB, plasma emerges as a consequence of the complete or partial ionization of solid, liquid or gaseous sample following the dielectric breakdown occurred due to the absorption of electromagnetic energy. Plasma represents the gas mixture which contains the neutral particles (atoms and molecules), positive ions, and free electrons able to interact among themselves and with photons emerging from different energy levels and excitation states. In gaseous surrounding the plasma formation is usually initiated through the multiphoton absorption or cascade ionization of the 'free electrons' which are always present in the gases. In contrast, inside solids and liquids electrons are either bound to the particular molecule or lattice site or are 'quasi-free', i.e. they possess enough kinetic energy that they can move through the liquid or solid lattice without being trapped by localized potential wells. (Kennedy *et al.*, 1997). Having that difference in mind, transition between the bound and quasi-free state during the breakdown in the condensed matter corresponds to the molecular ionization in gases. LIB mechanisms in liquid media are far less studied compared to the LIB in gaseous and solid media. Besides few exceptions, e.g. (Barnes, 1969), studies of LIB in liquid have been rarely mentioned before 1980's, when wide variety of laser applications in medicine draw attention to this topic. (Docchio *et al.*, 1988)(Docchio *et al.*, 1988) Since the great deal of medical (and other) applications as a breakdown medium use water, correspondingly more research was devoted to the studies of LIB in water. But liquid water represents extremely complicated medium with complex physical structure,

molecular bonding and band structure, due to which many questions about complex sequence of interrelated phenomena produced by LIB in water remained open. In the following, basic mechanisms of the processes responsible for the breakdown in the liquid media and on submerged target are explained, after which the properties of plasmas created in the process are outlined with an accent on the emission spectra of interest for LIBS.

4.1 Plasma creation through the LIB

1. LIB in the bulk of liquid

Breakdown in aqueous media is defined experimentally through detectable effects of laser radiation in media, like plasma emission, bubbles and shock waves. Theoretical modeling of LIB thresholds requires defining a minimum free electron density which corresponds to a breakdown, usually referred to as the critical density. Laser radiation in general can lead to a breakdown in two different ways: thermal breakdown or optical breakdown. The former case is mainly connected to the long duration pulses or high power repetitive pulses applied on materials with high linear absorption coefficients whilst optical breakdown involves use of short duration pulses, from micro to femto second regimes. Optical breakdown is of greater importance for LIBS underwater since it is the primary mechanism of laser-induced breakdown when dealing with transparent medium. Main principles of plasma formation in the case of interaction of short pulse lasers and water rely on electron cascade formation or direct ionization by multiphoton absorption (Kennedy *et al.*, 1997). Both mechanisms of plasma formation can occur also in solids and gases. The threshold irradiance required for LIB is a function of both the medium characteristics (ionization energy, impurity level) and the beam characteristics (wavelength, pulse width, beam diameter at focus). Threshold measurements are the first step in any experimental characterization of LIB. Similarly, calculation of the breakdown threshold is a key goal of any theoretical model. This is not an easy task, since liquids are very complex media, (liquid water in particular), therefore main body of theoretical calculations of LIB threshold values are based on fitting of experimental data with different simple formalisms, such as lucky electron model (Shockley, 1961). This model was the first evidence of cascade ionization in liquids as a primary mechanism for LIB for nanosecond to picosecond pulses, similarly like in solids for

the same pulse width range. However, this model can not account for multiphoton ionization nor to include impact of present impurities, and for that reason it can not be used for the calculations of the threshold values in a general case. Except lucky electron model, common alternative approach to cascade breakdown modeling is rate equation model. Using the rate equation formalism and Drude model (uniform scattering rate for all free electrons) cascade ionization threshold can be easily calculated. For multiphoton ionization in liquids, most frequently employed is Keldysh model, originally developed for semiconductors, but applicable in the case of liquids if considered as amorphous semiconductors. (Williams *et al.*, 1976) Kennedy provided first order model for estimation of LIB threshold (Kennedy, 1995) that accounts both multiphoton and cascade ionization regimes. In relation to femto and pico second pulses significant interest was devoted to self-focusing effect on LIB threshold. It was found by comparing experiments, first order model and numerical simulation that this effect plays important role in the case of short laser pulse regimes (pico and femto). (Feng *et al.*, 1997)

Cascade ionisation – To start the process of cascade ionisation (also called avalanche ionisation) seed electrons must be produced (since they are not present in liquids like in the case of gases) and then by multiplication, high number of free electrons (critical density) is achieved. Cascade ionization is initiated when primary electron absorbs laser photons during collisions with heavy particles, process named as inverse bremsstrahlung absorption. Role of the heavy particles is to preserve the momentum and energy. After photon absorption free electron has enough energy to ionize bound electron by collision, leading to the creation of two free electrons with lower energies. Repetition of this process leads to the multiplication of the free electrons or electron cascade (breakdown). Nevertheless, in order to have an electron cascade, rate of energy losses has to be smaller than rate of energy produced in focal volume. Energy losses are mainly due to inelastic collisions. Considering the fact that energy gain is proportional to irradiance but energy losses are not, it follows that threshold irradiance value exist for which breakdown process will occur.

Multiphoton ionisation – On the other hand, multiphoton ionisation is in its basics much simpler process. It does not require an initiation and it is much faster, therefore the lost mechanisms can be ignored. Every electron in the process of multiphoton ionization is ionized by absorption of multiple photons from the field, therefore particle-particle interactions and collisions are not needed. In this way, process of multiphoton ionization doesn't depend on the presence of impurities and

it can take place in very diffuse media in which multiple collisions can not occur. In respect to the cascade ionization, it is much faster process and it can happens even for the very short laser pulse durations. On the other hand, energies required for multiphoton ionization are much higher than energies for cascade ionization, since multiphoton ionization is nonlinear process for which very high irradiances are needed. Because of that, more common way of plasma formation is cascade avalanche ionization, except in the case of short laser pulses (femtosecond) where the field in the focal volume doesn't exist long enough to allow formation of the critical density of free electrons. Also in the case of diffuse gases, multiphoton ionization is favourable process in respect to avalanche ionization since collision rates are very low to establish significant number of free electrons through collision processes. Except as an independent method of breakdown in liquids, multiphoton ionization is often considered as initiation mechanism for avalanche ionization, especially for media with little amount of impurities or very diffuse media, where no other way for starting the cascade process exists.

Effect of impurities – Presence of impurities significantly lowers breakdown threshold in liquids and makes it probabilistic process with defined probability of a breakdown. In the case of water with impurities, initial seed electrons for cascade ionization mainly come from the thermal excitation of those impurities, which produce initial free electron density in the focal volume. For pure water, initial free electrons must be produced through the process of multiphoton absorption, but for that to happen much higher irradiances are needed. In the later case, there will actually be two thresholds associated with the cascade breakdown. (Kennedy, 1995)(Shen, 1984) The first threshold is related to the irradiance needed to initiate a cascade by producing minimal critical density through multiphoton ionization. The other threshold is the irradiance needed to sustain a cascade to breakdown with initial critical density of free electrons. Since cascade breakdown threshold is usually much lower than multiphoton ionization threshold, measured threshold values actually correspond to either multiphoton ionisation or impurity-initiated cascade breakdown. In pure water where two threshold values need to be surpassed, measured threshold value should be the higher, in this case multiphoton breakdown threshold. On the contrary, when liquid contains enough amounts of the impurities that multiphoton initiation of cascade process is not needed, measured threshold value corresponds to the cascade breakdown threshold. With the shortening of the pulse duration (other parameters remain constant) relation between these two threshold is

changing: both threshold increase as pulse duration decrease, but cascade threshold increase at much bigger rate. Based on that fact, influence of impurity presence in liquid should gradually decrease when moving to the short pulse regime, which is experimentally confirmed (Docchio *et al.*, 1986). Importance of the impurities for the LIB in water and alcohol is recently emphasized (Toker *et al.*, 2009)(Kovalchuk *et al.*, 2010). It was proven that mechanism of the breakdown is initiated by inclusion particles and that laser spark column has discrete structure. Instead of one plasma, the authors explain the process through the formation of numerous plasma events that consist of micro-plasma balls, micro-bubbles and spherical shock waves. Because plasma is formed around inclusion particles, initial characteristics and size of micro-plasma balls will depend on the nature and concentration of suspended particles.

Effect of focusing conditions – Dependence of LIB threshold on various conditions is rather complex, since numerous parameters are combined and mutually dependent. Further complication is introduced since the two main mechanisms for breakdown in liquids (avalanche and multiphoton ionisation) also tend to intersect in some regimes. Wavelength dependence of the two breakdown mechanism is the opposite: longer wavelengths favour the breakdown through the cascade ionisation, and in short wavelength range primary mechanism for LIB is multiphoton ionisation since inverse bremsstrahlung absorption needed for the cascade ionization has low efficiency. One of the laser beam parameter with biggest influence is focusing and spot size in medium. Spot size can influence cascade breakdown threshold in two ways: through free electron losses due to diffusion during the buildup process, or variation in minimal density required for initiation of avalanche. For pulses of longer duration, smaller spot size will mean higher threshold, because one has to include the influence of diffusion, primarily in the cases of microsecond regimes or longer. When working with the smaller beam diameters, initial minimal densities required to initiate a breakdown are higher, in order to ensure enough free electrons in the focal volume. This means that less number of cascade multiplications is needed to reach the breakdown threshold, but still, the spot size dependence is weak. Multiphoton initiated breakdown threshold should also experience small influence of spot size but in the opposite direction: smaller spot size, higher threshold. This means that for the pure water, where threshold for breakdown is determined by multiphoton ionisation, decreasing the spot size will lead to higher thresholds for breakdown. For very impure media there should not exist dependence on spot

size. When level of impurity is low enough or spot size small enough multiphoton initiation of breakdown process is required, just like in the case of the pure water. In addition, the optimal focusing is extremely important whenever the stable position of the LIB and plasma is of importance, as is the case for LIBS technique. Reasons for fluctuating position of LIB and multiple plasma formation as those observed in (Toker *et al.*, 2009) can be multiple breakdown on impurities, probabilistic nature of the breakdown and finding seed electrons in the focal volume, interaction of the later part of the laser pulse with the formed plasma causing forward movement of the plasma towards the laser, 'hot-spots' in the focal region and self-focusing, etc. Recent papers (Tian *et al.*, 2016)(Tian *et al.*, 2015) report well localized, stable plasma position with one core obtained with tightly focused laser beam and large focusing angles.

2. LIB on a submerged target

The process of LIB in the presence of the solid target in the liquid is somewhat different than previously described LIB in the bulk liquid. The LIB threshold is much lower than for the bulk liquids, since the initial free electrons are more easily obtained from the solid target. During LIB on the submerged target, part of the input laser radiation transmitted through the liquid column reaches the sample and heats it locally up to the boiling or decomposition temperatures in order to achieve efficient evaporation. (Noll, 2012) The process is largely dependent on the sample material in the question, since the amount of the temperature rise will be influenced by the efficiency of the laser-material coupling, which on the other side, depends on the thermal conductivity of the material. If the laser energy surpasses the characteristic threshold which depends on the sample material, the electrons are cut free from the atomic nuclei by multiphoton ionisation. Once the initial free electrons are created, they can continue to absorb the laser photons through the process of inverse Bremsstrahlung (for ns pulses). Through this process, electrons increase their kinetic energy, which leads to the more efficient ionisation through the impact collisions. As a result, dense plasma is formed together with two strong shock waves, one on the liquid side and laser-induced stress wave (LSW) on the solid side.

Due to the interaction of the pulsed laser beam with the target, ablation and expulsion of the material occurs. This ablated mass is partially evaporated and ionized, forming the plasma state. The remaining part of the ablated material is removed

from the target in different forms (vapour, particles, liquid droplets) and later on it can form particulates in the interaction region. If the concentration of this particulates is too high, great deal of the laser energy will be spent before reaching the target. In addition, particles can also act as a preferential breakdown sites which provide initial seed electrons, and produce parasitic breakdown in the liquid before the target. For that reason, it is necessary to frequently exchange the liquid or to use flowing systems when performing the LIBS measurements on the submerged targets. (De Giacomo *et al.*, 2007)(Musazzi and Perini, 2014) Comparison of the laser ablation process in the pure liquid and colloid is reported recently (Chen *et al.*, 2017), concluding that much less energy was reaching the target in the case of the colloid, resulting in the smaller size of the nanoparticles. Besides keeping the impurity concentration low, for laser ablation inside liquid optimal focusing is very critical. Optimal focusing conditions with respect to the stable and reproducible LIB event on the target surface, are achieved when the target is placed above the nominal focal point of the focusing element. Images obtained with photoelasticity imaging technique developed by (Nguyen *et al.*, 2013) to observe the LSW in the solid target, shows that placing the target at the exact focal position results in elongated plasma of very poor reproducibility, see Fig. 4.1

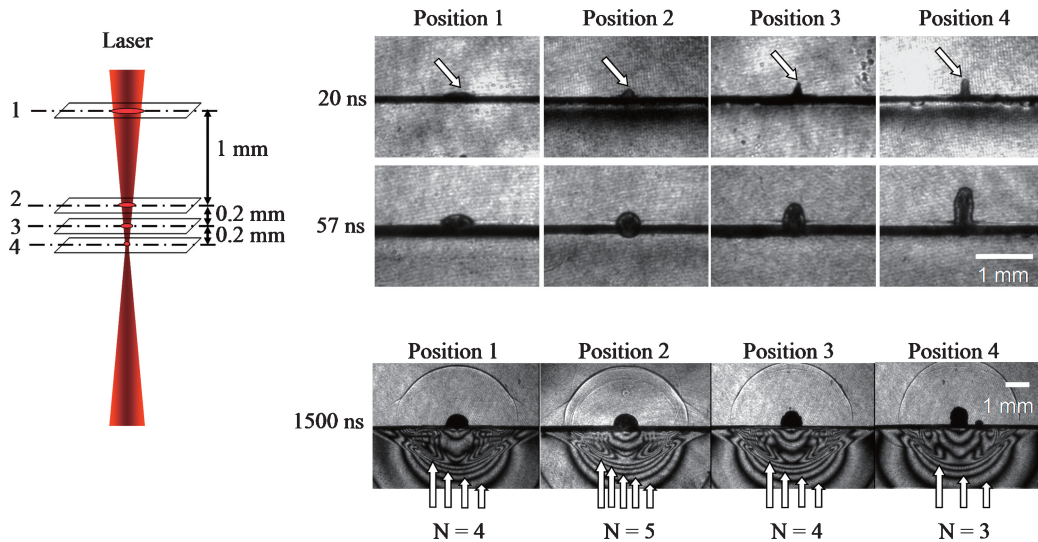


Figure 4.1: Dependence of the LIB on submerged target on the focusing conditions, (Nguyen *et al.*, 2013)

This position also reduces the advantages of the laser processing underwater, since the intensities of the generated LSWs are much weaker, based on the number of fringes detected in the target. This is the consequence of the columnar plasma shape, whose front efficiently absorbs the remaining part of the laser pulse energy

and increases its volume, thus decreasing the confining effect of the liquid.

4.2 Properties of the laser produced plasma in liquid environment

Laser produced plasma is transient system that undergoes fast changes during its evolution. When LIP in the liquid is created with the nanosecond pulse duration laser, initially formed vapour plume can gain energy from the remaining part of the laser pulse. This produces heating of the electrons through the process of the inverse Bremsstrahlung absorption and photoionisation of the heavy species. Absorption of the laser radiation depends on the laser wavelength and it can be calculated from the Maxwell equations and equation of motion for free non relativistic electrons (Noll, 2012). Taking the typical conditions of a laser-induced plasma for LIBS into account simple expression for the absorption coefficient can be obtained

$$\alpha = \frac{\nu}{c} \frac{\omega_p^2}{\sqrt{1 - (\omega_p/\omega)^2}} \quad (4.1)$$

where ω is the angular frequency of the laser radiation, c is the vacuum speed of light, ν is the collision frequency of electrons with ions and atoms and ω_p is the plasma frequency given by the equation

$$\omega_p = \sqrt{\frac{n_e e^2}{\epsilon_0 m_e}} \quad (4.2)$$

LIP produced in liquid or on the submerged target has initially very high electron number density $N_e > 10^{19} \text{ cm}^{-3}$ due to the strong confinement which limits the expansion rate. Such a high electron number density strongly decreases the ionisation energies of the species, due to the Debye effect on the potential energy of the bounded electrons. (De Giacomo *et al.*, 2012) As a consequence, the ionisation degree is almost unity, i.e. ablated material is fully ionised and almost all excited energy levels are forbidden due to the ionisation potential depression. Balance of the processes in this kind of plasma is moved from excitation-deexcitation to recombination-ionisation pair.

High electron number density coupled with the high ionization degree leads to the very strong continuum radiation due to the prevalence of the recombination processes. Such an environment is suitable for the intensive chemical reactions through

which the molecular species are easily formed, and relatively early on from the onset of the plasma (few hundreds of nanoseconds), compared to the times of the molecular formation in the LIP in gaseous surrounding (several μs). This is also the explanation for the widespread usage of the laser ablation (LA) in the liquid for nanoparticles production. Efficiency and yield in the nanoparticles production is largely dependent on the ablation mechanisms and material removal during LIB on submerged target. Material removal during LA in the liquid occurs in several distinctive phases. (Lazic and Jovićević, 2014) Up to $\sim 100\text{ns}$ the material is evaporated by the laser and hot plasma, and afterwards, intensive material expulsion begins due to the impact of the compression wave, which moves towards the target during several hundreds of ns. In some experiments (Lazic *et al.*, 2013a)(Gavrilović *et al.*, 2016) (Gavrilović *et al.*, 2017), additional phase of material removal is detected, where slow target evaporation occurs in the interval when the cavitation bubble is already well developed. In this late stage of LIB, cavitation bubble plays significant role in sustaining the plasma emission and thus producing additional material ablation, since the thermal exchange between the target and bubble is significantly smaller than it would be between the target and the liquid, which enables high temperature state of the material to last longer. Additional possibility for material ablation is the collapse of the cavitation bubble, in the cases when the impact jet is formed. (Takada *et al.*, 2010)

4.2.1 Optical emission spectroscopy of laser-induced plasmas in liquid (LIBS)

Laser induced breakdown LIBS (Cremers and Radziemski, 2006) is a powerful tool for in-situ elemental analysis in different surroundings (gases and liquids) and at different ambient pressures. The technique is based on a plasma generation by an intense laser pulse with duration in nanosecond range or shorter. From spectrally resolved emission of the plasma containing excited atoms and ions belonging to sample constituents, the material composition can be determined, see Fig. 4.2. LIBS is practically the only existing technique for in-situ chemical analysis of bulk liquids and of submerged solid samples. (Guirado *et al.*, 2012) Complete and thorough characterization of LIB in liquid has posed a difficult scientific problem, both for experimental and theoretical investigations, because of the number of involved complex phenomena and complexity of the media itself (water or other liquid). Despite

its wide range of applications, due to its peculiar structure, water still represents especially complicated and interesting case of liquid with lots of unknowns during the interaction with the high-irradiance laser beams. (De Giacomo *et al.*, 2012)

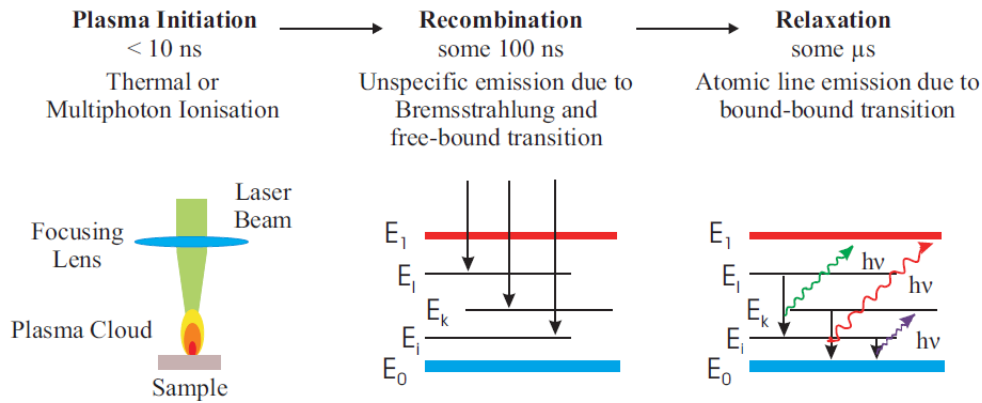


Figure 4.2: Laser-induced plasma initiation and the recombination and relaxation of emission lines,(Koch, 2012)

High acoustic pressure and long duration shock wave in liquids with respect to gas environment lead to a manifold increase of the LA efficiency and also to a lowering of the ablation threshold(Wook Kang— *et al.*, 2008). Although the ablation rates inside liquids are higher than in a gas environment, the LIBS signal at equivalent laser excitation is significantly lower than in the presence of sample-air interface(De Giacomo *et al.*, 2007)(De Giacomo *et al.*, 2005). Liquid environment has several disadvantages for LIBS signal, among them are short lived optical emission, fast plasma quenching, broadening of the very few emission lines, intense continuum radiation and pronounced effect of the radiation self-absorption. Plasmas in the liquid emit strong continuum radiation in the range from ultraviolet to infrared due to the bremsstrahlung from free electrons and electron-ion recombination. This continuum is the strongest immediately after the laser pulse impacts the target but after it diminishes, instead of intense atomic and ionic lines, as usually seen during LIB in gaseous surrounding, in underwater LIBS very often no analytical useful signal can be detected. This is the consequence of the short plasma duration in the liquid surrounding compared to the gaseous one. In some of the experiments on the SP LIB in liquids the continuum was the only spectral feature that could be recorded(De Giacomo *et al.*, 2011) (Suzuki *et al.*, 2002)(Ushida *et al.*, 2007) Although the continuum can also be used as a spectroscopic tool to study the characteristics of the plasma, see. e.g. (De Giacomo *et al.*, 2010), it doesn't provide elemental specific

information which can only be obtained from the well resolved atomic spectra. Besides high electron number densities, the underwater plasmas have substantially lower temperatures compared to the LIP in the gases. This is a consequence of the better thermal dissipation capacities of water compared to the air and vacuum and large energy losses in mechanical effects and in liquid evaporation. Also a presence of hydrogen from water strongly contributes to an effective thermalisation and cooling of the plasma. Besides rapid thermalisation, oxidation is also very intensive in underwater plasma, since the ionization energy of the water molecule is much lower than oxygen molecule, and hence in water surrounding abundance of oxygen atoms is increased compared to the gaseous surrounding. But, despite the abundance of the oxygen and hydrogen atoms in LIP under water, low plasma temperature disables the excitation of the highest excited energy levels, and thus, surprisingly, hydrogen and oxygen emission are rarely observed in the LIP in the water, with few exceptions (Escarguel, Ferhat, Lesage and Richou, 2000)(Kumar and Thareja, 2010) As mentioned previously, LIP in liquid is very suitable environment for chemical reactions through which the diatomic molecules are formed, and their emission is easily obtained due to the relatively low temperatures.(Sakka *et al.*, 2005) (Lam *et al.*, 2014) Therefore one of the suggestions for characterisation of the LIP plasma in water is to use this molecular band emission to probe the temperature conditions and temporal evolution of the chemical composition. (Lam *et al.*, 2016) These poor spectral properties of the SP LIBS require the use of optimal gated and delayed acquisition, which is usually reported to be in the order of 100 ns. (Lazic and Jovićević, 2014)

The specific combination of high density (10^{18}cm^{-3}) and low temperatures ($\sim 6000\text{-}15000\text{ K}$) makes the underwater plasma extremely hard for characterisation, due to the breaking of many assumptions used in the spectroscopic theories due to the plasma non-ideality. The usual parameters that are determined with spectroscopic measurements are plasma temperature, obtained usually from the Boltzmann plot method, and electron number density determined usually using Stark effect(Griem, 1974). In the conditions when plasma deviates from ideality and correlation effect are important, corrections to the Stark line broadening will also be needed. This area of plasma research is far more complex and less understood than the ideal plasma case (Fortov and Iakubov, 2000). Convenient parameter for describing plasma deviation from ideality is the coupling parameter Γ (Stambulchik *et al.*, 2007), defined for a single-species gas of charged particles with charges z_s and

temperature T as

$$\Gamma_s = \frac{z_s^2 e^2}{r_s k_B T} \quad (4.3)$$

where e is the electron charge, k_B is the Boltzmann constant, and r_s is mean interparticle distance given by $r_s = (4\pi N_s/3)^{-1/3}$ Eq. 4.4 can be rewritten using the expression for Debye length $\lambda_s = \sqrt{(k_B T/4\pi N_s e^2 z_s^2)}$ in the following form

$$\Gamma_s = \frac{1}{3} \left(\frac{r_s}{\lambda_s} \right)^2 \quad (4.4)$$

Due to the correlation effects in the plasma, corrections to the Stark line parameters are expected to be the same order of magnitude as coupling parameter value, in so called, weakly-coupled plasmas. In weakly-coupled plasmas only the coupling between the radiator, high Z -ion and the rest of the plasma is not negligible. But situations is even more complicated in the case of low temperature dense hydrogen plasma, where the interactions between the perturbers and corresponding correlation effects can not be neglected. Hydrogen in dense, non-ideal plasmas have been studied by many research groups and many opposing opinions and theories have been developed (Kielkopf, 1995) (Stambulchik *et al.*, 2007) (Kielkopf and Allard, 2014) (Vitel *et al.*, 1996) (Büscher *et al.*, 2002) (Böddeker *et al.*, 1993) (Griem, 2000) (Calisti *et al.*, 2007) (Alexiou and Leboucher-Dalimier, 1999). Especial controversy arose about the measurements of shifts and widths of the H_α line given in (Escarguel, Ferhat, Lesage and Richou, 2000) (Escarguel, Oks, Richou and Volodko, 2000) for the underwater laser produced plasma, which were discussed in several publications (Stehle *et al.*, 2000) (Alexiou, 2005) (Griem, 2001) (Halenka, 2004) (Griem *et al.*, 2005)

Despite all the difficulties connected with the SP LIBS and complexity of the plasmas produced inside liquid environment, applications which demand rapid, in-situ, non-contact analysis, all of which are the advantages of the LIBS, make that interest in the subject of the laser produced plasma under water continuously grows. This produces the need for the knowledge about the physics behind the process hence, the less examined interrelations between the bubble and plasma emission during SP LIB on submerged target are closely examined in this study.

Chapter 5

Experimental techniques for underwater Laser Induced Breakdown diagnostics

The laser induced breakdown on a solid target was generated using a Nd:YAG laser (Molelectron MY34) operated at 1064 or 532 nm , with 20 ns pulse duration and a pulse energy of 40 mJ. The laser was run in low repetition rate (up to 5 Hz) to ensure proper ablation event with every laser pulse and avoid time overlapping of successive breakdown events. The laser beam was focused perpendicular to the target plane by two quartz planoconvex lenses L_1 ($f_1 = 100$ mm) and L_2 ($f_2 = 68$ mm), where the second lens was mounted directly on the chamber wall. The advantage of the lens embedded in the chamber wall is that the focused laser beam propagates entirely inside the breakdown medium, thus avoiding aberrations on the air-glass-liquid interface (Kennedy *et al.*, 1997). Additional advantage is that there is no splashing of the liquid which is known to pose a problem in underwater laser ablation (De Giacomo *et al.*, 2007) and the possibility of damaging the optical components is thus minimized. The combination of the two lenses enabled smaller focusing angles and tighter focusing on the target. Also, the additional lens in front of the embedded one provided more flexibility during optimization of the focusing conditions. Simply by changing the separation between the two lenses location of the combination focal point given by the equation

$$s_2 = \frac{f_2(f_1 - d)}{f_1 + f_2 - d} \quad (5.1)$$

could be changed. The fact that the lens focal length becomes longer in water due to the higher refractive index compared to air was taken into account. The limiting factor was only the chamber's dimension, or more precisely, the dimension of the viewing lateral window (25.4 mm). The chamber was made in the laboratory from optically transparent polycarbonate sheets (12 x 8 x 0.5 cm³). The chamber was equipped with two quartz windows w_1 and w_2 , used for the lateral observation of the plasma and the vapour bubble. Several chamber dimensions and focusing conditions were tested before the optimal geometry for stable and reproducible breakdown event was found. Under the optimized conditions, the focal plane of the focusing system was slightly below (~ 0.5 mm) the surface of a target. This position of the focus was already reported by (Nguyen *et al.*, 2013), as optimal in respect to the the most reproducible plasma with the stable position above the target surface. In this way, undesirable breakdown on the suspended particles before the target surface (Cristoforetti *et al.*, 2012) was avoided, Fig.5.1



Figure 5.1: Photograph of the breakdown event with non-optimized (left) and optimized focusing (right)

Different target materials were investigated, metals, ceramics and semiconductors, but the main part of the results regards the aluminium containing targets, namely pure Al (99.999%) and a ceramic α -alumina target. Both target materials have very widespread use and significant part of the research connected to the underwater laser ablation was performed with this type of materials. The target was placed vertically inside a chamber filled with 700 ml of the liquid in the final chamber version. The target was mounted on the target holder and shifted by 1 mm after each laser shot to exclude the influence of the formed crater on subsequent plasma formation. Vast majority of the results were obtained for distilled water, while some experiments were performed in the tap water and etil-alcohol. The optical path length of the laser beam through water in final configuration was ~ 3 cm. To estimate the losses of the input laser energy through the water column BeerLambert

law was used 2.3 as in (Lazic and Jovićević, 2014) with water absorption coefficient $\alpha = 0.072 \text{ cm}^{-1}$ derived from the imaginary part of the refractive index k (Kou *et al.*, 1993) using the equation

$$\alpha = \frac{2\pi k}{\lambda} \quad (5.2)$$

By applying this approximation estimated laser energy reaching the target surface was 60% of the input laser energy. Based on the crater diameter on the target surface ($250 \pm 25 \mu \text{ m}$), the estimated fluence within an error of 12% was about 45 Jcm^{-2} (2.25 GWcm^{-2}). Water inside the chamber was periodically exchanged to avoid scattering on the particles produced by LA of the sample. The appearance and mutual position of the chamber, target and associated optics is given in Fig.5.2.

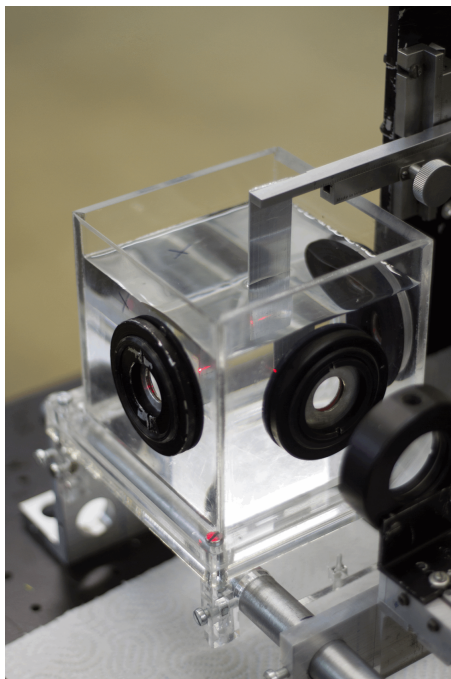


Figure 5.2: Photograph of the interaction chamber and the target holder

Since the processes occurring after the laser target interaction in liquid surrounding are numerous and extremely fast, the whole picture and full understanding can be obtained only by applying different experimental techniques. Most of the used experimental techniques in this work belong to the class of so called fast imaging techniques, from which we can distinguish plasma imaging, shadowgraphy and Schlieren techniques. Those techniques enabled insight in the spatio-temporal evolution of the plasma, cavitation bubble and shock wave, respectively. The disadvantage of these techniques is that by using single frame iCCD camera one can record only one time

delay from one laser shot, so in order to obtain full time evolution consecutive laser pulses need to be applied. This implicitly calls for high stability and reproducibility of the breakdown event, the condition less stringent for the case of the submerged target than for the pure liquid, but still pretty demanding. To check the correctness of such analysis complementary techniques of the transmission and scattering were applied, where with one probe beam and from one pulse whole time evolution is obtained, but without spatial resolution. Optical emission spectroscopy was used as irreplaceable tool for elemental analysis of the material's composition and characterisation, and for the plasma diagnostics. In following brief explanation of these experimental techniques will be given and used experimental setups explained.

5.1 Fast imaging techniques

5.1.1 Plasma imaging

Fast imaging was performed through the lateral window w_1 by using a biconvex achromatic lens L_3 ($f_3 = 100$ mm) and a photographic objective lens OL (focal length 75 mm, f 1.5) mounted with macro-bellows on an iCCD camera (Andor Technology, model DH734I-18U-03, with 1024 x 1024 pixels, 13 x 13 mm size, 18 mm intensifier diameter), see Fig.5.3. The optical magnification of the system was determined using a reference object and the dispersion (0.01176 mm per px) was calculated for subsequent recordings. The iCCD was controlled using a pulse generator (DG-535, Stanford Research Systems), triggered optically by a fast photodiode that captures the laser beam partially reflected on mirror M_2 . The acquisition gate width was varied between 15 ns and 50 μ s. Shorter acquisition widths at earlier delays were favourable to be able to track fast changing plasma shape and size. Accumulation of the signal was necessary at longer delays due to the very weak signal, but was nevertheless performed also for the early delays to exclude the influence of the eventual shot-to-shot changes in appearance. Images of the plasma were accumulated over 5 laser shots, except for long delays (hundred of μ s from the laser pulse) where mainly 10 pulses were used.

5.1.2 Shadowgraphy and Schlieren techniques

Shadowgraph and Schlieren techniques allow us to see the optical inhomogeneities in transparent media, or schlieren, normally not accessible to our vision (Settles,

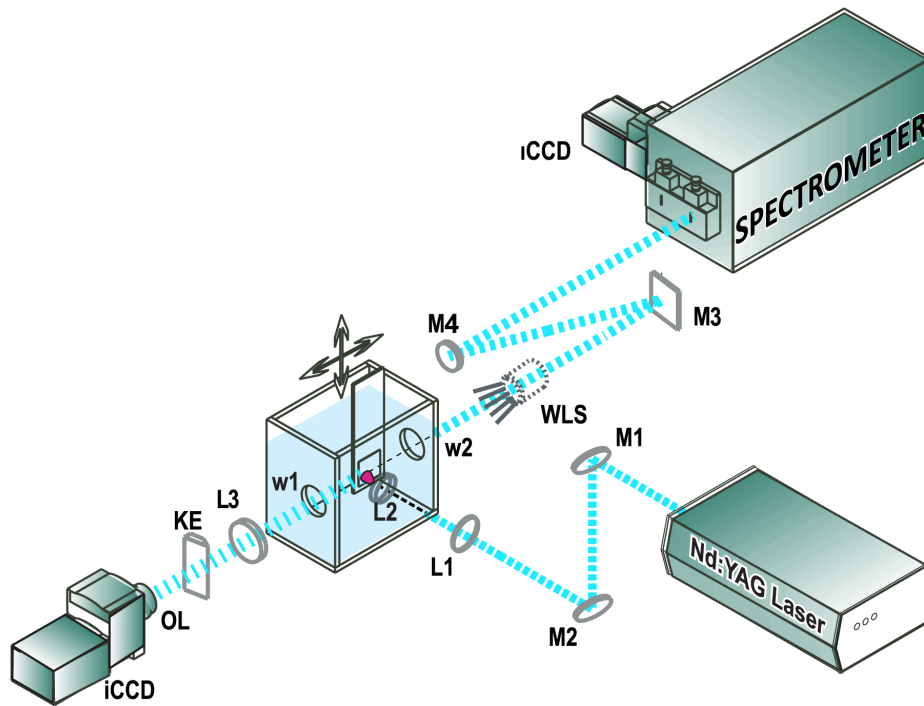


Figure 5.3: Experimental setup for fast imaging techniques: L_1 - L_3 – lenses, M_1 - M_3 – flat mirror, M_4 – concave mirror, WLS – white light source, KE – knife edge, OL – objective lens, and w_1 and w_2 – quartz windows.

2006),(Vasil'ev, 1971). Schlieren exists in liquid, solid and gaseous surroundings. It can emerge due to the temperature changes, fast flows or mixing of different materials. Both the shock wave and the bubble represent significant disturbances of the refractive index of the surrounding media and as such are perfect candidates for the Schlieren and shadowgraphy studies. More about the basic concept of this techniques can be found in the ref. (Settles, 2006),(Vasil'ev, 1971). The same optical setup previously described in Section 5.1.1 was also used for shadowgraphy adding illumination using a white light source (WLS). The light from the WLS (halogen lamp, 80 W) was guided by a fiber bundle (diameter 6 mm) to the chambers lateral window w_2 , providing evenly distributed illumination over the observation volume. The same setup was used for the Schlieren imaging, where a vertically mounted knife edge KE was positioned in the focus of lens L_3 , thus monitoring the refractive index gradient perpendicular to the sample. For shadowgraphs and Schlieren images only one laser pulse was applied and the gate width was varied between 20 ns and 2 μ s. Due to very bright plasma emission and not enough intense back illumination the earliest delays of the bubble and especially shock wave formation couldn't be clearly

discerned with the used experimental setup.

5.2 Transmission and scattering with the probe beam

Light propagation through the region in which the interaction of the laser beam with the target in the liquid has occurred is highly affected by the optical and physical properties of the evolving bubble. To study this more closely the probing techniques of transmission and scattering were applied. Transmission measurements were performed under illumination of 2 mW HeNe laser, Fig 5.4. The laser beam was expanded to ~ 5 mm diameter and sent through the chamber windows parallel to the target surface. On the opposite side of the chamber photomultiplier tube (PMT) EMI 9659QB with interference filter (IF) for He-Ne wavelength was placed and used for the detection of transmitted radiation. For the scattering measurements probe was green laser diode beam sent through the beam expander and directed on the target with incidence angle of $\sim 60^\circ$, Fig5.4b. The scattered light was collected through chamber window and focused with lens L3 ($f=5$ cm, diameter 5cm) onto the entrance slit of PMT equipped with suitable IF. The signal from the PMT was monitored on the oscilloscope (model TDS2024C) and saved for the later processing.

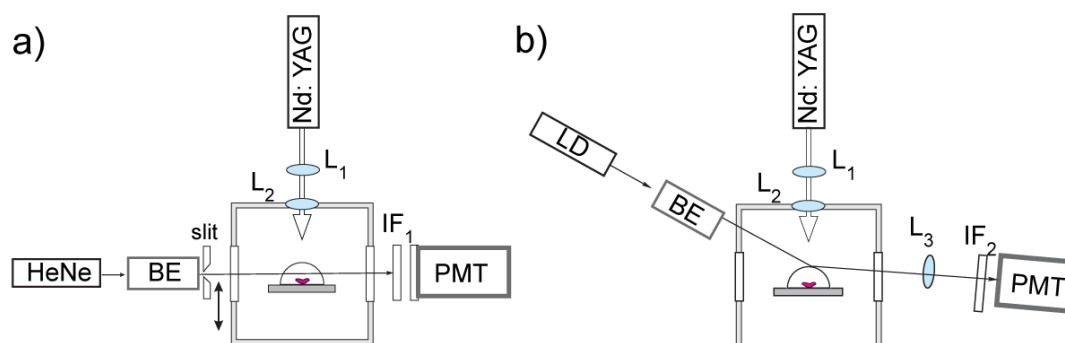


Figure 5.4: Experimental setup for probe techniques: a) transmission b) scattering
 L_1 - L_3 – lenses, BE – beam expander, HeNe – helium-neon laser, LD – green laser diode, IF_1 , IF_2 – interference filters, PMT – photomultiplier tube

5.3 Optical emission spectroscopy (OES)

Two setups were evaluated for optical emission spectroscopy measurements. In the first configuration plasma emission was recorded using setup shown in Fig5.5. Image of the plasma plume was projected onto the entrance slit (10 m width and 2.5 mm height) of the spectrometer (Shamrock sr-303i, Czerny-Turner type, focal length 303 mm, with the three gratings of 2400 grooves/mm, 1200 grooves/mm and 300 grooves/mm, $f/4$) using lens L_3 ($f_3 = 170$ mm). The plasma radiation was recorded with the iCCD detector (Andor Technology, model DH720-18F-63, with 1024×256 pixels, $26 \times 26 \mu\text{m}$ pixel size, 18 mm intensifier diameter) mounted on the exit slit plane of the spectrometer.

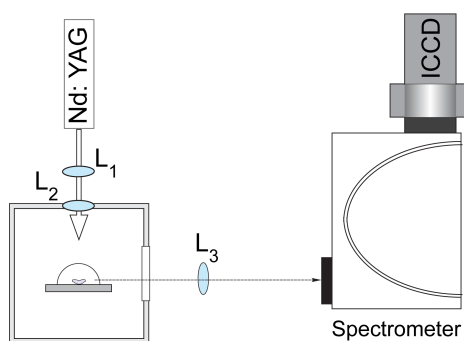


Figure 5.5: Experimental setup for optical emission spectroscopy with lens

To avoid problem of chromatic aberrations introduced by the lens and to extend wavelength optical range to the UV part of the spectrum, setup with mirrors was tested and afterwards used for the rest of the OES measurements. By using mirrors instead of the lenses for image projection the dependence of the focal length on the thickness of the liquid layer is also excluded. In this setup the 1 : 1 image of the plasma plume was projected, by means of optical mirrors M_3 and M_4 (see Fig.5.3) on the entrance slit ($100 \mu\text{m}$ wide) of a 0.5 m Ebert-type spectrometer, $f/8.6$ equipped with a grating of 1180 grooves per mm. The iCCD detector, previously used for the fast imaging techniques (Andor Technology, model DH734I-18U-03), was mounted at the spectrometers exit plane and operated in an imaging mode. Advantage of this camera in respect to the other one used for OES in lens configuration is in extended wavelength range that covers due to the quartz entrance window (180-850 nm), smaller pixel size and the fact that image intensifier covers the whole matrix of pixels. After construction of the suitable adapters to fit the camera onto the one of

the exit ports of the spectrometer, it was necessary to do the wavelength calibration of the system. This calibration and instrumental profile recording was performed using low pressure Hg and Ne spectral calibration lamps. Resulting calibration curves are shown in the Fig.5.6.

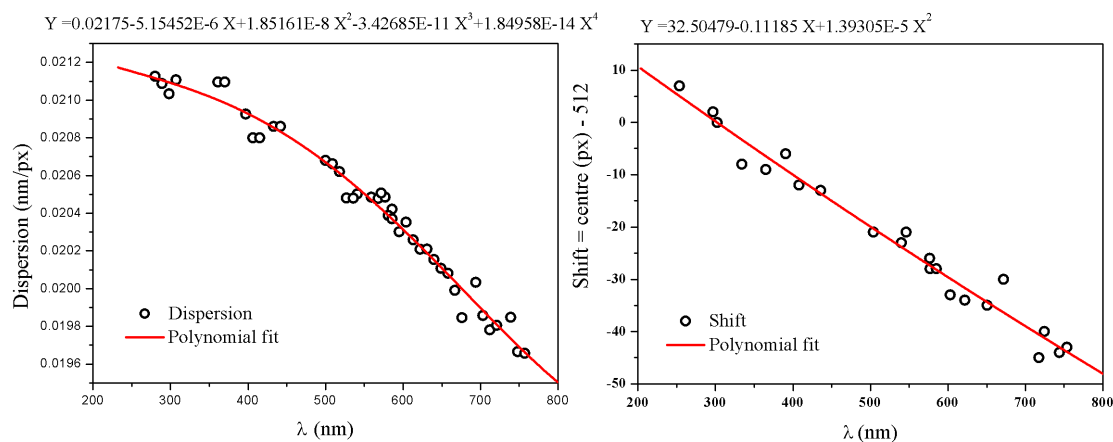


Figure 5.6: Wavelength calibration of the Jarrel-Ash spectrometer with the mounted DH734I-18U-03 iCCD camera

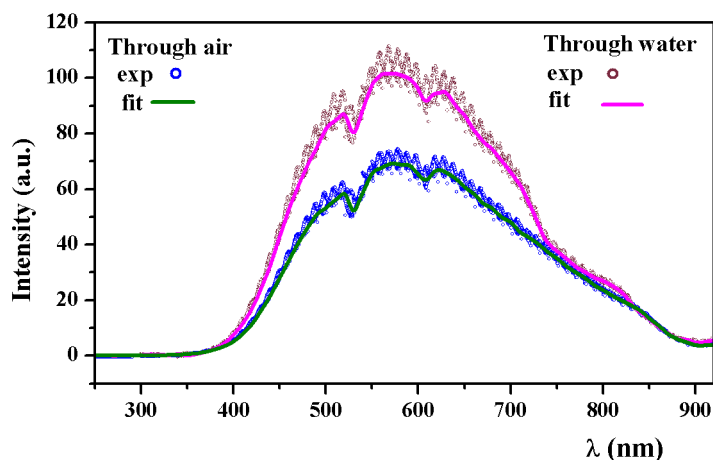


Figure 5.7: Calibration curve - Intensity calibration: Without and with the water in the chamber

The sensitivity of spectrometer, ICCD system and all optical elements in the setup with mirrors was calibrated against standard tungsten coiled-coil filament quartz halogen lamp (EGG, model597-1). The calibration curve was made for the two cases, with and without the water in the chamber. The whole spectral range from 200 nm to 900 nm was covered, but only the calibration curve for the wavelengths larger than 300 nm was used, since for the proper calibration at wavelengths

Table 5.1: Instrumental apparatus and components – final configurations

Component	Specification
Nd:YAG laser	Molelectron MY34, $\lambda = 1064$ nm, $\tau = 20$ ns, $E=40$ mJ
Spectrometer	0.5-m Ebert-type (Jarrell Ash 82-025)
Pulse generator	DG-535, Stanford Research Systems
iCCD camera	Andor Technology, model DH734I-18U-03
Chamber	Made of optically transparent polycarbonate sheets
Target	Alumina (α -Al ₂ O ₃) and pure Al (99.999%)
Nd:YAG Dual laser Line mirrors M ₁ and M ₂	BK7, diameter 25.4 x 6 mm, 450, 99.5%, 532 + 1064 nm, YAG 1H + 2H
Mirrors M ₃ and M ₄	Plain with aluminized surface M ₃ , concave mirror focal length 50 cm with aluminized surface M ₄
Lenses L ₁ , L ₂ and L ₃	Quartz plano-convex lenses L ₁ focal length 100 mm and L ₂ focal length 68 mm, biconvex achromatic lens L ₃ focal length 100 mm
Objective lens OL	focal length 75 mm, f1.5
Windows	Quartz windows w ₁ and w ₂
Light source WLS	White light source with fiber bundle (diameter 6 mm)
IF ₁ , IF ₂	Interference filters for 525 and 650 nm wavelength

lower than 300 nm deuterium lamp is needed. Spectral recordings were made with large overlapping, i.e. for each recording wavelength was changed for 10 nm, so the percent of overlapping points in two successive recording was 50. Resultant calibration curve is shown in Fig.5.7.

The spectra were reconstructed by averaging over spatial axis in the spectral recordings. Each LIBS spectrum was an accumulation over 160 laser pulses, where each laser shot was delivered to a fresh spot on the target. Reproducibility of the breakdown events - LIP - was monitored with photo-diode, simultaneously with ICCD recordings. In order to improve reliability of the measurements, shots which had signals from the photo-diode that deviated from some average signal were not taken into account. Summary of instrumental apparatus and components used in the final configurations for all experimental techniques is given in the table 5.1.

5.4 Data acquisition and processing

Data obtained from the fast imaging techniques are all in the matrix form. On the image matrices some basic techniques for image manipulation and quality enhance-

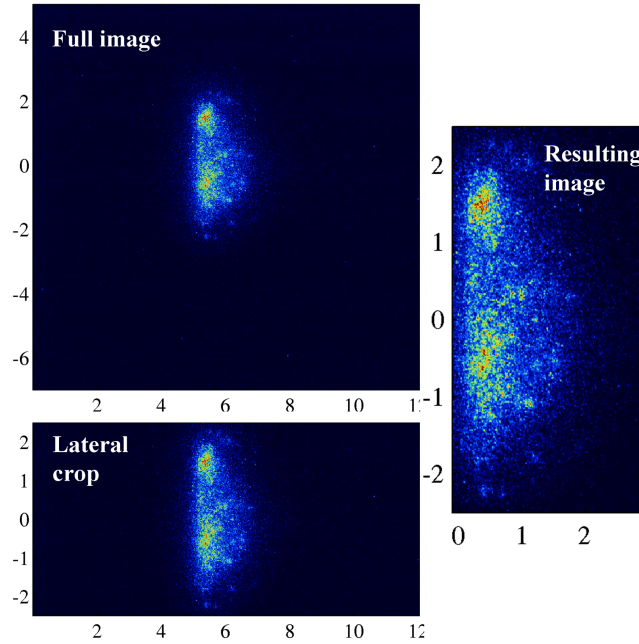


Figure 5.8: Example of the image cropping

ment were applied (manipulating the contrast, histogram, colormaps etc.). Routine written in the Matlab[®] was used for correlating the pixel values and position in respect to the target, based on the predetermined dispersion value. To be able to measure the sizes of the plasma, bubble and position of the shock front, slight adjustments in the null position (target surface) between successive recordings were applied (± 3 px). After centering and transferring from pixels to millimeters, image cropping was performed. In the program there was the additional option from image symmetrisation and smoothing. The example of basic image cropping procedure is shown in the Fig.5.8.

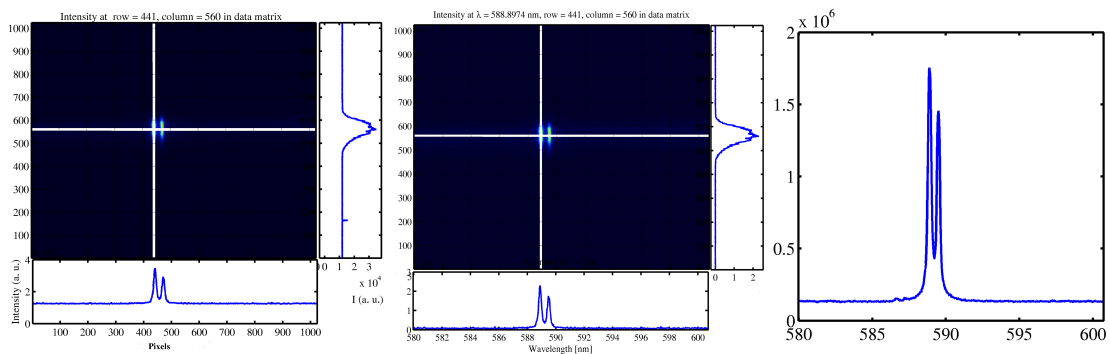


Figure 5.9: Spectral data manipulation: a) raw image b) image after background subtraction and conversion in wavelength c) spectra obtained after summing the pixels (vertically) with the useful signal

Regarding the processing of the spectroscopic measurements, the routine was

made to assign wavelength vector to matrix based on the name of the recorded file. The file name had to be in the format `xxxx_xyyyyyyy.sif` where `xxxx_x` is central wavelength in angstroms read from the spectrometer and the rest of the characters are chosen arbitrarily. By using the determined values of dispersion and shift (see Fig.5.6) and central wavelength from the input file name, the wavelength vector was calculated and added to the matrix. For each recorded spectral range and every set of experimental conditions (different gate widths on the sensor or different number of accumulations applied) the image in the absence of the breakdown event was recorded and subtracted from the plasma image. After that step, due to the low signal intensity and strong continuum the binning of the pixels with the useful signal (pixels whose intensity represent spectral emission) was performed. The care was taken that spectral image falls approximately on the center of the sensor since in that part sensor has the best linearity of the response. By selecting only the part of the sensor with the useful signal and by averaging over that part, the level of noise was significantly reduced compared to the case of the Full Vertical Binning (FVB), where the whole spatial direction is integrated. The procedure is illustrated in the Fig.5.9.

Few additional procedures used for specific tasks during image and spectral data processing will be explained in Section 6 .

Chapter 6

Results

6.1 Plasma evolution

Peculiarities of the plasma formation and evolution inside the liquid environment were captured using fast photography. Striking differences are immediately observed when compared to the plasma evolution in the air at atmospheric pressure. Example of the plasma evolution and formation on α -alumina in air and in distilled water are given in Fig. 6.1. The most notable difference is reflected in the dimensions of the two plasmas and their expansion speed into the background environment. When laser induced plasma (LIP) is formed in gaseous surroundings it can expand for several millimeters away from the target, depending among other factors, on the pressure of the background gas. In contrast, water has significantly higher density and orders of magnitude higher compressibility, both leading to very effective plasma compression and its small size. As a consequence, a typical size of the plasma inside liquid doesn't go over 0.5 mm. Besides its small size, intensity of the plasma radiation is decaying much faster compared to the plasma in gaseous surroundings, due to the pronounced energy losses into mechanical effects, bubbles and shock waves. This rapid energy loss leads to the fast cooling of the plasma, accompanied by high recombination rate which contributes largely to the poor spectral characteristics of the plasmas in liquid.

Besides being extremely small in size, plasma produced by laser ablation underwater is usually quoted to have very short duration of emission (De Giacomo *et al.*, 2007)(Sakka *et al.*, 2002)(T.Tsuji *et al.*, 2007)(Saito *et al.*, 2002)(Kim *et al.*, 2015)(DellAglio *et al.*, 2015), and this is another big difficulty for experimental stud-

ies. Returning again to the Fig.6.1, although the small plasma size is also detected in this experiment, plasma persistence is substantially longer than usually stated in SP LIBS $1\mu\text{s}$. To put in evidence extremely long plasma persistence following laser ablation in liquid, series of photographs captured after laser ablation of aluminium is given in Fig. 6.2. Similar long emission also exists on alumina target, and difference between the plasmas on different target materials will be discussed in Sect. 6.5

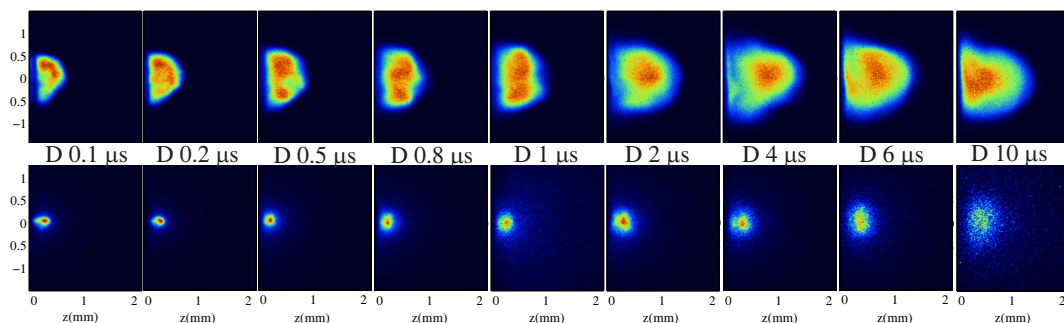


Figure 6.1: Fast photography of the plasma evolving from the target (placed on the left) captured at different delays D from the laser pulse in air at an atmospheric pressure (upper row) and in distilled water (lower row). Laser energy was 40 mJ.

From the photographs it can be seen that detected plasma emission changes significantly during the time and part of the explanation for this long plasma lifetime lies exactly in this change of the plasma's shape. In the first microsecond after the laser pulse usual picture of underwater plasma - very bright and very small plasma confined by surrounding liquid to only $400\mu\text{m}$ diameter, is seen. At about 400 ns from the laser pulse the plasma expansion perpendicular to the target slows down drastically; its further expansion occurs mostly in the direction parallel to the target surface. In this stage the plasma has a flat shape where its length parallel to the target is almost twice the height (direction normal to the target). The flat shape of the plasma is dominant until $\sim 10\mu\text{s}$ and afterwards expansion is more pronounced and characterized by the formation of glowing centres and their clustering. A flat plasma shape on submerged metallic targets was observed by different authors, (Thornton and Ura, 2011) (Oguchi *et al.*, 2007), but a long lasting emission (well beyond $1\mu\text{s}$) was reported only recently. (Lazic *et al.*, 2013a).

However, there are some studies that discuss about light emission on a longer timescale of a few microseconds. (Lam *et al.*, 2014) gave a temporal dependence of the intensity of atomic Al lines and molecular AlO bands for a time period of

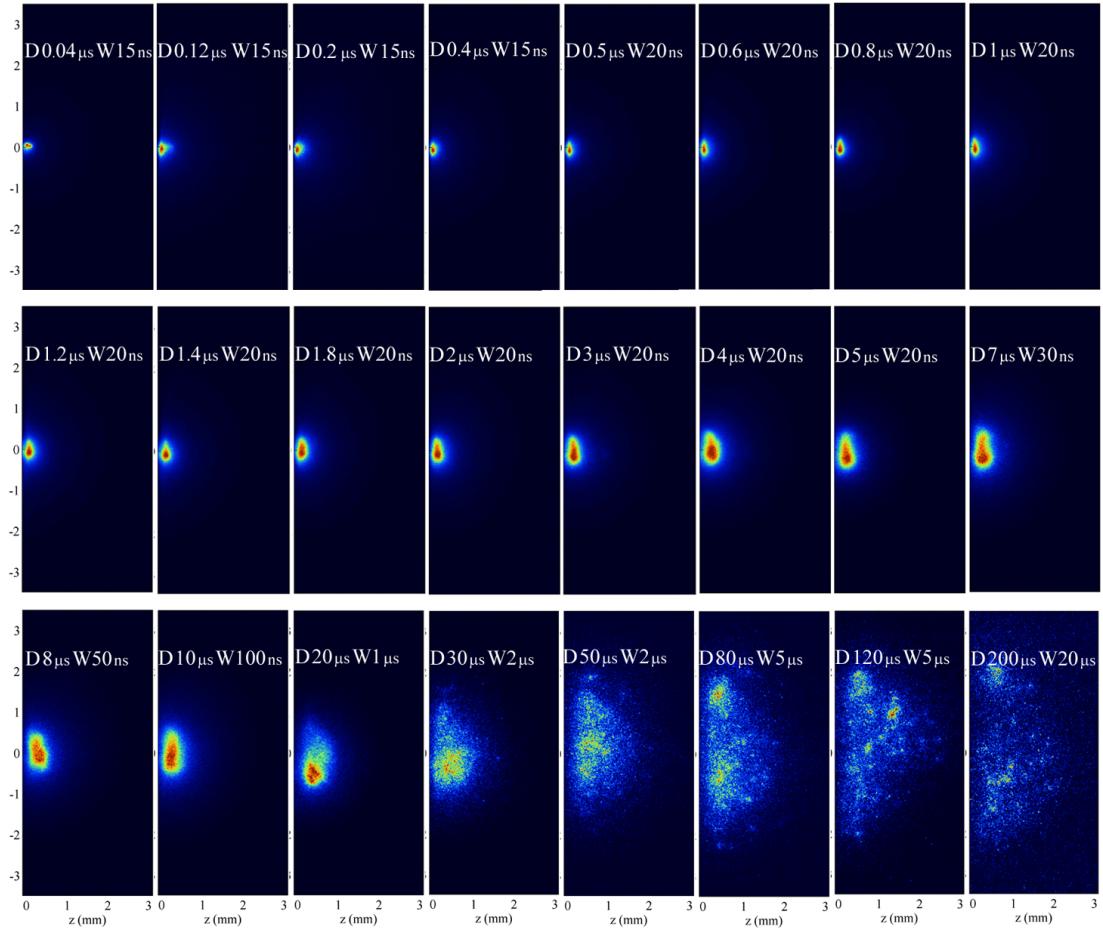


Figure 6.2: Fast photography of the plasma evolving from the target (placed on the left) captured at different delays D from the laser pulse with acquisition gate width W .

6 μs after the laser pulse. Although in ref. (Lam *et al.*, 2014) the plasma plume formation and shape were not imaged, the experimental data clearly demonstrate that some emission still exists after several microseconds from the laser pulse. In ref.(Oguchi *et al.*, 2007), a visible plasma emission was documented up to delays of 1000 ns and 2000 ns, for laser pulse durations of 20 ns and 100 ns, respectively. To date, a long lasting plasma emission after a SP laser excitation underwater was reported only by (Lazic *et al.*, 2013a) where the plasma plume was detected up to 30 μs from the laser pulse. Besides the long duration of emission similar two-stage plasma evolution is also reported in (Lazic *et al.*, 2013a), where plasma shape is changed from the spherical to flat at slightly longer delay of 1 μs . The first stage lasts approximately 1 μs and is characterized by the rapidly expanding plume and by ejection of macroscopic hot particles from the sample surface. In the second stage, the newly forming plasma expands slowly and smoothly from the target into the growing vapour bubble. This secondary plasma formation was explained by complex interaction of the hot plasma front with the surrounding, which leads to the propagation of a high temperature and high pressure region back to the target. Similar phenomena were reported for LA in air(Zhou *et al.*, 2011), (Tao *et al.*, 2012) where a newly formed emissive plume detected at 3 μs after the laser pulse was attributed to the expulsion of the material by the backward reheated and melted sample layer. Slow target evaporation through the backward reheated target into the growing bubble was recently explained in the context of material removal during LA in liquids.(Lazic and Jovićević, 2014). This particular phase of LA is not always observed and it depends on the experimental conditions.

Starting from the plasma photographs Fig. 6.2 for each acquisition delay the integral plasma intensity was calculated. The appearance of the graphical user interface (GUI) of the program used for this purpose is given in the Fig. 6.3. The first step is to import the experimental matrix, which is then displayed as an image in the lower part of the GUI. Afterwards, coordinates of the area over which the summation of the plasma intensity needs to be performed is defined in the section Define Rectangle and displayed over the plasma image as a white rectangle. The parameters of the rectangle can be changed interactively. In the same way, coordinates of the rectangle that represents background emission and noise that needs to be subtracted from the signal are then inputted and shown as the pink rectangle. Position of the background rectangle is chosen to be the furthest from

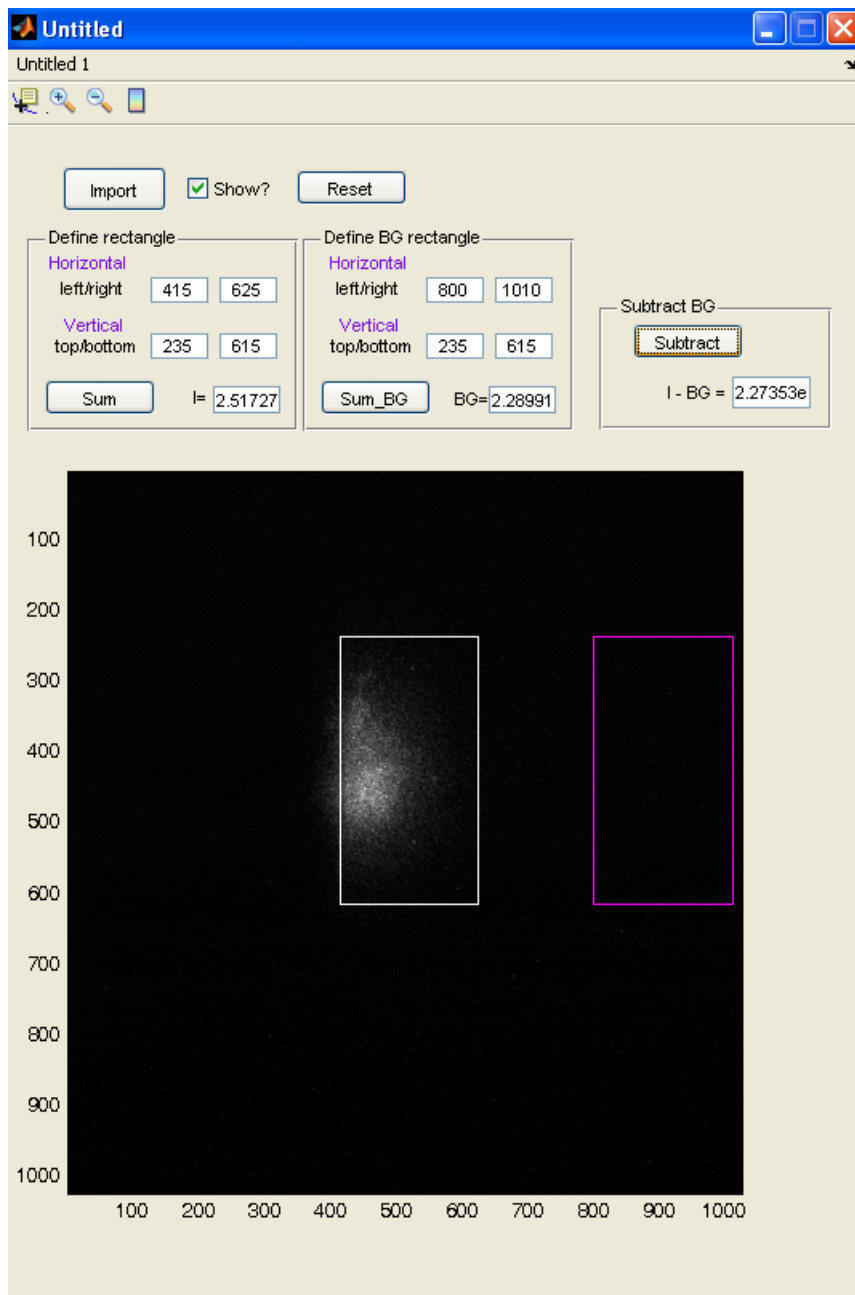


Figure 6.3: Graphical user interface for the calculations of the integral plasma intensity

the plasma emission and its size is the same as the rectangle for the summation of the plasma intensity. As a final step, subtraction of the background intensity from the plasma intensity is performed. This procedure was repeated for plasma images recorded at different delays.

In the next step, the obtained values were normalized on the gate width, the number of accumulations and on the nominal signal intensity as a function of the applied iCCD gain. The influence of the iCCD gain on the signal intensity was derived from measurements using an external light source. Example of the images used for calibration on iCCD gain is shown in the Fig. 6.4. All other acquisition parameters were kept constant, only the values of the gain were changing, taking care not to saturate the detector in the process and in this way the calibration curve for different applied gains was obtained. The normalized integral plasma intensity as a function of the acquisition delay for the pure Al target is shown in Fig.6.5.

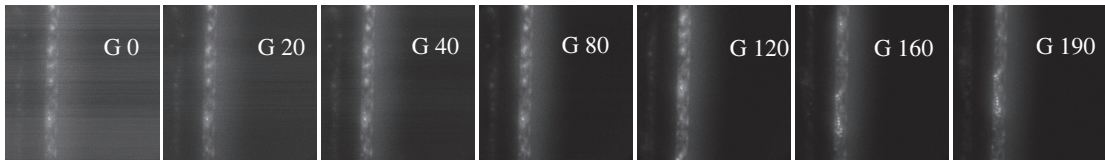


Figure 6.4: Sequence of the images recorded under the same experimental conditions only with varying applied gain used for the gain calibration

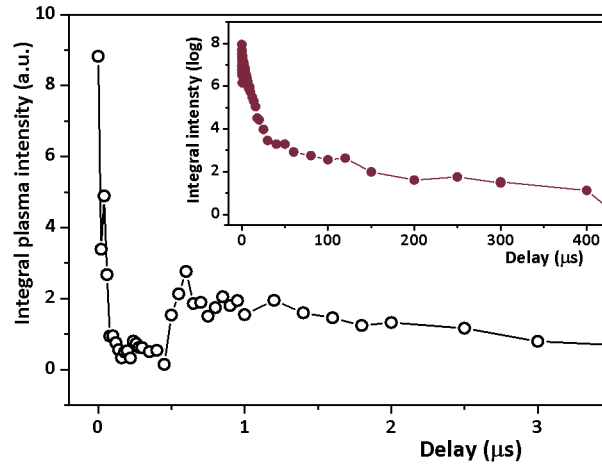


Figure 6.5: Temporal dependence of integral plasma intensity for early delays (main figure) and later delays (inset)

High intensity plasma emission immediately after the laser pulse is followed by rapid decrease of emission intensity in a few hundreds of nanoseconds as already reported in the literature (De Giacomo *et al.*, 2013). Temporal behaviour of integral plasma intensity up to delays of 500 ns is well described with the equation 6.1

$$I(t) = a_1 e^{-(t-t_0)/\tau_1} + a_2 e^{-(t-t_0)/\tau_2} \quad (6.1)$$

,often used to fit the temporal evolution of the continuum intensity (De Giacomo *et al.*, 2013)(Kennedy *et al.*, 1997) and is shown in the Fig.6.6

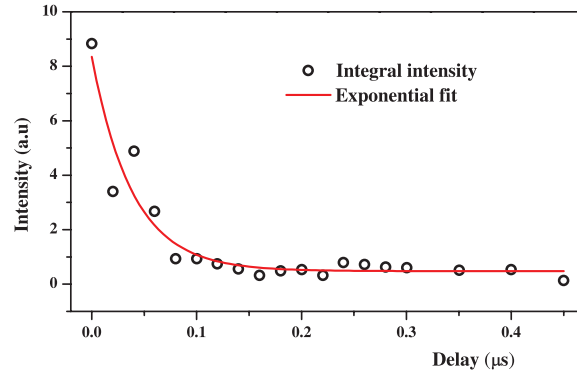


Figure 6.6: Early plasma emission intensity drop fitted with the exponential decay according to the eq. 6.1

After this initial fast decay, sudden increase in total intensity is observed at delay time of 500 ns . This phenomenon is ascribed to the coincident change in the plasma shape and size, which is at that point well localized on the target and with increased contact surface due to the flattening, thus producing more efficient heating and additional material evaporation. This heating remains effective as long as the plasma temperature is sufficiently high to produce target melting and evaporation. Looking at the inset of the fig. 6.5 it can be seen that some weak residual emission was detected up to delay of $\sim 475 \mu s$. This time interval, as it will be shown later, correspond to the time of the first bubble collapse.

In Fig. 6.7, the position of the maximum intensity plasma region above the target is shown as a function of time. After the initial fast forward movement of the most luminous plasma region (up to $250 \mu m$ from the target), the same moves back to the target after less than 100 ns. This is visible in the inset of Fig.6.7. Similar phenomena were previously observed in the laser ablation of targets in air.(Zhou *et al.*, 2011),(Tao *et al.*, 2012). Since the ablation in liquid environment has additional unique properties, other mechanisms driving this backward motion of the intense plasma emission towards the target (formation of the cavitation bubble, rebound of the internal shock wave, etc.) are also possible and additional investigations are needed.

In addition to the plasma flattening, the position of the most intense emission

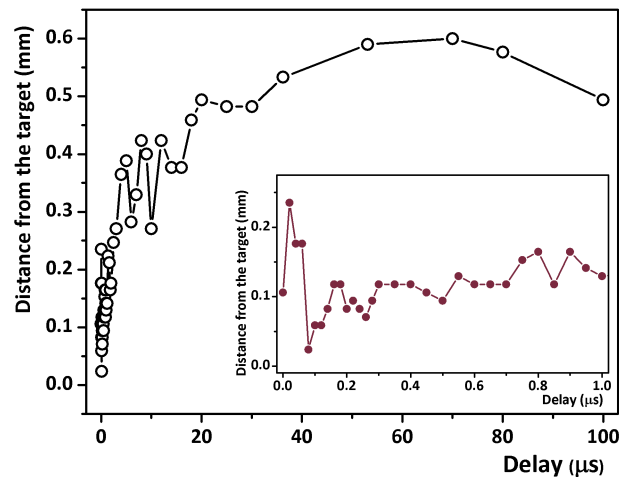


Figure 6.7: The position of the maximum intensity plasma region with respect to the target for later delays (main figure) and early delays (inset).

region remains almost constant for a few microseconds and it is situated up to 200 μm from the target, Fig.6.7.

Results presented in this Section show that high intensity, well localized and stable plasma over a few microseconds is formed which is advantageous for optical emission spectroscopy analysis of single pulse laser induced plasma (Gavrilović *et al.*, 2016), (Gavrilović *et al.*, 2017), since it enables the use of large number of accumulations and larger gate widths with respect to the initial, fast decaying emission. In contrast to this results, some papers (Oguchi *et al.*, 2007), (Matsumoto *et al.*, 2013a), (Matsumoto *et al.*, 2013b) reported the plasma images with a dark region immediately above the target. In this way, heating of the target with the plasma is less efficient, which can cause shorter (in the order of 100 ns) plasma persistence, as reported by authors. Throughout the course of these studies, very long lasting plasma emission ($> 100 \mu\text{s}$) was detected. Appearance and properties of this late emission coming from within the bubble will be discussed in the Sect.6.2.

6.2 Bubble dynamics

6.2.1 Plasma and bubble relations

As already mentioned in Sect.6.1, duration of the optical emission in these set of experiments on a single pulse laser ablation events is in the order of hundreds of μs . At this long time scales, cavitation bubble is formed and well expanded, leading to the completely different physical conditions inside which the plasma is evolving.

During the ablation of the pure Al target, some optically active species persist during the whole bubble cycle i.e. until its first collapse. Spatial relations between light emitting centres and vapour bubble was checked using superimposed images obtained by fast photography and shadowgraphy. Since the optical setup was the same for both imaging techniques, with addition of the WLS for the shadowgraphy, using dimensionally calibrated images precise position of the light emitting centres inside expanding bubble could be determined. From the Fig. 6.8, it seems that the unique temperature and pressure conditions inside confining vapour bubble favour the long lasting optical emission, since no emitting centers were observed outside the vapour bubble. Similar set of photographs for the ceramic alumina was also made and it is shown in the Fig.6.9. Also in this case, complete emission is coming from within the bubble, but dispersion of glowing points was not observed. These differences in appearance will be discussed in the Sect.6.5. Recent research about position and origin of nano particles (NPs) in underwater ablation claiming that all NPs are trapped inside the cavitation bubble (T.Tsuji *et al.*, 2007)(Wagener *et al.*, 2013)(Soliman *et al.*, 2010) seem to be supported by these findings, since all the emitting species are contained inside the bubble.

From the results presented here it can not be claimed that there are no particles outside the bubble but only the ones trapped inside still hold temperature high enough to emit some light. This surmise is further justified by temperature measurement with AIO molecular band up to delays of 10 μ s, that clearly shows that early bubble holds temperature as high as 3500 K in employed experimental conditions. (more about the temperature measurements can be found in the section 6.4). These temperatures agree with the values reported by (Casavola *et al.*, 2005) obtained by modeling of bubble dynamics.

6.2.2 Optical effects of the laser induced bubble

Furthermore, optical emitting region seems to never fill the entire bubble volume. Spatial relation of bubble and optically active area is illustrated graphically in the Fig. 6.10, where plasma radius normal and parallel to the target is expressed in percents of the corresponding bubble radius. Due to the bright plasma emission clear observation of the bubble and hence the bubble radius measurement, was not possible before $\sim 3 \mu$ s delay for the pure Al target. Radius of the plasma in direction normal to the target is 92% of the bubble radius at 3 μ s delay, falls down to the

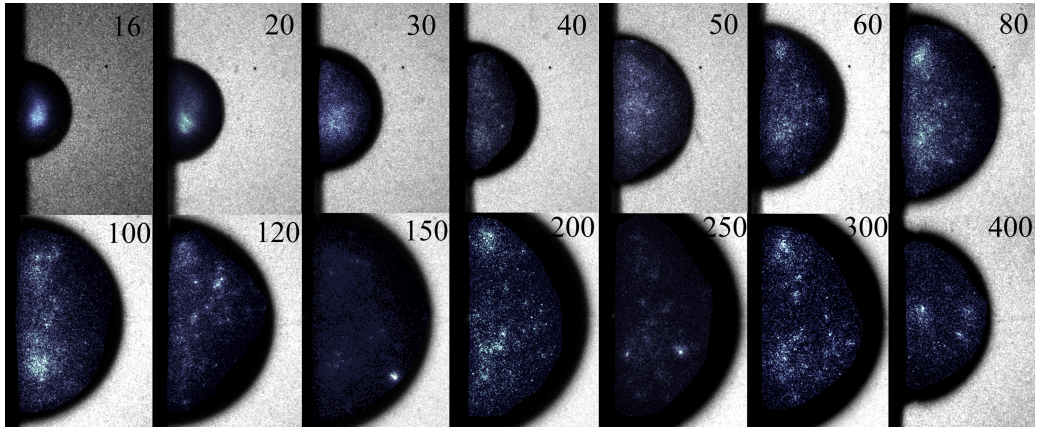


Figure 6.8: Superimposed images of plasma photography (false colour) and shadowgraphy for the pure Al target

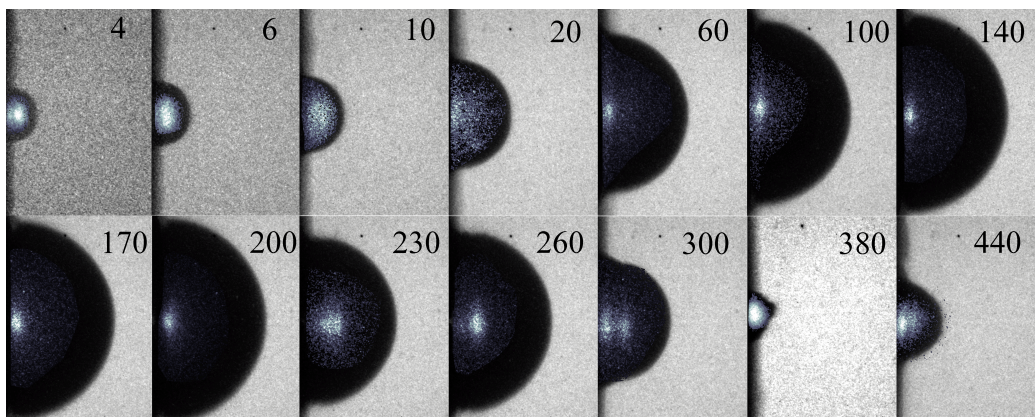


Figure 6.9: Superimposed images of plasma photography (false colour) and shadowgraphy for the alumina target

minimum of approximately 62% for delay of 20 μs , and afterwards starts enlarging again to approximately 70%. At the earlier delays of bubble expansion most of the glowing centres are located in proximity of the target. As the bubble grows and its internal pressure decreases these trapped particles start to expand more freely inside the bubble volume. Still, no optical emission was observed from the upper part of the bubble near the boundary with the liquid. The reason for this additional confinement to approximately 2/3 of the bubbles dimension can be just apparent reduction of the plasma size due to the optical properties of the bubble, which acts as a negative lens (Lazic *et al.*, 2012)(Lazic *et al.*, 2013a). Rays originating near the bubble edge and traveling parallel to the axis of the collecting lens are deviated strongly by expanded and cooled bubble so that they never reach the detector, creating the image of the emitting region with dark ring next to the bubble's wall.

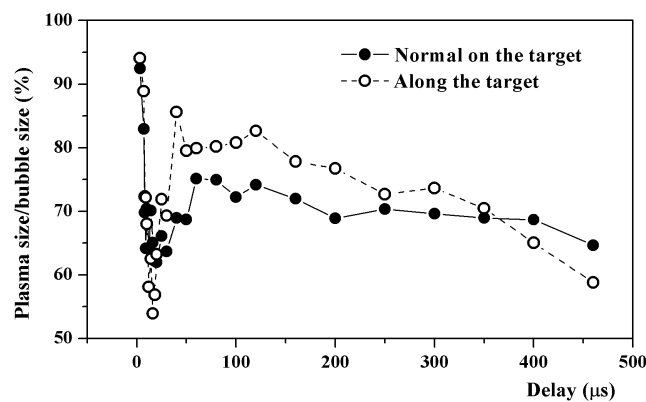


Figure 6.10: Percentage of the bubble volume occupied with the plasma for the pure Al target

Optical effect of the bubble are even more pronounced when observing the images obtained with shadowgraphy in the phases when the bubble is fully expanded. Imaging of the spherical bubbles and their effects on the light propagation have been studied widely in the literature, (Bongiovanni *et al.*, 1997)(Bongiovanni *et al.*, 2000)(Tiwari *et al.*, 2010). Different interaction orders of the bubble and the WLS used for the back lighting of the bubble are visible as high intensity points known as a glory (Langley and Marston, 1991) or glare points (Dehaeck and van Beeck, 2007). Glare circle and a bright spot formation due to the multiple reflections at the water-vapour interface during the imaging of the hemispherical and relatively cold gas bubble is shown in the Fig.6.11. Bright spot in the center is formed from the rays that have suffered $N=2$ interactions with the bubble wall, while the glare circle

the incoming ray can be written in the form

$$\frac{\cos(\tau_3)}{\cos(\tau'_3)} = \frac{n_{bub}}{n_{liq}} \quad (6.2)$$

while the dimension of the glory ring D_3 can be expressed as $D_3 = |AB| = R \cos \tau_3$. From the Fig.6.12 it can also be written $\tau_3 = 2\tau'_3$. Combining these two relations with the Eq.6.2 and after some mathematical manipulation, relation between the bubble diameter and the glory ring diameter can be obtained

$$D_3 = \frac{n_{bub}^2 + \sqrt{n_{bub}^4 + 8n_{liq}^2 n_{bub}^2}}{4n_{liq}^2} D_b \quad (6.3)$$

, where D_b represents the determined bubble radius. Introducing a new dimensionless parameter $\eta = D_3/D_b$ and solving the Eq.6.3 two expressions can be obtained, either to express the refractive index of the liquid or refractive index of the bubble as unknown variable. If constant and known refractive index of the liquid is assumed, and the dimensions of the bubble shadow D_B and glory ring D_3 are measured from the images, transient refractive index of the laser induced bubble can be calculated using the following equation

$$n_{bub} = \sqrt{\frac{2\eta^2}{\eta + 1}} n_{liq} \quad (6.4)$$

Using the Eq.6.4, the value of the refractive index of the bubble in the maximum expansion phase is unity, as previously obtained from the ray tracing models (Lazic *et al.*, 2012). The other measured values of refractive index in the time interval of 100 μs up to 450 μs are in the range 1 - 1.07, which also agree with the values obtained with the ray tracing in (Lazic *et al.*, 2012).

The important thing to notice here is that this method doesn't require any calibration, which is always advantageous. Although the accuracy of the method is not known (bubble is hemispherical, and initial assumption is spherical bubble) and it could only be applied for relatively late delays when the bubble is sufficiently expanded, it provides experimental evidence of refractive index change. The precision of the measurement is mainly determined by the accuracy of the bubble size determination since the glare circle has much sharper defined edges. Bubble sizing methods are described in the 6.2.3.

6.2.3 Bubble sizing

The procedure for determining the bubble size from dimensionally calibrated images was written in the Matlab[®] and the main steps are illustrated in the Fig.6.13

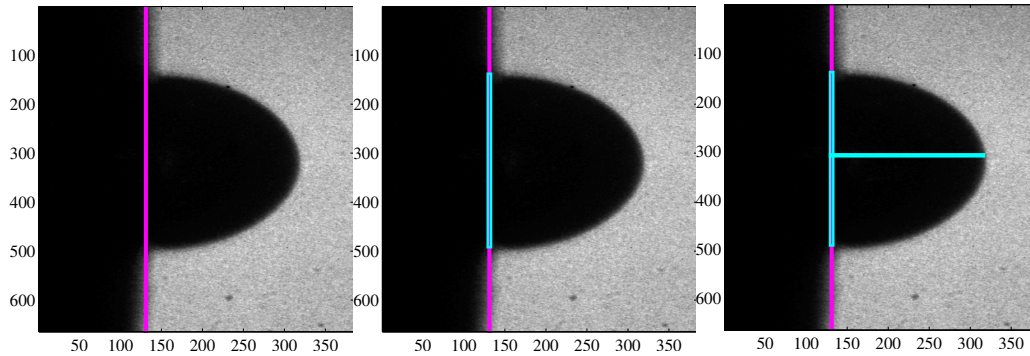


Figure 6.13: Steps in determining bubble size: Target position, bubble size along the target, bubble size normal on the target, from left to right

The first step in determining the bubble size is to determine the position of the target surface. This position (and the bubble edge also) is defined at 50% of the difference between the maximum and the minimum intensity values along the horizontal direction in the image 6.13. This way of the edge determination was defined since the intensity falls from the maximum or "white" to the minimum or "black" over considerable amount of pixels (>10). Although the edge is located somewhere among these gray pixels, it is impossible to obtain any more precise information, as pointed out in (Bongiovanni *et al.*, 1997) where it was concluded that the intensity level at the mathematical bubble edge depends on the illumination source, the location and the size of the bubble. Once the position of the target is determined and displayed as magenta line, the bubble size is determined and marked with the cyan line, see Fig.6.13, middle figure- size along the target, and right figure- size normal to the target. This procedure for the bubble size determination works well also in the cases when the bubble has less regular shape, which happens very often during the collapse phases of the bubble. Extraction of the bubble size from the images where the shape of the bubble is deformed is illustrated in the Fig. 6.14.

The procedure for the bubble sizing is coded in the way that it imports all the experimental files with the extension .sif from the chosen folder, determines both bubble sizes and displays them in the separate figures. For each imported file, the procedure extracts from the name of the file the delay at which the bubble was recorded and stores that information with the corresponding values of the bubble size along and normal on the target. As a final step, based on the inputted value

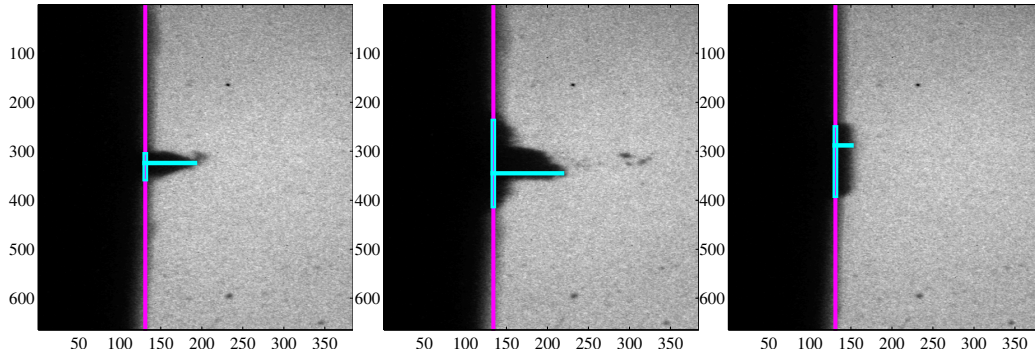


Figure 6.14: Size determination for bubbles with irregular shapes

of the spatial dispersion in mm/px graph of temporal evolution of the bubble size is displayed, see Fig.6.15 where the outcome of the procedure is illustrated on the example of the pure Al target in the final experimental configuration (see Sect.5).

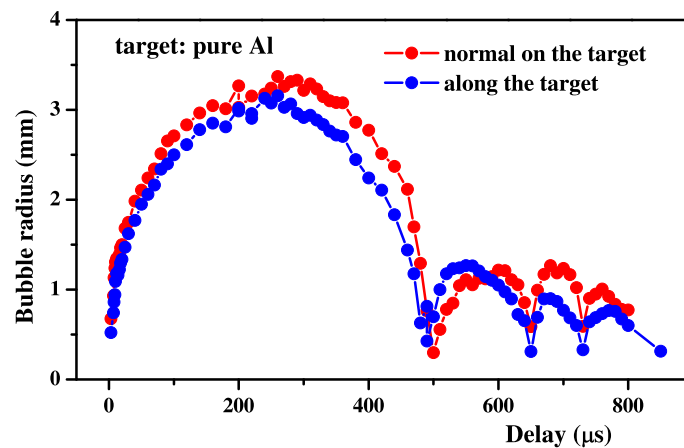


Figure 6.15: Output of the procedure for the bubble sizing

From the Fig.6.15 it is found that the maximum bubble expansion occurs 260 μ s after the laser pulse, and its radius is ~ 3.157 mm and ~ 3.371 mm in the direction parallel and normal to the target surface, respectively. The bubble remains slightly elongated towards the laser source during the expansion. Differently, in the shrinking phase a part of the bubble just above the target starts to deform, increasing the contact angle, as evident in Fig.6.8 at a delay of 400 μ s. Similar phenomena were also observed by (Ibrahimkuty *et al.*, 2015) who speculated that still high surface temperature can be responsible for the observed change in the contact angle between vapour, liquids and solids.

In this experimental setup on the pure aluminium, the bubble collapses after about 475 μ s from the laser pulse, evidenced by the release of the second shock wave

in Schlieren images, see Sect.6.3. Based on the experimentally determined radius and time of the bubble's collapse, the energy contained in the bubble was estimated using formula 6.5 widely used in the literature (Sasaki *et al.*, 2009) (Cristoforetti *et al.*, 2012) and adapted to the cases of hemispherical cavity produced by laser ablation in liquid (Soliman *et al.*, 2010) (Sasaki *et al.*, 2009). The difference between static pressure in liquid and pressure of the vapour inside the bubble ($p_{stat} - p_v$) is inferred using Eq.6.6

$$E_b = V(p_{stat} - p_v) \quad (6.5)$$

$$T_b = 2 \cdot 0.915 \cdot R_{max} \sqrt{\frac{\rho}{p_{stat} - p_v}} \quad (6.6)$$

where T_b represents the bubble oscillation period (Thornton *et al.*, 2013) (Franc and Michel, 2004), i.e. time elapsed between bubble formation and the collapse so if the bubble evolution is symmetric in time, bubble oscillation period is double *Rayleigh* collapse time derived in Sect.3.2.2, eq.3.23. Eq.6.6 was derived for spherical bubbles but has already been proven to be applicable for elongated bubbles (Thornton *et al.*, 2013) as is the case here. R_{max} for elongated bubbles corresponds to the radius of a sphere which has the same volume as the elongated bubble. (Sasaki *et al.*, 2009) In this way the energy stored in the bubble was calculated to be 10.8 mJ. Three bubble rebounds were detected after the initial collapse, which lasted up to 900 μs after the laser pulse. During the successive rebounds the bubble had less regular shape and it was flattened on the target.

From the results presented in this Section, it is evident that the large part of the input laser energy is spent on the bubble formation.

6.2.4 Probe techniques for investigation of the bubble's dynamic

The imaging techniques with the iCCD camera, despite its numerous advantages, especially in the temporal and spatial resolution, suffer also from some drawbacks. The main is that the temporal evolution of the bubble (or plasma or shock wave) can not be recorded from the one laser shot. Laser probe techniques have been used for a long time to obtain closer insight into processes of laser ablation (Koren, 1987) (Sell *et al.*, 1989) (Diaci and Možina, 1995) since they enable one to follow

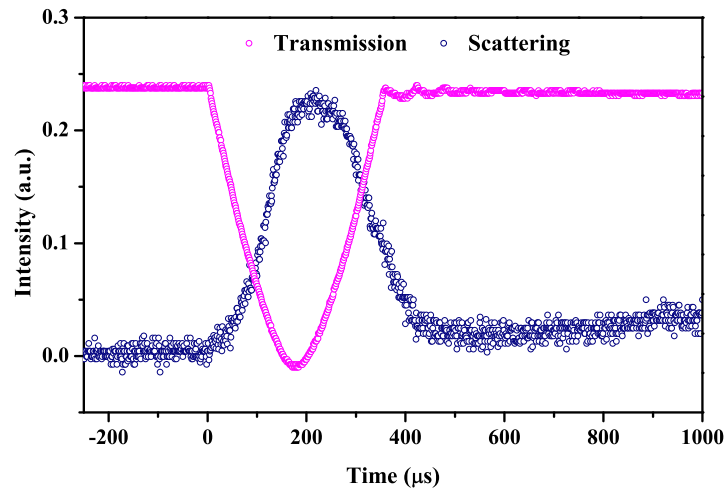


Figure 6.16: Probe beam techniques on alumina sample, blue circles scattering, magenta circles transmission

the temporal evolution of the processes from one laser pulse. Having this in mind, besides imaging the bubble, two additional probe beam techniques were applied for studying the bubble, and example of the result is shown in the Fig.6.7.

The technique (transmission) was recently applied in (Matsumoto *et al.*, 2016) to study the difference in bubble oscillations between laser ablation with long and short nanosecond laser pulses, and it was called the laser-beam transmission probe (LBTP). The same technique under the name beam deflection was used in the (Nath and Khare, 2008) for studying the velocities of the charged particles and the bubble wall. Slightly different setup called again beam deflection technique was used in (Chen *et al.*, 2004) for investigation of the shock wave and cavitation bubble oscillation. Very good agreement between the various probe and imaging techniques was proved in several publications (Petkovšek and Gregorčič, 2007)(Gregorčič *et al.*, 2007) (Gregorčič *et al.*, 2008)(Nath and Khare, 2011)(Gregorčič *et al.*, 2016)(Chen *et al.*, 2017) giving the higher credibility to the probe beam techniques. Recently, dependence of the transmission signal on the bubble radius was derived in the case when the transmission signal was additionally blocked by an aperture in front of the fast photodiode used for the signal detection(Koch *et al.*, 2012)

The first thing to notice is that the two probe beam techniques applied here show very good agreement in times of the bubble expansion and shrinking phases. The transmission technique has slight advantage in signal strength and hence higher

order bubble oscillations could be captured with it, as illustrated on the example of the pure aluminium target 6.17, while with the scattering technique whose signal is significantly lower, only the first bubble rebound could be seen in pure Al6.18. In the case of alumina where successive rebound bubbles have very short duration and small sizes, no successive rebounds were detected with the scattering method6.16. Higher sensitivity of the transmission can also be seen in the interval when complete period of bubble oscillation is over. Namely, as reported in (Matsumoto *et al.*, 2016), the transmission signal level after the bubble oscillation has finished doesn't recover completely to its initial value. The reason for this lowering of the "undisturbed" transmission signal intensity can be the presence of the material that was trapped inside the bubble. After the bubble oscillation period ends, material is expelled in the liquid and stays preferentially in the proximity of the target blocking the part of the probe beam and thus causing the intensity of the transmitted signal to be lower, see Fig.6.17. This effect is less pronounced for ceramic alumina target and it is related to material's characteristics which will be addressed in the chap.6.5.

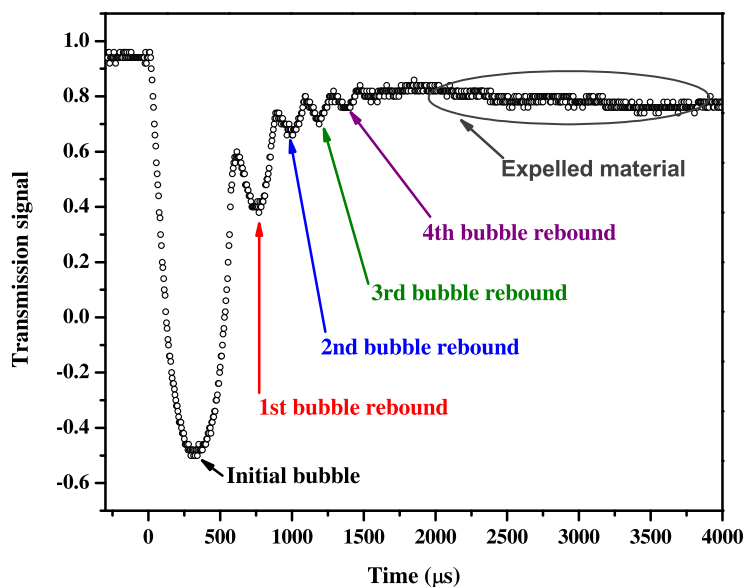


Figure 6.17: Complete bubble evolution from one laser pulse recorded with transmission technique - four bubble rebounds detected. Decrease in the signal after the extinction of the bubble is attributed to the material expelled in the liquid.

Since the transmission technique is quite simple and gives complete evolution of the bubble in time, the question remains whether this changing signal intensity can

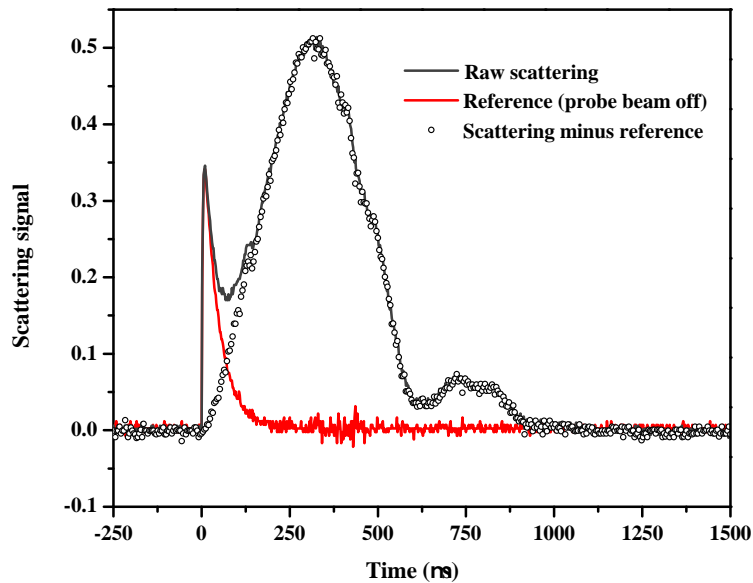


Figure 6.18: Complete bubble evolution from one laser pulse recorded with scattering technique-only the first bubble rebound detected.

somehow be linked the to time evolution of the bubble radius. The procedure applied for that cause is similar to the one described in (Chen *et al.*, 2017) ,(Chen *et al.*, 2004) and (Lazic *et al.*, 2013b) and it is based on the change of the distance between the probe beam and the target. Besides changing the distance, the probe beam was additionally restricted with the rectangular slit to $100 \mu\text{m}$ width, in order to probe the different heights above the target. The concept of the technique is to determine the distance from the target, at which the characteristic dip in the transmission signal due to the interception of the probe beam by the growing vapour bubble, disappears. The typical result is shown in the Fig.6.19 for the case of the ceramic alumina target. None of the transmission signals detected with the slit showed clear bubble rebounds, possibly due to the significantly lower intensity of the probe beam, whose size is reduced from the $\sim 5 \text{ mm}$ to only $100 \mu\text{m}$. The relative change in transmission signal intensity is not the same for all investigated distances.

Namely, for the closest examined distance above the target $d=0.2 \text{ mm}$, the detected decrease in the signal intensity due to the appearance of the bubble is relatively small, light green curve in the main Fig.6.19. As the distance of the probe beam above the target increases, the relative change of the signal intensity enlarges and reaches its maximum change (minimum in the transmission signal) for the dis-

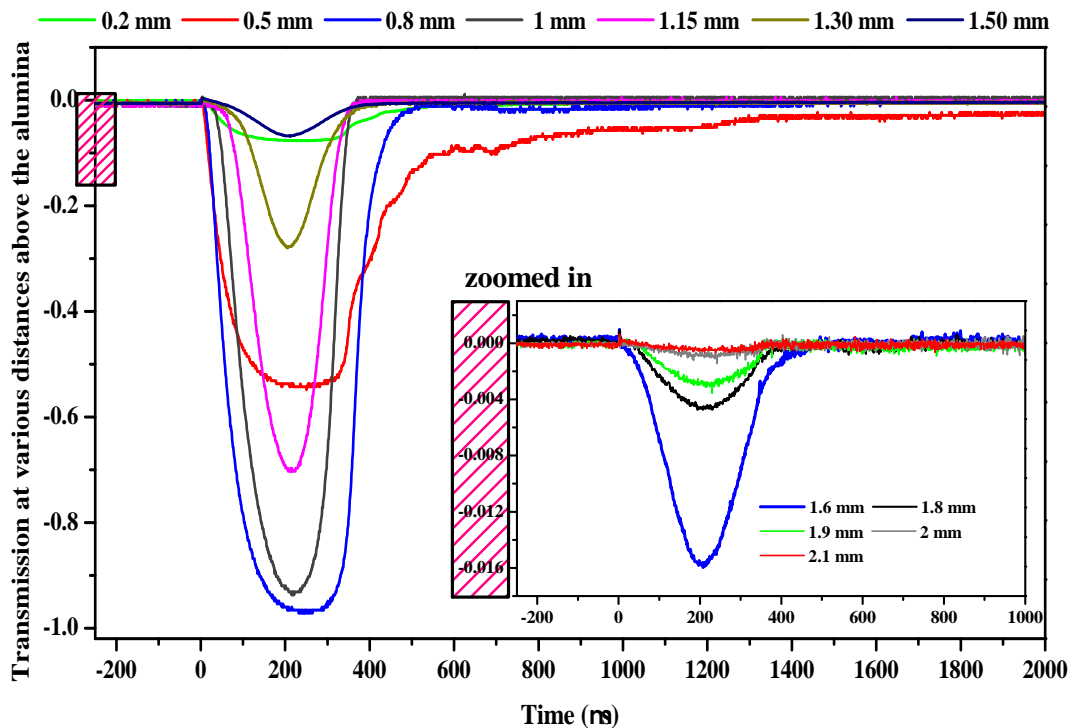


Figure 6.19: Transmission signal on alumina target for different positions above the target surface. Inset figure shows signal for distances from the target which are close to the bubble radius value

tance $d=0.8$ mm from the target surface, blue curve in the main Fig.6.19. Further increase of the distance results in shallower dips, with decreasing durations. The longest duration of the signal perturbation is detected at the distances closest to the target, which is explained through the joined effects of the bubble and ejected material in proximity of the target surface and on the probe beam transmission. This, at the first glance unusual, increase of the transmission dip with departure from the target might be explained by analysing the propagation of the characteristic rays through the expanded bubble, with the refractive index ~ 1 . Three representative beam positions are depicted in the Fig.6.20. The rays traveling very close to the target surface encounter the bubble surface under very small angles θ_1 , thus experiencing the least deviation from their original path. With increase in distance, the angle of interaction increases, leading to the complete deviation of the incoming beam which cannot reach the detector. Further increase, on the contrary, enhances optical effects of the bubble, already mentioned in the Sect.6.2.2 and causes more rays to be able to reach the detector after multiple interaction with the bubble wall. In the inset of the Fig.6.19 the signals at the furthest distances of the probe beam

from the target are zoomed in. The last signal with observable dip corresponds to the separation of the probe beam and the target of ~ 2.2 mm, leading to the conclusion that the bubble diameter is at least 2.2 mm. This value is just the lower limit for the maximum bubble radius determined using transmission, since the beam at distances from the target comparable to the bubble size, is partially transmitted directly to the detector without interaction with the bubble, masking the weak intensity transmission dip. From the dimensionally calibrated images of the bubble on alumina in the same experimental conditions, maximum bubble radius is determined to be 2.3 mm, which means that this form of the transmission technique can be used for bubble sizing with uncertainty better than 20%.

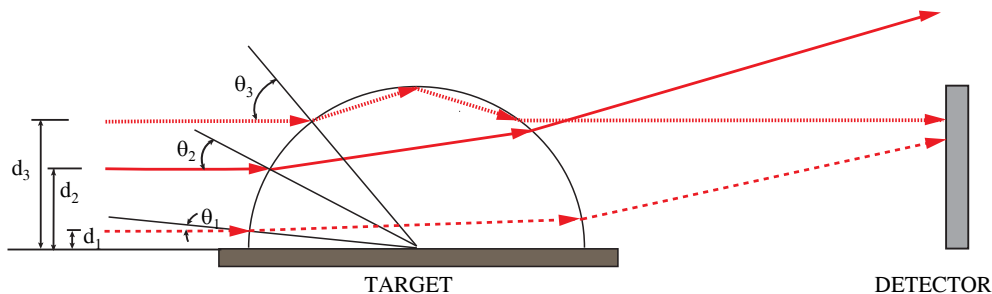


Figure 6.20: Explanation of the transmission with the slit

The second probe beam technique, scattering is less sensitive and slightly more difficult for alignment compared to the previously described transmission technique. It was previously shown how to measure maximum bubble radius with the transmission technique. Scattering signal with subtracted background, on the other hand, can give insight in complete evolution of the bubble size if independent calibration is provided (Lentz *et al.*, 1995). Typical shape of the scattering signal is shown in the Fig.6.7 together with the corresponding transmission signal on alumina target, while in the Fig.6.18 the measured scattered signal for the pure Al target is shown. The focusing conditions and chamber dimensions were different for the two targets, but since there will be no comparison between the two targets, this fact is for now irrelevant.

In the Fig.6.18 raw scattered signal exhibits an additional peak corresponding to the plasma emission. Although the scattered radiation was recorded with the interference filter, the plasma radiation still has very high intensity, in some cases even stronger than the useful scattered signal. To observe just the pure scattered signal, the signal from the plasma radiation in the absence of the probe beam was

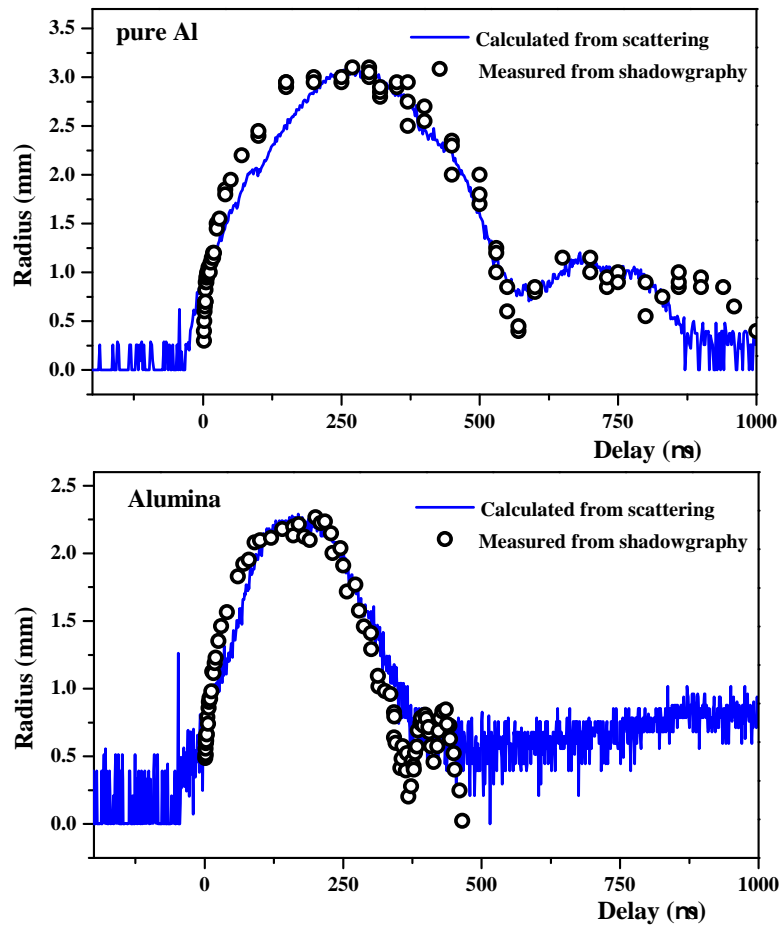


Figure 6.21: Comparison of the calibrated scattered signal based on the maximum bubble radius determined from the shadowgraphy measurements and bubble radius evolution determined from shadowgraphy

recorded (red curve in the Fig. 6.18) and then subtracted from the recorded scattered signal. This procedure was applied for every target and all experimental conditions. As discussed in sec.3.2.4, the underlying physics of scattering technique is Mie's scattering. But, in our experimental conditions, the bubble has dimension in the mm range and the condition $r/\lambda \gg 1$ is fulfilled, where r is the bubble radius and λ is the wavelength of the probe beam light. In such cases, much simpler geometrical optics approximation can be used to describe the scattering from the bubble. Both Mie and geometrical optics approximation correlate the scattered light intensity with the squared value of the bubble radius, irrespective of the observation angle. In this way, recorded signal, which is actually photomultiplier voltage, can be expressed as a function of the bubble radius:

$$R(t) \propto T(t) = [V(R=0) - V(t)]^{(1/2)} \quad (6.7)$$

where $V(t)$ is the PMT voltage and $V(R=0)$ is the background scatter detected when there is no bubble present (Barber and Putterman, 1992). The only missing thing is the constant of proportionality, which can be obtained through some sort of the independent calibration for (at least) one point. The independent calibration applied here was the fast shadowgraphy technique. The choice was to calibrate at the point of the maximum scattered signal (highest signal to noise ratio, SNR) and to relate that value to the maximum bubble radius obtained from the shadowgraphy. In this way calibration constant is determined, and used to retrieve the complete evolution of the bubble radius from the scattered signal intensity. The results of this procedure on the example of the pure aluminium and alumina target are shown in the Fig.6.21. The agreement is quite good for the first bubble, while higher order bubble oscillations couldn't be reproduced. The other possibility for an independent calibration is the maximum bubble size determined from the transmission measurements with the slit.

To conclude, although the accuracy of the bubble sizing with the probe beam techniques is lower compared to the fast shadowgraphy, this combination also offers several advantages: i) There is no need to use an iCCD camera, which significantly reduces the cost of the equipment ii) the alignment procedure is much simpler, especially for the transmission iii) complete evolution can be obtained in just several laser shots (one shot to record the scattered signal and a few to scan the different heights above the target and determine the maximum bubble size with transmission).

6.3 Shock wave propagation

Besides the bubble, other important mechanical effect in LA underwater is the shock wave (SW) which emerges, as a result of the disturbance induced by the pressure developed during plasma formation (Delale (Ed.), 2013), Fig.6.22 Based on the measured position of the outer shock wave front, on the pure Al target, initial velocity of the shock wave is estimated to be 3 km/s at 100 ns delay but drops down very quickly to 1.6 km/s after 1 μ s. Based on the determined shock wave velocity, the peak pressure as a function of a shock wave velocity can be obtained using the equation 3.6 in Chap.3 (Delale (Ed.), 2013) (Kennedy *et al.*, 1997).

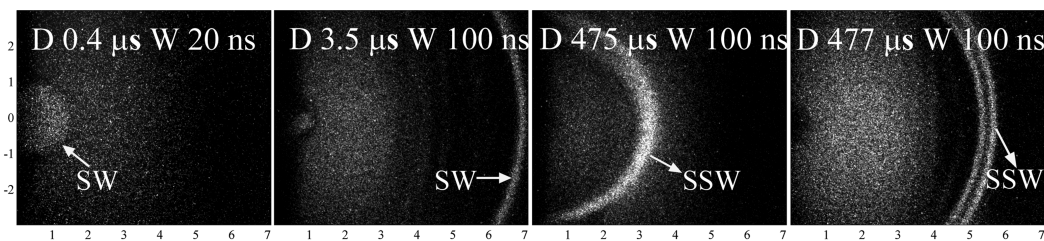


Figure 6.22: Images of the shock wave on pure Al obtained using the Schlieren technique, at different delays D from the laser pulse; W is the acquisition gate width.

Derived values of pressure are 2.29 GPa at the earlier delays and 86 MPa after the 1 μ s, similar to those reported in the literature (T.Tsuji *et al.*, 2007). The velocity of the second shock wave could not be determined with employed measurement procedure due to the slight fluctuations in the time of the bubble collapse and subsequent release of the second shock wave ($\pm 2 \mu$ s). Second collapse did not produce observable shock wave. Determination of the energy consumed by the shock wave was not possible since the largest part of the shock wave energy is deposited in the vicinity of the target where and in very early stages of the LIB in which the measurement of the shock wave front propagation was not possible due to very bright plasma emission.

Based on the calculated velocities and pressures and having in mind the work of (Vogel *et al.*, 1999) it can be stated that a large part of the input laser energy is spent on the shock wave.

6.4 Optical emission spectroscopy results

Optical emission spectra recorded from the laser induced plasma inside liquid environment has several particular characteristics, which make it very different from the

one in the gaseous surrounding. Since in the employed experimental setup plasma evolves in the two phases, primary and secondary, described in the Sect.6.1 spectrally resolved emission also differs significantly between the two phases. The typical behaviour of the emission signal in the both phases will be described on the example of the metallic aluminium and ceramic alumina target.

6.4.1 Primary plasma phase

Spectral characteristics of the plasma immediately after the laser pulse impacts the target are very similar to the ones usually reported from underwater plasmas. The one that makes the plasma diagnostic from this spectra extremely difficult and is the most pronounced is the intense continuum emission. Number of papers exist where the continuum radiation was the only spectral feature that could be recorded (Suzuki *et al.*, 2002)(Ushida *et al.*, 2007). Spectral line emission superimposed on strong continuum emission is illustrated on the example of the spectra from alumina target, recorded at a delay of 500 ns shown in the Fig. 6.23.

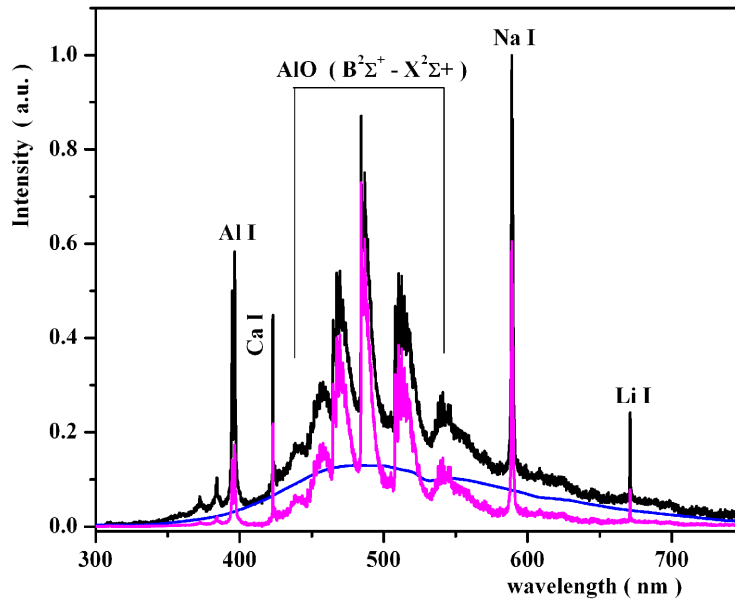


Figure 6.23: Typical spectra acquired after LIB on alumina. Blue curve represents continuum contribution which has been subtracted from experimental spectrum (black curve) and result (magenta curve) is marked as corrected spectrum.

The raw recorded spectra is displayed as a black line, while the spectra after the subtraction of the continuum component (the blue curve) is shown as a magenta line. For the case of the pure Al target, the continuum contribution is even more

pronounced, especially at the early delays of the 0.1 μs which is the earliest delay at which the spectroscopic measurements were performed. The temporal evolution of the spectra on the pure Al target is shown in the Fig.6.24, demonstrating difficulties that one encounters when performing spectroscopic measurements at delay times $\leq 1 \mu\text{s}$, as usually done in the literature. It can be seen in both cases that emission below 350 nm is very low, partially due to the strong absorption by water in that wavelength range.

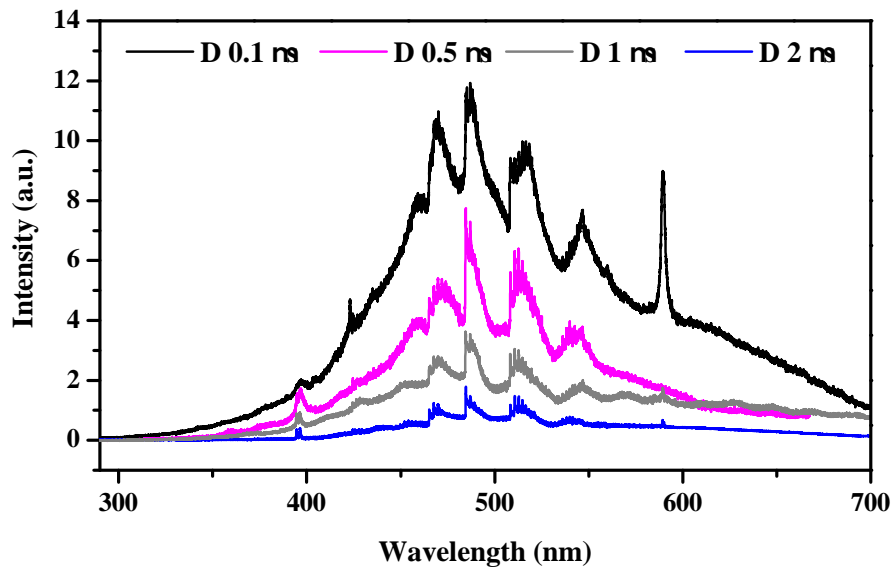


Figure 6.24: Strong continuum radiation in the spectrum of the pure Al target recorded at delays of 0.1, 0.5, 1 and 2 μs after the laser pulse

Procedure for evaluation and subtraction of the background from the recorded spectra was written in the Matlab[®] according to the procedure described in the (Rekhi *et al.*, 2003). Graphical user interface of the program for the continuum component evaluation and subtraction is shown in the Fig.6.25. Besides the need to remove the continuum component that might interfere with the line emission, the continuum itself is recognized as valuable tool for diagnostics of laser induced plasma (De Giacomo *et al.*, 2010). In underwater laser plasmas the value of informations extracted from the continuum increases due to the lack of ionic emission lines and a few atomic emission lines, as can be seen in the Figs.6.23-6.24.

The program illustrated in the Fig.6.25 works as follows. Pressing the buttons 'Import data' and 'Import CF' opens the dialog where the user can navigate to the requested file. If the 'show' check boxes are on the inputted spectra is displayed in the main window and calibration curve in the separate figure. Then the user inputs

in the field 'temperature' estimated value of the temperature for which the continuum component should be created. The next three buttons 'Planck', 'Emissivity' and 'Int.Corr' create the Planckian curve for the inputed temperature value in the spectral range determined by the experimental spectrum, correct it for the emissivity of the "grey" body and for the spectral response of the optical system used for the recording of the spectra. All of the steps can be displayed in the main window of the GUI, as desired. Since all the curves and the experimental spectrum are normalized to unity, it is necessary to scale the resultant 'Int.Cor.' curve to compare it with the spectrum, which is achieved by entering the scaling factor in the box 'scale'. This curve is shown in the example of the GUI in 6.25. The process can be repeated until the satisfactory agreement is obtained. Based on the wavelength for which the generated curve reaches its maximum value the temperature is evaluated using the Wien's displacement law, eq.6.8

$$\lambda = \frac{2.8977682 \cdot 10^6 [\text{nmK}]}{T} \quad (6.8)$$

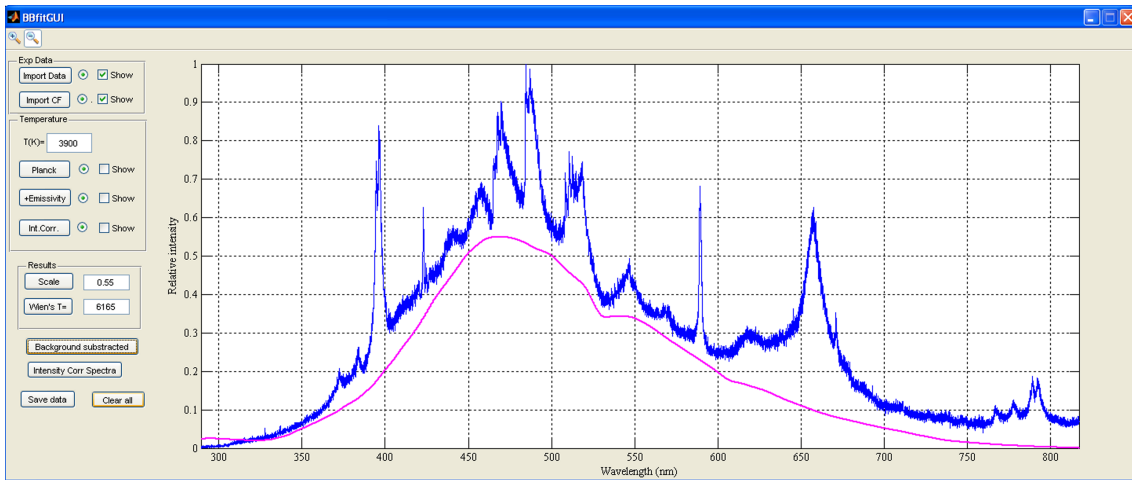


Figure 6.25: Graphical user interface of the program for determination and subtraction of the continuum component from the recorded spectra and temperature evaluation based on the Planck's law

When the correct curve is determined it can be subtracted from the original spectra by pressing the button 'Background subtracted' and corrected for the calibration function of the system ('Intensity CorrSpectra'). 'Save data' option saves altogether the experimental data, continuum curve, corrected spectra and determined value of the temperature from the Wien's law.

The usual values of the electron temperature obtained by fitting the continuum

component with the Planck's law are in the range 6000-7000K. This temperature represent just an estimate averaged over the gate width of 0.5μ . Still, at the earliest delays after the laser pulse for which the spectra were recorded, 0.1μ s, this is the only temperature information that could be obtained, since no well resolved line profile was recorded at that delay for any of the investigated materials. The example of the line emission quality at early delays is shown in Fig. 6.26.

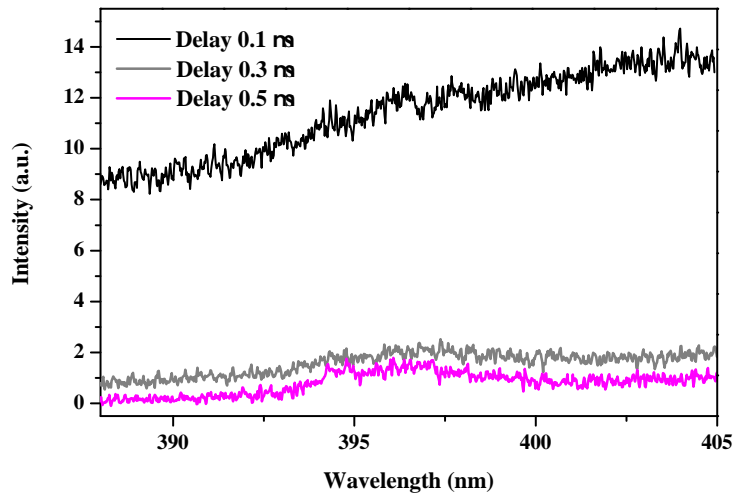


Figure 6.26: Absence of line emission in primary plasma phase on aluminium and slow emerging of the line at delay of 0.5μ s when the continuum intensity drops significantly

The line emission that was present only in the primary plasma phase is emission from the hydrogen H_{α} line on both the pure Al and ceramic alumina, and oxygen triplet $2s^22p^3(^4S^0)3s-2s^22p^3(^4S^0)3p(^5S^0-5P)$ on alumina. Profiles of the H_{α} and oxygen triplet were reported in the electrical discharge machining plasmas (Descoeurdes *et al.*, 2008) (Descoeurdes *et al.*, 2005)(Descoeurdes, 2006) and laser induced plasmas at a water/gas interface(Adamson *et al.*, 2007)(Lo and Cheung, 2002) but these line emissions are seldom observed in the plasmas produced by the laser in the liquid environment. Few examples to the contrary are (Escarguel, Ferhat, Lesage and Richou, 2000) for laser induced plasma in the pure liquid and (Kumar and Thareja, 2010) for the laser induced breakdown on the submerged aluminium target. Although, at the first glance, that might seem odd, few explanations for this rare appearance of hydrogen and oxygen emissions exist. Namely, temperatures of the laser produced underwater plasmas are relatively low (several thousands of K (Kennedy *et al.*, 1997)) due to the higher thermal dissipation capacities of liquids

compared to the gases (Lam, 2015). As a consequence, ionic lines and lines with the higher excited state energies are not frequently observed. Large energy spent in the shock wave emission and Bremsstrahlung emission additionally cools the plasma, which increases the rate of the electron-ion recombination (De Giacomo *et al.*, 2007) making the emission from the higher excited states less possible.

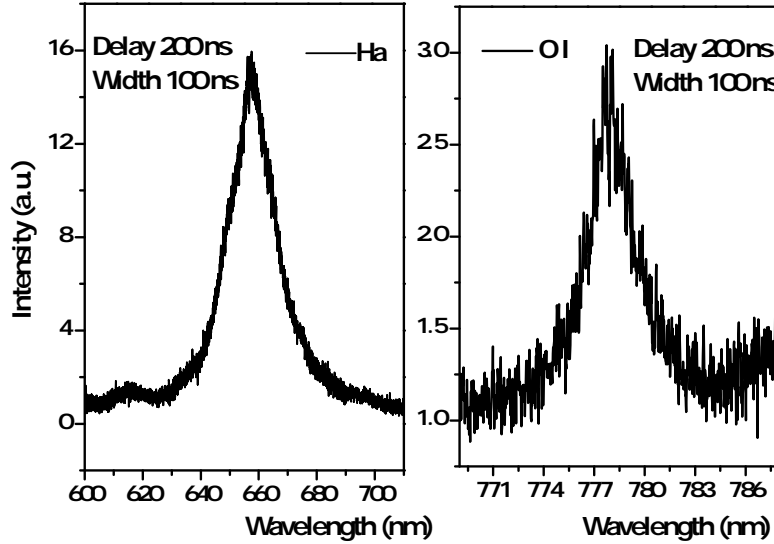


Figure 6.27: Profiles of the H_{α} and oxygen I line recorded in the first plasma phase on the alumina target

Examples of the hydrogen and oxygen line profiles at delay $0.2 \mu s$ for ceramic alumina are shown in Fig.6.27. On the metallic aluminium target the H_{α} line was recorded only at delay of $0.1 \mu s$, while for the ceramic alumina it was detected up to $0.8 \mu s$. Oxygen emission is extinguished rapidly (visible up to $0.4 \mu s$) not only due to the high excitation level of the transition, but also due to an intense oxidation of the target species, as visible from AlO emission appearing already 100 ns after the laser pulse.

H_{α} line was used for the evaluation of the electron number density, since the higher member of the series, which would be more reliable, were not detected in the spectrum. This method of the electron number density determination is convenient since it does not require knowledge of the plasma temperature. The width of the line is extremely large, going up to 26 nm for the pure Al target at a delay of $0.1 \mu s$. Using the equation for electron number density diagnostics from the (Konjević *et al.*, 2012)

$$N_e[\text{m}^{-3}] = 10^{23} * \left(\frac{w_{SA}[\text{nm}]}{1.098} \right)^{1.47135} \quad (6.9)$$

electron number densities in the range $(0.6-7.7) \cdot 10^{18} \text{cm}^{-3}$ for ceramic alumina were obtained. The spectral profiles were fitted with the Voigt function, and Lorentz width was used in the eq.6.9. Gaussian part was kept fixed and it was set to determined value of instrumental profile of 0.105 nm, which was negligible compared to extremely large widths of the profile. Typical fit of the H_α line and derived temporal evolution of the electron number density on the plasma from alumina is shown in the Fig.6.28

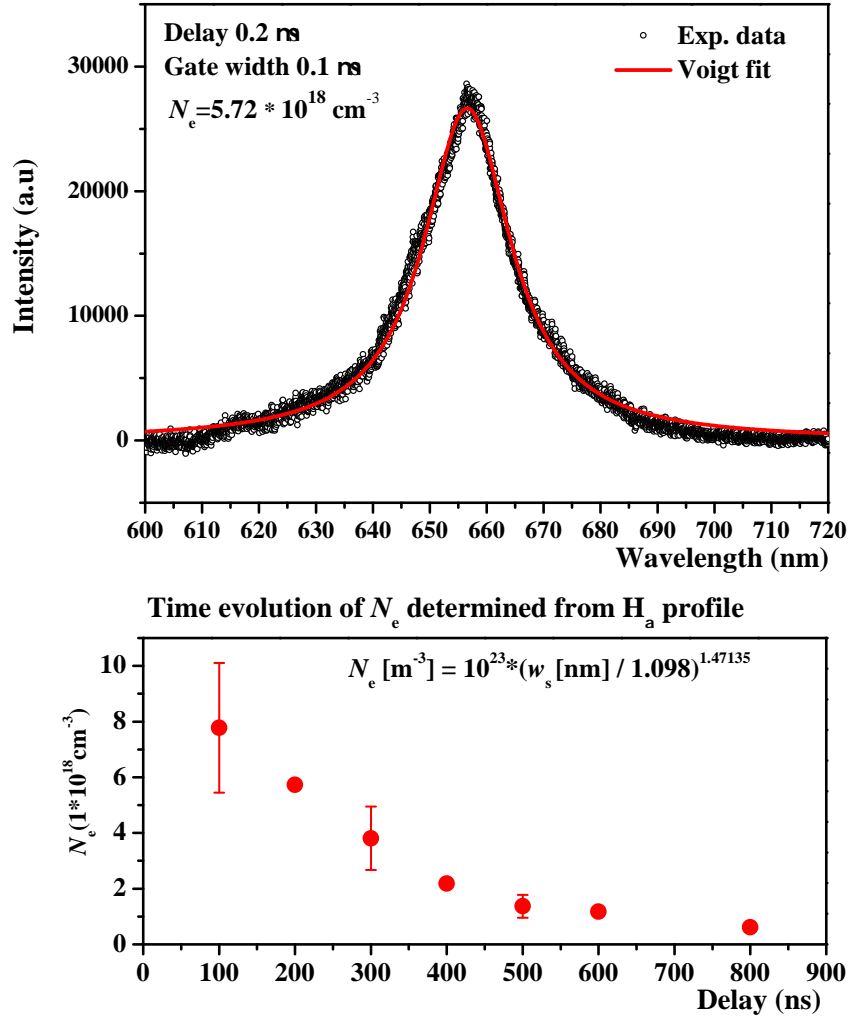


Figure 6.28: Experimental profile and Voigt fit of the H_α line at delay of $0.2 \mu\text{s}$ (upper figure) Temporal evolution of the N_e determined from the Stark widths of the H_α using the eq.6.9 (Konjević *et al.*, 2012)

One has to keep in mind that possible influence of self-absorption on the line width was not checked, which increase significantly the uncertainty in electron number density determination. In addition, the underlying physical assumptions (Kon-

jević *et al.*, 2012) used in deriving the eq.6.9 are suited to use in low electron number diagnostics, so the uncertainty of this method of N_e determination in high density plasma can not be precisely determined. Having this in mind, the error bars in the Fig.6.28, especially at the earliest delays are set to the high values ($\sim 50\%$).

Another approach used for the electron number density determination from the H_α profile is based on the whole profile fitting using the tabulated line profiles from (Gigosos *et al.*, 2003). The tables cover very wide range of the electron densities, but for the range of densities of the interest here (10^{18} cm^{-3}), assumed plasma temperatures need to be significantly higher so as to be able to neglect the effects of the plasma non-ideality and coupling effects. If neglecting the fact that the actual temperatures are supposed to be lower, determined densities are in the same range ($\pm 20\%$), while the overall agreement of the generated and experimental profiles is slightly worse than with the Voigt fit. The absence of the other lines of the hydrogen can also be used as a method for the estimation of electron number density using the Inglis-Teller relation

$$\log n = 23.26 - 7.5 \cdot \log n_{max} \quad (6.10)$$

which connects the value of the electron number density in cm^{-3} with the quantum number of the upper energy level of the last observable emission in the spectrum. (Descoeurdes, 2006). Since the last observable line is the H_α (transition from the level 3 to 2) and there was no H_β line in the spectrum (transition from the level 4 to 2) it follows

$$3 \leq n_{max} \leq 4 \quad (6.11)$$

which substituted in eq.6.10 gives the lower limit of electron number density of $6 \cdot 10^{18} \text{ cm}^{-3}$. This crude estimate agrees with the values obtained from the H_α line width at the earliest delays. One more attempt was made to obtain information about electron number density in the primary plasma phase, by matching the experimentally recorded profile of oxygen I triplet at 777 nm with the generated one using the atomic data from the (Griem, 1974) and the line parameters from the NIST database (Kramida *et al.*, 2015). The synthetic profile in the Fig. 6.29 is generated for the $T = 8000 \text{ K}$. Since the exact temperature value at this early delay can not be determined, and the temperature measurements from the continuum, integrated over the time interval 100-500 ns, gives the temperature values around

6000 K, it is believed that 8000 K represent reasonable assumption. For this electron temperature and density combination the screening parameter (or Debye shielding parameter)(Konjević, 1999) given by the equation

$$R = 8.99 \times 10^{-2} N_e^{1/6} T_e^{-1/2} \quad (6.12)$$

has the value of 1.31. Original Hooper's distribution functions for a low frequency electric micro field arising from singly charged ions which interact through the shielded Coulomb potential (Hooper Jr, 1968), used for the generation of the neutral line profile as in (Cvejić *et al.*, 2013), are given only for the values of $R < 0.8$. However, in (D'yachkov, 1998) analytical approximation for the cumulative Holtsmark and Hooper micro field distribution is presented for the values of R up to the 1.4. Although there is no physical justification for the extrapolation of $R > 1$, since the Debye radius becomes less than the ion-sphere and loses the meaning of the screening radius, formal extrapolation is possible up to the $R \cong 1.5$. In addition, this analytical approximation was compared against the Model Micro field Method in (Stehle *et al.*, 2000) and good agreement was found. It is concluded that the extrapolation is valid up to the $R < 1.4$. These results justify the use of the oxygen I triplet for the electron density measurement, and again confirm the high electron density present in the first phase of the LIP. Still, one has to keep in mind that the plasma parameters are out of the range of commonly used theories of spectral line shapes so great care is needed when applying analytical formulas and interpreting the obtained results.

6.4.2 Secondary plasma phase

If the plasma emission extinguishes within the first few hundreds of nanosecond, as often reported in the literature, than little information can be obtained from the spectra, since the continuum component is very strong in that period. But if the secondary plasma is formed, good quality line profiles can be recorded, since the spectral characteristics of the secondary plasma are much better due its expansion inside the bubble. In the spectrum of the secondary plasma no ionic emission is present since the recombination occurs fast in the primary plasma phase, and due to the low temperatures, molecular bands dominate the spectra. When working both on metallic aluminium and ceramic alumina target, blue-green AIO emission was very intensive from the 500 ns on, and it was used for the vibrational temperature

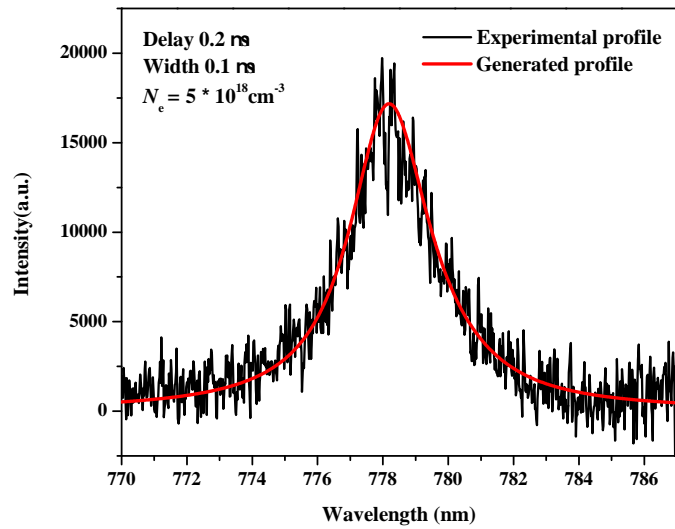


Figure 6.29: Experimental and generated profile of oxygen I triplet at delay of $0.2\mu\text{s}$. Atomic data for the generated neutral line profile are taken from the (Griem, 1974)

determination.

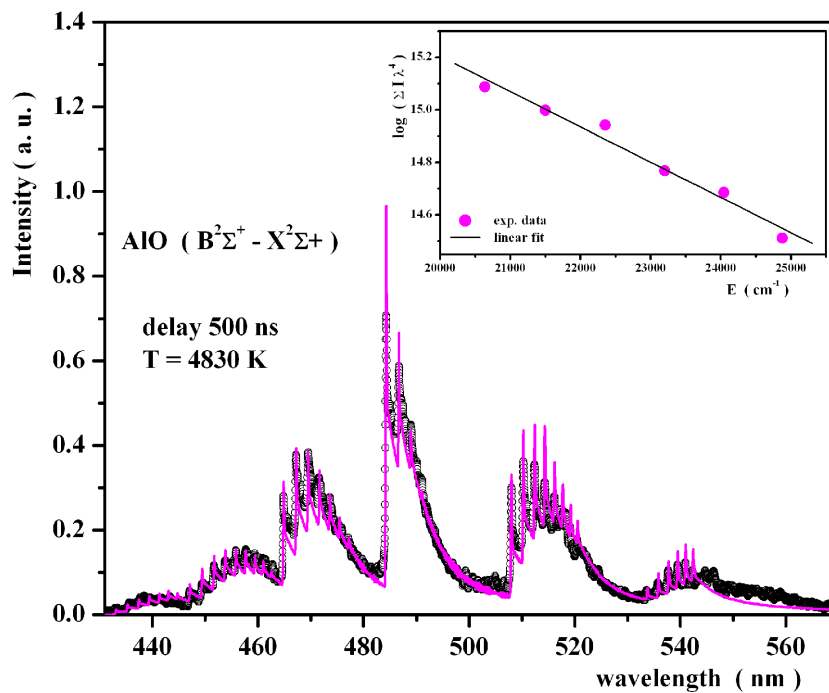


Figure 6.30: Example of recorded and synthetic spectra of AlO vibrational band. In the inset figure typical Boltzmann plot is shown. Temperatures determined from Boltzmann plot are used for synthetic spectra generation using program from (Parigger *et al.*, 2015)

In the Fig.6.30, the vibrational temperature determination for the alumina target at 0.5 μs delay is shown. Temperature was determined in two different ways. The first one is use of Boltzmann plot technique, described in (Ornstein and Brinkman, 1931), while the relevant values of the transition probabilities are taken from the ref (Sriramachandran *et al.*, 2013). Applying the summation rule of the molecular spectra, band intensities with the same initial vibrational state were summed. These sums were considered for each n' as a function of the vibrational energy. The sum of the band intensities divided by ν^4 in each n'' progression is proportional to the Boltzmann factor for the vibrational levels. Plotting these sums against the energy of vibrational levels enables temperature determination, see the inset in the Fig.6.30. The temperature determined from the Boltzmann plot was crosschecked with the synthetic spectra, generated using the program from (Parigger *et al.*, 2015). The earliest delay for which the temperature could be measured is 0.5 μs , and for the pure Al $T=5200$ K.

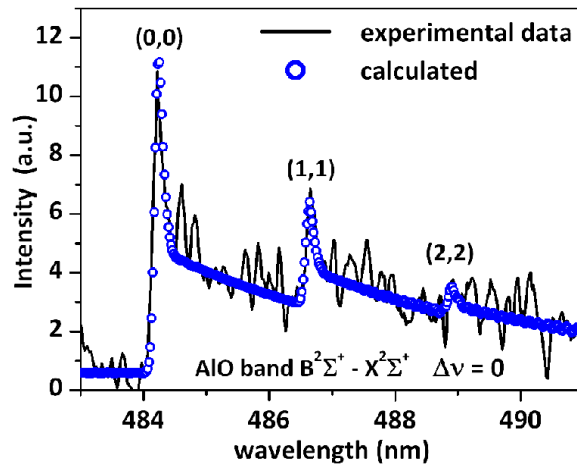


Figure 6.31: Recorded and calculated AIO band head at delay of 10 μs from the laser pulse

These temperature values indicate very special properties of the underwater plasma, where high electron number density evident from the continuum emission and very broad profiles of the few lines is at the same time obtained at relatively low temperature (~ 5000 K). As already mentioned in the Sect. 6.10, temperature determination with the use of molecular AIO band was possible up to delay of 10 μs . Example of the recorded and generated band head spectrum on the pure Al target is shown in the Fig. 6.31. The complete evolution of the temperatures determined from the vibrational AIO band on the pure Al target is given in the Fig. 6.32. It can

be concluded from there that the temperature decrease is rather slow after initial fast decay and that the bubble indeed holds the temperatures above 1000 K throughout whole period of its first oscillation as already predicted by modeling (Casavola *et al.*, 2005). This also justifies the use of relatively large gate widths of 500 ns used for the spectra recording. Thus, the main contribution to the measurement uncertainty is expected to come from any spatial inhomogeneity (spatially averaged measurements) and possible self-absorption, especially in the band head.

Since the spectrally resolved measurements doesn't give any clue about the origin of the late emission detected from within the bubble on the surface of the pure Al target, reported in the Fig. 6.8, information about the temperature values can help in narrow the search for the emission mechanisms responsible for the late emission.

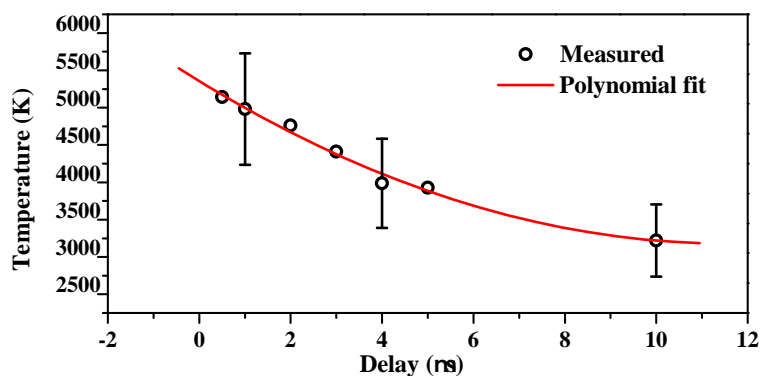


Figure 6.32: Temporal evolution of the vibrational temperatures determined from the AlO band head on the pure aluminium target

Although the contribution of blackbody radiation for the temperature of 1000K below 850 nm (detection limit of the employed camera) is just few percents, and also the quantum efficiency of the photo cathode in the iCCD is steeply decreasing in this wavelength region, the contribution of the blackbody emission cannot be completely excluded. Moreover, since during the bubble evolution temperatures inside bubble can be somewhat higher than 1000K, the contribution from the blackbody emission would increase and move towards shorter wavelengths for which the quantum efficiency is higher. Other possible explanations include the weak emission from Na impurity, which has low temperature of evaporation (~ 1156.090 K) and low lying excited level ($16973, 16956 \text{ cm}^{-1}$) and is the longest observable line in the spectrum, up to $20 \mu\text{s}$. For deeper understanding of the nature of these glowing centres, further studies are required.

Besides the molecular AlO emission, in the secondary plasma phase on the pure

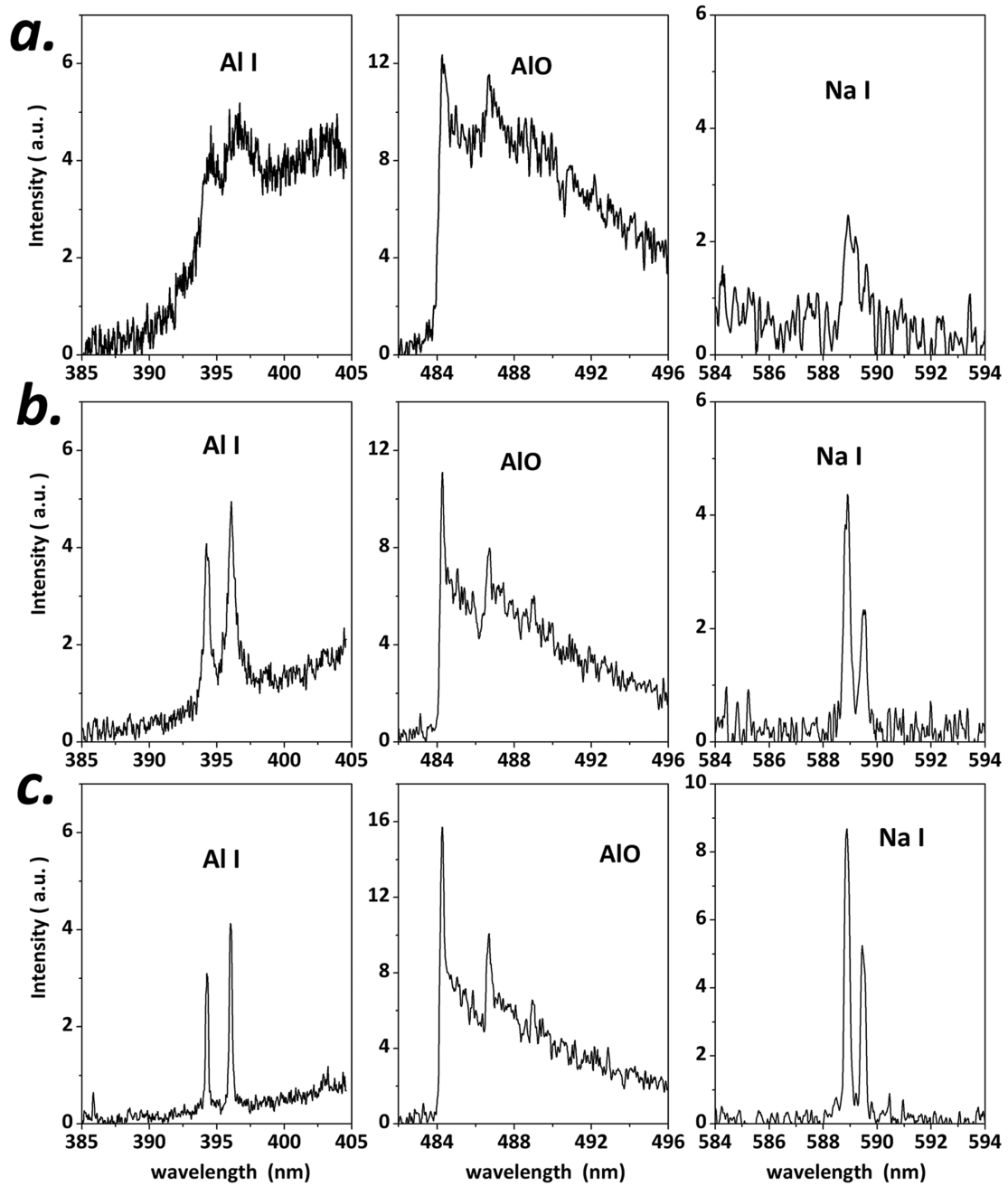


Figure 6.33: Spectra obtained with SP LIBS on aluminium target underwater with 160 accumulations: a) delay 0.5 μs gate width 0.5 μs b) delay 2 μs gate width 0.5 μs c) delay 5 μs gate width 100 μs .

Al target, lines from the main sample constituent Al I $3s^23p-2p^63p$ ($^2P^0-^2S$) and impurity sodium doublet $2p^63s-2p^63p$ ($^2S-^2P^0$) were detected. Their appearance at different delays after the laser pulse is shown in the Fig. 6.33. It can be seen that continuum emission is almost negligible for these later delays. Another interesting point is that by increasing the acquisition delay to $2\mu\text{s}$ increase in the analytical signal is observed. Comparing the spectra obtained at delay of $0.5\mu\text{s}$ and $2\mu\text{s}$, in the second case there is a significant improvement in signal strengths and quality of the lines. By setting the gate width to $100\mu\text{s}$ at delay of $5\mu\text{s}$ clearly resolved spectra with further improvement in signal to noise ratio are obtained 6.33c. The longest lasting emission is detected from Na atoms, probably due to the lowest energy of excited level. Weak Na emission was detected even at delays of $20\mu\text{s}$. This result is quite comparable with emission duration in the gas surrounding (Musazzi and Perini, 2014) (Cremers and Radziemski, 2006) (Noll, 2012)

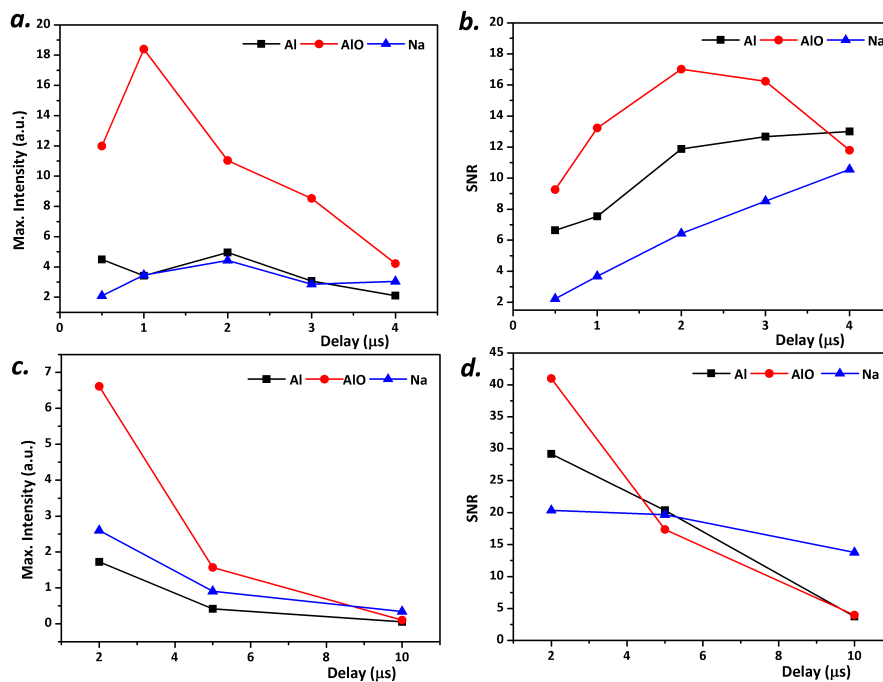


Figure 6.34: Intensity and SNR evolution of different excited species during SP LIBS on pure Al target underwater: a and b) gate width $0.5\mu\text{s}$; c and d) gate width $100\mu\text{s}$.

Evolution of the peak line intensities after the background subtraction, and the corresponding signal-to-noise ratios (SNR) are depicted in Fig. 6.34. The delay times before $0.5\mu\text{s}$ are omitted here due to a preponderant continuum contribution. Although the peak emission intensity occurs at different delays for different lines, for all of them the most intense emission is delayed in respect to the laser pulse for

1–2 μs . Late increase in the signal intensity is particularly noticeable for molecular AlO species. This is the consequence of the known fact that the optimal emission of AlO species is in the temperature range of 3500–4000 K. (Boumans, 1995) At higher temperatures AlO radicals dissociate into atoms, and at lower temperatures they form polyatomic aggregates.

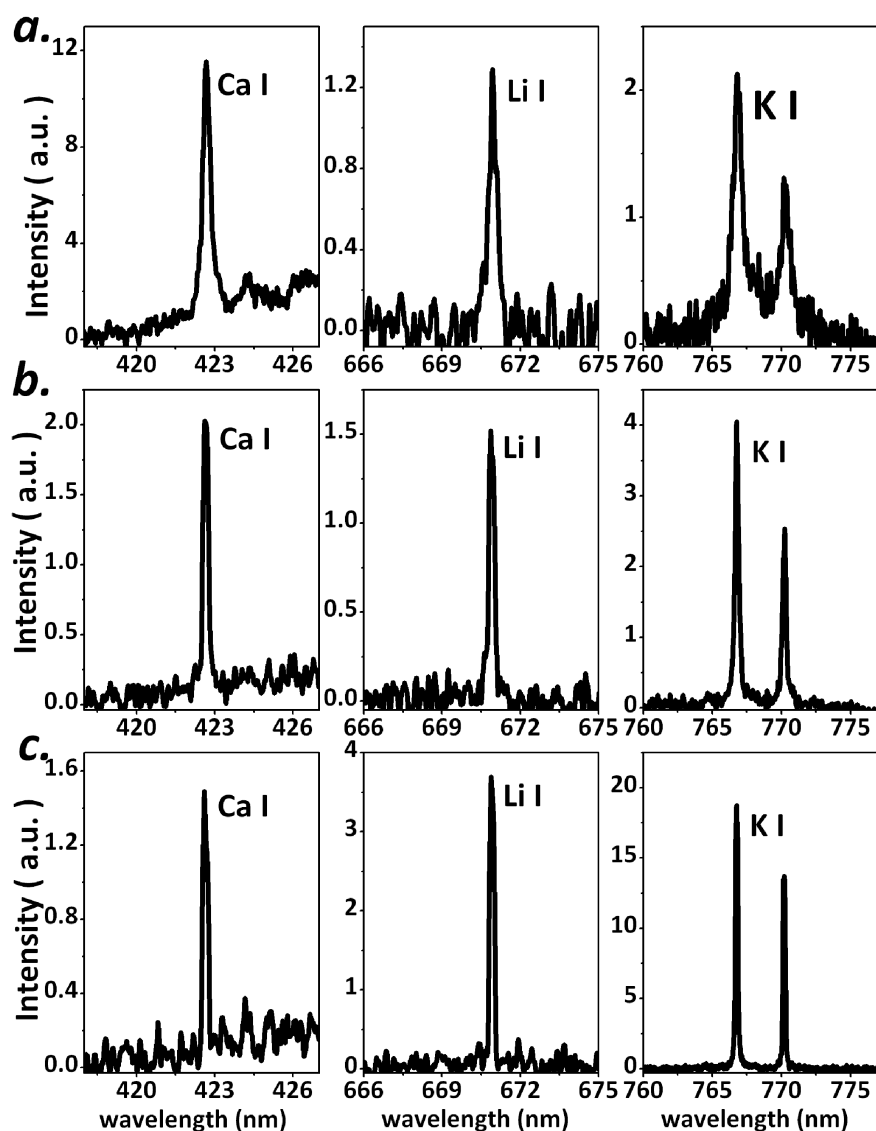


Figure 6.35: SP LIBS spectra from impurities in submerged alumina target, obtained with 160 accumulations: (a) delay: 0.5 μs , gate width: 0.5 μs ; (b) delay 2 μs , gate width 0.5 μs ; (c) delay 5 μs , gate width 100 μs .

The signal quality in terms of SNR importantly increases for longer delays, see Fig.6.34b. Peak emission intensity for molecular bands is at 2 μs delay, while the SNR of atomic lines increases up to delay of 4 μs . When the acquisition gate width is

further increased to 100 μs for secondary plasma recordings, significantly higher SNR are obtained compared to the detection of the early plasma with short acquisition gates often used in the SP LIBS experiments (De Giacomo *et al.*, 2005) (Matsumoto *et al.*, 2013a) (Suzuki *et al.*, 2002). Similar situation is also obtained for the emission from the impurities in ceramic alumina target, see Fig.6.35. In both cases, the lines are well resolved, intense and almost free of the continuum component. Judging by the FWHM (full width at half maximum) of the lines in the secondary plasma, electron number density (N_e) values are much lower. Determination of the N_e from these lines was not possible since the instrumental width of the employed spectrometer-iCCD combination was too large ($\sim 0.195\text{nm}$). Secondary plasma phase is without any abrupt changes in the pressure, temperature, shape and intensive material expulsion. Unique property of the ablation in liquids, cavitation bubble, provides plasma-friendly environment which extends the plasma emission duration, similar as in DP LIBS experiments (Cristoforetti *et al.*, 2012) (Lazic *et al.*, 2013a)

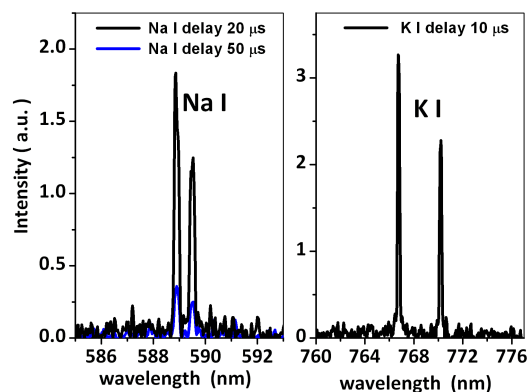


Figure 6.36: Examples of long lasting emission from low lying states of alkali elements on alumina target: black line delay 10 μs , blue line delay 50 μs .

At the beginning of its oscillation cycle, bubble dimensions are small and it efficiently prevents the exchange of the heat with the surrounding liquid. Plasma is also spatially restricted inside the bubble and remains well localized above the target, which makes possible detection of the LIBS signal during tens of microseconds. When the bubble growth becomes significant plasma no longer holds high temperature and pressure and the emission from the excited states disappears. In the case of pure Al, see Fig.6.8, position of the plasma inside the bubble is changed after tens of microseconds, leading to less efficient focusing to the spectrometer slit and hence loss of the signal. For the ceramic alumina target, however, the emission from the Na I doublet was visible even at delay of 50 μs , see Fig. 6.36. Further increase of

the optical emission duration is material related property and it will be discussed in the next section.

6.5 Influence of the target material on the laser induced breakdown in liquid medium

Appearance of the plasma at different delays after the laser pulse is shown in Fig. 6.37 for the case of metallic pure Al and ceramic alumina target. The size of the plasmas are approximately the same, but with very different shapes. In the initial phase, the plasma from the alumina target seems more homogeneous and with a more regular shape in comparison to aluminium. This can be attributed to a smaller quantity of ablated material in the case of the ceramic target, which has a very high hardness and a higher melting point compared to the metal (see Table 2 in (Gavrilović *et al.*, 2017)). Backward motion is observed on both targets at 0.1 μs after initial expansion and detachment from the target at delay of 0.06 μs . The surface of the target is still in a high temperature, melted state, and is further heated by the backward plasma motion, which lead to the evaporation and new plasma phase. Due to the large thermal conductivity of metallic Al, deposited energy spreads effectively from the interaction area, producing relatively large volume of the secondary plasma. Plasma starts to obtain flat shape, with dimension along the target significantly larger than dimension normal to the target. In contrast, on alumina the new evaporation phase initially affects only a narrow region around the laser spot while the position of the maximum intensity of the plasma region remains well above the target surface.

Right after the laser impacts the target, plasma on the alumina has higher intensity which decays more slowly compared to the plasma on pure aluminium. But on aluminium, intensity enhancement occurs at $\sim 0.5 \mu\text{s}$, see Fig. 6.5 due to efficient and extended secondary plasma formation, connected to the material's high conductivity, low melting/evaporation temperature (933/2753 K (Totten and MacKenzie, 2003)) and to certain extent higher ablation rate. On alumina, on the other hand intensity enhancement is very small due to the narrower thermally affected region and higher melting/evaporation temperatures (2327/3250 K (Garcia-Giron *et al.*, 2016) (Samant and Dahotre, 2009)). The influence of these difference in the plasma intensity are visible in the OES of the primary plasma also, see Fig. 6.38.

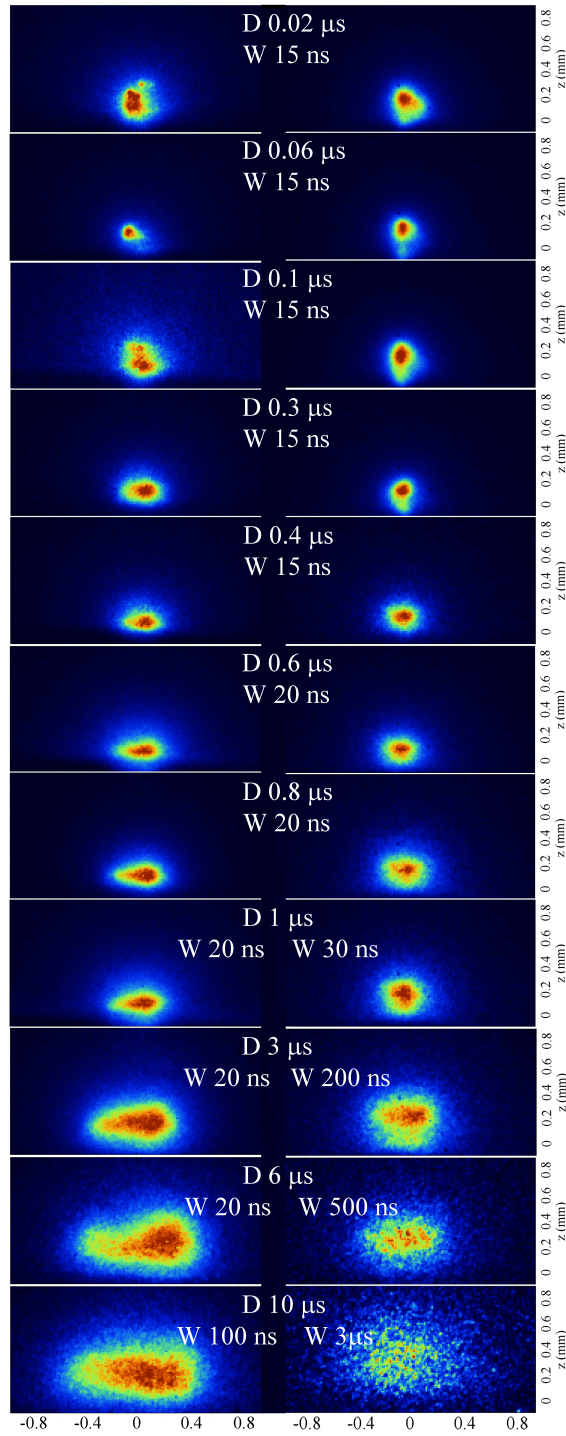


Figure 6.37: Plasma evolution on different target materials placed on the bottom, left column – pure aluminium , right column –alumina target

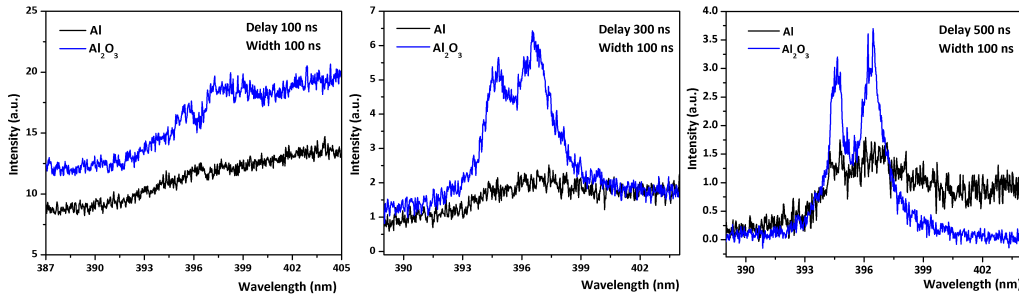


Figure 6.38: LIBS emission from Al I lines recorded at short acquisition delays on the two target materials

Although the formation of the secondary plasma on alumina is less efficient than on the pure Al, on a larger timescale, the overall emission intensity above alumina target drops to an almost constant value after $\sim 30\mu\text{s}$ and then persists up to $650\mu\text{s}$, longer than the emission on the pure Al which has slower decay but diminishes with the first bubble collapse around $475\mu\text{s}$. Emission on alumina survives the bubble collapse, and even gain in the intensity in the moments that correspond to the bubble collapse, which on the alumina happens at $350\mu\text{s}$. This intensity enhancement is visible at delay $380\mu\text{s}$ in the Fig 6.9 The reasons for this extremely persistent emission on alumina can be various and some of them are listed below:

- Low thermal conductivity of alumina in comparison to aluminium, previously mentioned in the context of the less efficient secondary plasma formation, might have beneficial effect in this phase, since it helps maintaining the high temperature of the vapour inside the bubble, where heat exchange with the surrounding water (thermal conductivity $\sim 0.6\text{ W m}^{-1}\text{K}^{-1}$ only) is very slow;
- The temperature of the melted alumina layers created by the laser pulse and to a lesser extent by the backward propagating plasma decays slowly: a high temperature state for the melted alumina can persist for several seconds (Zhang and Modest, 1998)(Bityukov *et al.*, 2008) (Bityukov and Petrov, 2013)(Vadim A Petrov, 2007) accompanied by optical emission in the visible spectral range.(Bityukov *et al.*, 2008) This sort of temperature plateau during the cooling of alumina has also been observed for other materials,(Sola *et al.*, 1997) with a duration proportional to the depth of the modified layer. If melted layer several microns thick is assumed and the scaling of the solidification time is performed according to the results of (Bityukov *et al.*, 2008)(Geiger *et al.*, 1996), the expected time for duration of the high temperature state on the alumina surface matches to the timescales of the plasma persistence

6.5 Influence of the target material on the laser induced breakdown in liquid medium

– Alkali impurities present in alumina (Na, Li and K) have low energies of excited states, thus contribution to the overall signal.

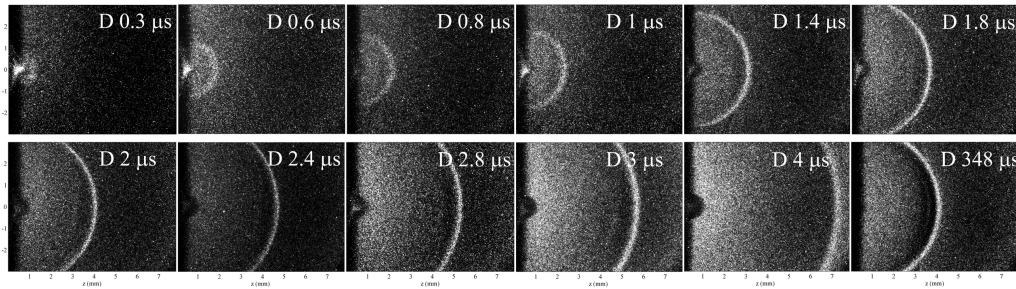


Figure 6.39: Images of the shock wave on alumina obtained using the Schlieren technique, at different delays D from the laser pulse

Differences of the optical emitting regions at late delays can be seen by comparing Fig.6.8 and Fig. 6.9 On the alumina target up to delay of $20\mu\text{s}$ plasma occupies almost entire bubble volume, while at later delays the strongest emission is coming from the thin layer in the contact with the target. The luminous central spot can be attributed both to the optical effects of the bubble described in Sect.6.2.2 and to the position of the laser induced crater, where the temperature is the highest. In contrast, on aluminium target, optical emission is spread throughout the bubble volume and many luminous centres are visible. In the fig. 6.39 similar time evolution of the shock wave obtained for the ceramic α -alumina target is shown. Initial speed is just slightly lower, 2.9km/s , while the release of the second shock wave is occurring much earlier, about $350\mu\text{s}$ after the laser pulse.

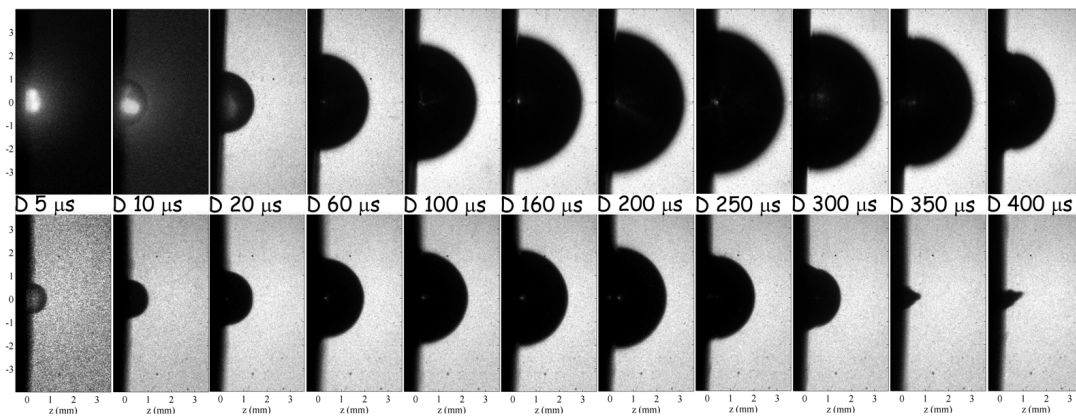


Figure 6.40: Bubble evolution on different target materials: top row – pure aluminium, bottom row – alumina target

Comparison of the bubble evolution on the two targets is given in the Figs.6.40-6.41. The radius of the bubble is larger on aluminium (3.2 mm) than on alumina (2.3 mm),

where the bubble's collapse time is also longer. Using the equations 6.6 and 6.5 as in ref.(Gavrilović *et al.*, 2016) ,(Cristoforetti *et al.*, 2012)(Sasaki *et al.*, 2009)(Thornton *et al.*, 2013)(Franc and Michel, 2004) for the energy stored inside the vapour cavity after the ablation of alumina is estimated to be 3.1 mJ, about three times lower than on aluminium under the same experimental conditions.

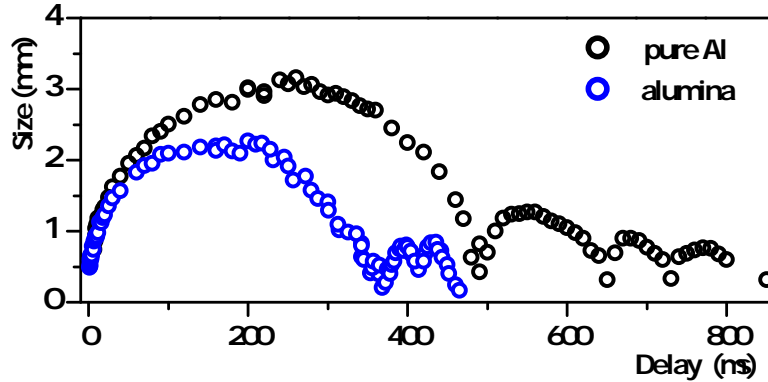


Figure 6.41: Bubble size on different materials determined from fast shadowgraphy measurements

In Fig. 6.42 the Al I, AlO and Na I lines produced by laser ablation of both targets, detected at delays of $0.5 \mu\text{s}$, $2 \mu\text{s}$ and $5 \mu\text{s}$, are shown comparatively. The significant difference between the Na I doublet intensities from the two targets is due to the larger quantity of material impurities in alumina compared to the aluminium sample. Due to a relatively weak continuum component in the secondary plasma on alumina the considered transitions are of a good quality already at a delay of $0.5 \mu\text{s}$, while for the pure Al the lines are well resolved at delays of $2 \mu\text{s}$ or longer. On the other hand, since the secondary plasma formation is more efficient on the metallic target than on the ceramic one, at longer delays the Al I lines and the AlO band become more intense on aluminium than on alumina. Using a gate width of $0.5 \mu\text{s}$, see Fig. 6.42b,c, on aluminium the maximum Al I intensity and SNR were obtained at a delay of $2 \mu\text{s}$. In contrast, on the alumina target the Al I intensity and SNR are the highest at a delay of $0.5 \mu\text{s}$. For both targets, the emission from Na I decays slowly starting from $2\text{-}3 \mu\text{s}$ of delay and reaches its maximum SNR later than the other transitions. Delayed appearance of the emission from the alkali elements could also be due to the time needed for the plasma to fully expand and atoms of alkali elements to be immersed inside the plasma(De Giacomo *et al.*, 2004).

Important conclusion is that by increasing the acquisition gate width up to $100 \mu\text{s}$ and detecting the LIBS spectra only from the secondary plasma, both the line

intensities and their SNR values show a large increase irrespective of the target material.

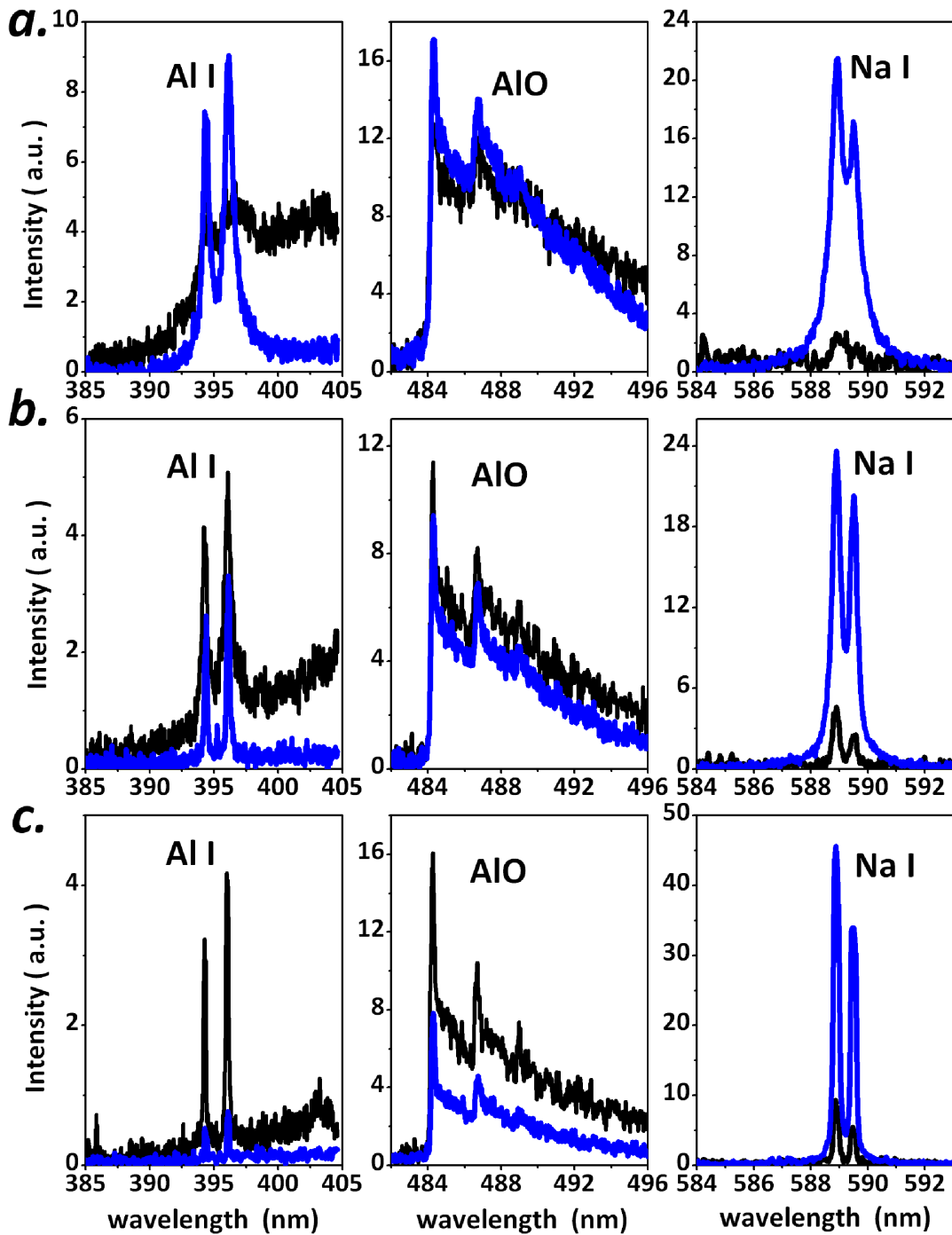


Figure 6.42: SP LIBS spectra from α -alumina (blue) and pure Al target (black) underwater obtained with 160 accumulations: (a) delay 0.5 μ s, gate width 0.5 μ s, (b) delay 2 μ s, gate width: 0.5 μ s and (c) delay: 5 μ s, width 100 μ s

Chapter 7

Conclusion

The mutual influences of the cavitation bubble and plasma emission, created by the ablation with single pulse from the commercial nanosecond laser source, are studied here. The presented study is primarily focused on different mechanical and optical phenomena of SP laser induced breakdown (LIB) on the metallic aluminium and ceramic alumina target in water, with special attention on the late stage of the plasma evolution. Several experimental techniques including fast photography, Schlieren, shadowgraphy, probe beam techniques and optical emission spectroscopy are used to give insight in the plasma formation and evolution, shock wave propagation, cavitation bubble dynamics, and plasma spectral emission.

At first, differences between the plasmas formed in the liquid and the gaseous surrounding were investigated experimentally using plasma photography to track the spatial and temporal evolution of the plasma formed on the ceramic α -alumina target. From the series of the photographs, strong influence of the confining liquid media on the size and the propagation speed of the plasma is clearly observable. In contrast to the commonly accepted opinion about the short lived plasmas inside liquid, when comparative studies of the plasmas in air and liquid were made, the emission from the plasma in liquid, although much weaker, appeared also up to delay of 10 μ s. Since this was an unusual and rarely reported result, the investigation continued in this direction, and very long lasting optical emissions comparable to bubble collapse time (few hundreds of μ s) were detected both for the pure, metallic aluminium and ceramic alumina target in underwater SP laser ablation.

Besides long duration, plasma obtained in this study shows another particular feature. Namely, plasma evolves in the two characteristic phases. After the initial plasma formation by the laser pulse, followed by its detachment from the target and

collapse to a small volume, the plasma grows back to the target, and approximately after the 500 ns, the formation of the secondary plasma is observed. On the thermally conductive aluminium, the backward propagating plasma finds an enlarged heated area, which together with the low vaporization temperature of the material leads to efficient secondary target evaporation. The shape of the secondary plasma is initially flattened on the sample surface and its overall emission increases during the first 2 μ s. Low thermal conductivity of alumina on the other hand, keeps the backward plasma-target interaction in proximity of the laser induced crater, where a high temperature in the surface layers is present, and also prevents important heat losses of the plume through the target. Simultaneously, a high vaporization temperature of the material limits the emission of the sample material into the vapour bubble leading to a less efficient secondary plasma formation compared to the metallic target. The backward interacting plume on alumina is slightly elliptical and inside the expanded vapour bubble it is reduced to a glowing point close to the hot crater. The transition between the primary and secondary plasma phases is evidenced by observing the photographs, and even more clearly, after performing some basic manipulation over the image matrix, for which the programming routines were developed.

Further, the mutual relations of the plasma and the bubble were investigated on the example of the two chosen target materials. It was shown that duration of the optical emission on the pure Al target coincides with the collapse of the laser produced bubble, and it is concluded that the unique temperature and pressure conditions inside the bubble favour this long lasting optical emission. In this late stage, plasma on aluminium is no more compact. and lot of glowing centres were detected from the whole bubble volume. Even though the process of the secondary plasma formation is less efficient on ceramic alumina target, the total duration of emission exceeds the lifetime of the bubble, and even certain increase in emission intensity is detected after the bubble collapse. The long lasting optical emission remains well confined inside the bubble, but without visible particle clustering detected in the case of metallic aluminium. Dedicated comparison between all the studied phenomena on the two target materials is given in the separate section, and is shown graphically below, Fig. 7.1

In addition to the studies of bubble influence on the duration of plasma emission, bubble influence on the signal collection efficiency is also investigated. Due to the lowering of its index of refraction with the expansion, bubble enhances Snell's

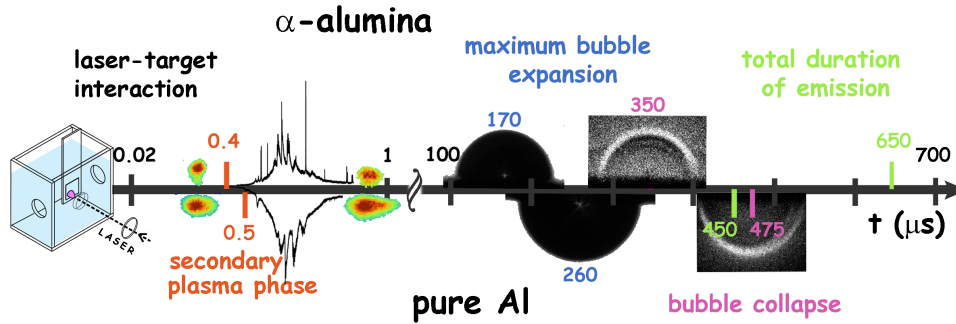


Figure 7.1: Graphical comparison of the timescale of LIB processes on two different target materials

reflections at its surface which alters significantly the propagation of light rays. This influence in some cases can even be positive, since it enables detection of the outer part of the plasma emission otherwise lost for the detection, by forming a bright central spot. Multiple reflections and refractions inside the bubble are used here to derive the expression for the calculation of the refractive index of the bubble, which was found to change during the bubble evolution. It is proven that bubble alters significantly spatial distribution of the plasma emission and this important factor needs to be taken into account when optimizing the optics collection system. These effects are also very important for DP LIBS and other applications where the laser beam propagates through the laser formed bubble, like the probe beam techniques used in this study to resolve the dynamics of the cavitation bubble. Probe beam techniques have proven to be very convenient and cheaper comparative method, which under the right experimental configuration can provide information about the whole bubble dynamics from the one laser shot. Bubble sizing was performed from the scattering and transmission measurements, and also from the fast shadowgraphy images with the use of the routine for extracting the bubble dimensions from the dimensionally calibrated images. Information about the bubble size and the bubble collapse time obtained from the second shock wave recorded with the schlieren technique, served to calculate the energy contained in the bubble, while the shock front propagation was used for the evaluation of the pressures developed in the interaction area.

Optical emission spectroscopy analysis is also divided in the two sections which correspond to the two plasma phases. In the first stage, immediately after the laser pulse and with duration of less than 500 ns, the plasma rapidly expands and decays, where the optical emission is characterized by an intense continuum component and very large widths of the detected lines. Here, the LIBS signal has a poor quality

in terms of the spectral resolution and signal-to-noise ratio. The program for the continuum component determination and subtraction from the experimental spectra was made, which calculates the temperature from the Wien's displacement law. Electron temperature deduced from the continuum emission was found to be in the range 6000–7000 K. Electron number density is determined in the primary plasma phase on alumina from the H_{α} line, oxygen triplet and by using the Inglis-Teller limit, obtaining the values above $6 \cdot 10^{18} \text{ cm}^{-3}$. The plasma conditions suggest the non-ideal plasma case, and the implications for the electron number density determination are discussed in short. The LIBS signal detected from the secondary plasma on aluminium is very intense at the beginning, but later suppressed also by the particle formation and the heat dissipation through the target. The secondary plasma phase starts from the backward reheated target. Its emission has a stable position close to the target and still growing intensity over tens of microseconds from the pulse, which enables the use of a large number of accumulations to obtain the better quality of lines.

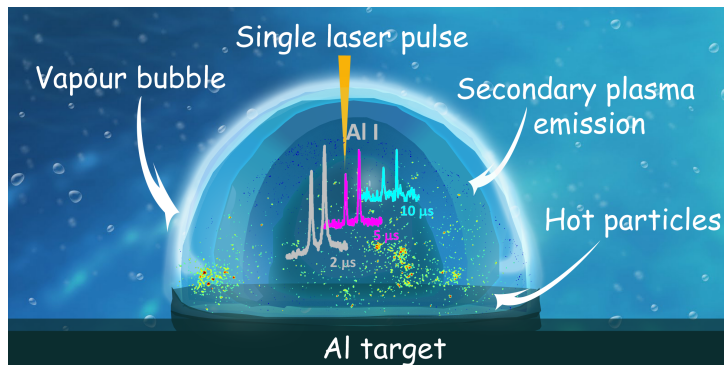


Figure 7.2: Sketch of the processes occurring after LIB on the Al target

The secondary plasma has significantly lower electron densities with respect to the first plasma stage, hence it is almost free from the continuum component. Temperatures in the secondary plasma phase are around 5000K, as determined from the vibrational AlO bands on both target materials. The LIBS spectra from the secondary plasma contain the lines from low excited levels and have a good quality, with very narrow transitions almost free of the continuum component. The intensities of the emission lines decay below the detection limit at delays in order of $10 \mu\text{s}$, whereas Na I doublet remains visible even after $50 \mu\text{s}$ from the laser pulse on alumina target. Sketch of the processes induced after LIB on a metallic aluminium target 7.2, where the bubble, plasma emission and particles inside the bubble are all present at the same time, serves to illustrate the complexity of the phenomena

that needs to be studied in order to understand the SP LA in the liquid.

In summary, a good quality LIBS spectra after underwater laser ablation with ns pulses from a commercial laser source can be obtained by detecting only the delayed, long lasting plasma and avoiding the initial explosive phase, characterized by high electron density, intense continuum and a very few, strongly broadened emission lines. With the proposed experimental approach, LIBS detection of underwater plasma is feasible both on metallic and ceramic samples, also by using a not gated and a relatively cheap CCD or camera. In the process of the sustaining and detecting the plasma emission the role of the cavitation bubble proved to be extremely important.

Bibliography

- Abraham, E., Minoshima, K. and Matsumoto, H. (2000), Femtosecond laser-induced breakdown in water: time-resolved shadow imaging and two-color interferometric imaging, *Optics Communications* **176**, 441–452. 20
- Adamson, M., Padmanabhan, A., Godfrey, G. and Rehse, S. (2007), Laser-induced breakdown spectroscopy at a water/gas interface: A study of bath gas-dependent molecular species, *Spectrochim. Acta Part B* **62**, 1348–1360. 82
- Akhatov, I., Lindau, O., Topolnikov, A., Mettin, R., Vakhitova, N. and Lauterborn, W. (2001), Collapse and rebound of a laser-induced cavitation bubble, *Phys. Fluids* **13**, 2805–2819. 21
- Al-Mamun, S. A., Nakajima, R. and Ishigaki, T. (2013), Tuning the size of aluminum oxide nanoparticles synthesized by laser ablation in water using physical and chemical approaches, *J. Coll. Int. Sci.* **392**, 172–182. 14
- Alexiou, S. (2005), Stark broadening of hydrogen lines in dense plasmas: Analysis of recent experiments, *Phys. Rev. E* **71**, 066403, 11pp. 43
- Alexiou, S. and Leboucher-Dalimier, E. (1999), Hydrogen balmer- α broadening in dense plasmas, *Phys. Rev. E* **60**, 3436–3438. 43
- Alloncle, A., Dufresne, D. and Autric, M. (1994), Pressure waves induced in liquid under high laser irradiation, *J. de Physique IV* **4**, 131–134. 19, 20
- Amendola, V. and Meneghetti, M. (2013), What controls the composition and the structure of nanomaterials generated by laser ablation in liquid solution?, *Phys. Chem. Chem. Phys.* **15**, 3027–3046. 5, 13
- Bai, X., Ma, Q., Perrier, M., Motto-Ros, V., Sabourdy, D., Nguyen, L., Jalocha, A. and Yu, J. (2013), Experimental study of laser-induced plasma: Influence of laser fluence and pulse duration, *Spectrochim. Acta Part B* **87**, 27–35. 3

- Bang, J. H. and Suslick, K. S. (2010), Applications of ultrasound to the synthesis of nanostructured materials, *Adv. Mater.* **22**, 1039–1059. 3
- Barber, B. P. and Putterman, S. J. (1992), Light scattering measurements of the repetitive supersonic implosion of a sonoluminescing bubble, *Phys. Rev. Lett.* **69**, 3839–3842. 29, 31, 77
- Barcikowski, S. and Compagnini, G. (2013), Advanced nanoparticle generation and excitation by lasers in liquids, *Phys.Chem. Chem. Phys.* **15**, 3022–3026. 13
- Barcikowski, S., Devesa, F. and Moldenhaueri, K. (2009), Impact and structure of literature on nanoparticle generation by laser ablation in liquids, *J. Nanopart. Res.* **11**, 1883–1893. 13
- Barnes, P. A. (1969), *Studies of laser induced breakdown phenomena in liquid water*, Simon Fraser University,thesis. 32
- Beddows, D., Samek, O., Liška, M. and Telle, H. (2002), Single-pulse laser-induced breakdown spectroscopy of samples submerged in water using a single-fibre light delivery system, *Spectrochim. Acta Part B* **57**, 1461–1471. 15
- Benjamin, T. B. and Ellis, A. T. (1966), The collapse of cavitation bubbles and the pressures thereby produced against solid boundaries, *Philos. Trans. R. Soc. London, Ser. A* **260**, 221–240. 28
- Bityukov, V. K. and Petrov, V. A. (2013), Absorption coefficient of molten aluminum oxide in semitransparent spectral range, *Appl. Phys. Research* **5**, 51–71. 96
- Bityukov, V. K., Vorobev, A. Y., Petrov, V. A. and Titov, V. E. (2008), The radiation of alumina melt in the visible and near ir spectra upon solidification in the process of cooling in ambient air, *High Temperature* **46**, 782–794. 96
- Böddeker, S., Günter, S., Könies, A., Hitzschke, L. and Kunze, H.-J. (1993), Shift and width of the h_{α} line of hydrogen in dense plasmas, *Phys. Rev. E* **47**, 2785–2791. 43
- Bongiovanni, C., Chevaillier, J. P. and Fabre, J. (1997), Sizing of bubbles by incoherent imaging: defocus bias, *Exp. in Fluids* **23**, 209–216. 65, 68
- Bongiovanni, C., Dominguez, A. and Chevaillier, J.-P. (2000), Understanding images of bubbles, *Eur. J. Phys.* **21**, 561–570. 65

- Boumans, P. W. J. M. (1995), *Theory of Spectrochemical Excitation*, Springer US. 92
- Brennen, C. E. (1995), *Cavitation and Bubble Dynamics*, Oxford University Press, Inc. 20, 22
- Brenner, M. P., Hilgenfeldt, S. and Lohse, D. (2002), Single-bubble sonoluminescence, *Rev. Mod. Phys.* **74**, 425–484. 3, 21, 26
- Brujan, E.-A., Nahen, K., Schmidt, P. and Vogel, A. (2001), Dynamics of laser-induced cavitation bubbles near an elastic boundary, *J. Fluid Mech.* **433**, 251–281. 28
- Büscher, S., Wrubel, T., Ferri, S. and Kunze, H.-J. (2002), The stark width and shift of the hydrogen $h\alpha$ line, *J. Phys. B: At. Mol. Opt. Phys.* **35**, 2889–2897. 43
- Calisti, A., Bureyeva, L., Lisitsa, V., Shuvaev, D. and Talin, B. (2007), Coupling and ionization effects on hydrogen spectral line shapes in dense plasmas, *Eur. Phys. J. D* **42**, 387–392. 43
- Casavola, A., De Giacomo, A., Dell'Aglio, M., Taccogna, F., Colonna, G., De Pascale, O. and Longo, S. (2005), Experimental investigation and modelling of double pulse laser induced plasma spectroscopy under water, *Spectrochim. Acta Part B* **60**, 975–985. 26, 63, 89
- Chen, J., Li, X., Gua, Y., Wang, H., Song, X. and Zeng, H. (2017), Probing mesoscopic process of laser ablation in liquid by integrated method of optical beam deflection and time-resolved shadowgraphy, *J. Coll. Int. Sci.* **489**, 38–46. 13, 21, 38, 71, 73
- Chen, X., Xu, R.-Q., Chen, J.-P., Shen, Z.-H., Jian, L. and Ni, X.-W. (2004), Shock-wave propagation and cavitation bubble oscillation by nd:yag laser ablation of a metal in water, *Appl. Opt.* **43**, 3251–3257. 71, 73
- Chu, H.-C., Vo, S. and Williams, G. A. (2009), Precursor luminescence near the collapse of laser-induced bubbles in alkali-salt solutions, *PRL* **102**, 204301, 4pp. 3
- Cirisan, M., Cvejić, M., Gavrilović, M., Jovićević, S., Konjević, N. and J.Hermann (2014), Stark broadening measurement of al ii lines in a laser-induced plasma, *J. Quant. Spectrosc. Radiat. Transfer.* **133**, 652–662. 4

- Cremers, D. A. and Radziemski, L. J. (2006), *Handbook of Laser-Induced Breakdown Spectroscopy*, John Wiley & Sons Ltd. 4, 40, 91
- Cristoforetti, G., Tibberi, M., Simonelli, A., Marsili, P. and Giammanco, F. (2012), Toward the optimization of double-pulse libs underwater: effects of experimental parameters on the reproducibility and dynamics of laser-induced cavitation bubble, *Appl. Opt.* **51**, B30–B41. 5, 21, 26, 27, 45, 70, 93, 98
- Crum, L. A., J., T., Reisse, M. J. L. and Suslick, K. S. (1999), *Sonochemistry and Sonoluminescence*, Springer Science+Business Media Dordrecht. 29
- Cvejić, M., Gavrilović, M., Jovićević, S. and Konjević, N. (2013), Stark broadening of mg i and mg ii spectral lines and debye shielding effect in laser induced plasma, *Spectrochim. Acta Part B* **85**, 20–33. 4, 86
- Cvejić, M., Stambulchik, E., Gavrilović, M., Jovićević, S. and Konjević, N. (2014), Neutral lithium spectral line 460.28 nm with forbidden component for low temperature plasma diagnostics of laser-induced plasma, *Spectrochim. Acta Part B* **100**, 86–97. 4
- De Giacomo, A., De Bonis, A., DellAglio, M., De Pascale, O., Gaudiuso, R., Orlando, S., Santagata, A., Senesi, G. S., Taccogna, F. and Teghil, R. (2011), Laser ablation of graphite in water in a range of pressure from 1 to 146 atm using single and double pulse techniques for the production of carbon nanostructures, *J. Phys. Chem. C* **115**, 5123–5130. 41
- De Giacomo, A., DellAglio, M., Casavola, A., Colonna, G., De Pascale, O. and Capitelli, M. (2006), Elemental chemical analysis of submerged targets by double-pulse laser-induced breakdown spectroscopy, *Anal. Bioanal. Chem.* **385**, 303–311. 15
- De Giacomo, A., DellAglio, M., Colao, F. and Fantoni, R. (2004), Double pulse laser produced plasma on metallic target in seawater: basic aspects and analytical approach, *Spectrochim. Acta Part B* **59**, 1431–1438. 21, 98
- De Giacomo, A., DellAglio, M., Colao, F., Fantoni, R. and Lazic, V. (2005), Double-pulse libs in bulk water and on submerged bronze samples, *Appl. Surf. Sci* **247**, 157–162. 15, 41, 93

- De Giacomo, A., Dell'Aglio, M., Gaudio, R., Amoroso, S. and Pascale, O. D. (2012), Effects of the background environment on formation, evolution and emission spectra of laser-induced plasmas, *Spectrochim. Acta, Part B* **78**, 1–19. 3, 39, 41
- De Giacomo, A., Dell'Aglio, M., O.De Pascale and Capitelli, M. (2007), From single pulse to double pulse ns-laser induced breakdown spectroscopy under water: Elemental analysis of aqueous solutions and submerged solid samples, *Spectrochim. Acta, Part B* **62**, 721–738. 5, 6, 27, 38, 41, 44, 55, 83
- De Giacomo, A., Dell'Aglio, M., Santagata, A., Gaudio, R., De Pascale, O., Wagnener, P., Messina, G. C., Compagnini, G. and Barcikowski, S. (2013), Cavitation dynamics of laser ablation of bulk and wire-shaped metals in water during nanoparticles production, *Phys.Chem.Chem.Phys.* **13**, 3083–3092. 14, 27, 28, 60, 61
- De Giacomo, A., Gaudio, R., Dell'Aglio, M. and Santagata, A. (2010), The role of continuum radiation in laser induced plasma spectroscopy, *Spectrochim. Acta Part B* **65**, 385–394. 41, 80
- Dean, C. E. and Marston, P. L. (1991), Critical angle light scattering from bubbles: an asymptotic series approximation, *Appl. Opt.* **30**, 4764–4776. 31
- Dehaeck, S. and van Beeck, J. P. A. J. (2007), Simultaneous determination of bubble diameter and relative refractive index using glare circles, *Appl. Opt.* **46**, 5957–5963. 65, 66
- Delale (Ed.), C. (2013), *Bubble Dynamics & Shock Waves*, *SHOCKWAVES* 8, Springer-Verlag Berlin Heidelberg. 3, 19, 78
- Dell'Aglio, M., Gaudio, R., De Pascale, O. and De Giacomo, A. (2015), Mechanisms and processes of pulsed laser ablation in liquids during nanoparticle production, *Applied Surface Science* **348**, 4–9. 5, 55
- Descoeur, A. (2006), *characterization of electrical discharge machining plasmas*, École polytechnique fédérale de Lausanne. 82, 85
- Descoeur, A., Hollenstein, C., Walder, G., Demellayer, R. and Perez, R. (2008), Time- and spatially-resolved characterization of electrical discharge machining plasma, *Plasma Sources Sci. Technol.* **17**, 024008, 10pp. 82

- Descoeurdes, A., Hollenstein, C., Walder, G. and Perez, R. (2005), Time-resolved imaging and spatially-resolved spectroscopy of electrical discharge machining plasma, *J. Phys. D: Appl. Phys.* **38**, 4066–4073. 82
- Detalle, V., Sabsabi, M., St-Onge, L., Hamel, A. and Heon, R. (2003), Influence of er:yag and nd:yag wavelengths on laser-induced breakdown spectroscopy measurements under air or helium atmosphere, *Appl. Opt.* **42**, 5971–5977. 3
- Diaci, J. and Mozina, J. (1995), Multiple-pass laser beam deflection probe for detection of acoustic and weak shock waves in fluids, *Rev. Sci. Instrum.* **66**, 4644–4648. 70
- Docchio, F., Regondi, P., Capon, M. R. C. and Mellerio, J. (1988), Study of the temporal and spatial dynamics of plasmas induced in liquids by nanosecond nd:yag laser pulses. 1: Analysis of the plasma starting times, *Appl. Opt.* **27**, 3661–3668. 32
- Docchio, F. and Sacchi, C. A. (1988), Shielding properties of laser-induced plasmas in ocular media irradiated by single nd:yag pulses of different durations, *Investigative Ophthalmology & Visual Science* **29**, 437–443. 12
- Docchio, F., Sacchi, C. A. and Marshall, J. (1986), Experimental investigation of optical breakdown thresholds in ocular media under single pulse irradiation with different pulse durations, *Lasers Ophthalmol.* **1**, 83–93. 36
- Duocastella, M., Fernandez-Pradas, J. M., Morenza, J. L. and Serra, P. (2009), Time-resolved imaging of the laser forward transfer of liquids, *J. Appl. Phys.* **106**, 1084907, 7pp. 15
- D’yachkov, L. (1998), Approximation for the probabilities of the realization of atomic bound states in a plasma, *J. Quant. Spectrosc. Radiat. Transfer* **59**, 65–69. 86
- Ellis, A. T. (1953), *Observation on cavitation bubble collapse*, Thesis, California Institute of Technology. 28
- Escarguel, A., Ferhat, B., Lesage, A. and Richou, J. (2000), A single laser spark in aqueous medium, *J. Quant. Spectrosc. Radiat. Transfer.* **64**, 353–361. 42, 43, 82
- Escarguel, A., Oks, E., Richou, J. and Volodko, D. (2000), Highly nonlinear, sign-varying shift of hydrogen spectral lines in dense plasmas, *Phys. Rev. E* **62**, 2667–2671. 43

- Feng, Q., Moloney, J. V., Newell, A. C., Wright, E. M., Cook, K., Kennedy, P. K., Hammer, D. X., Rockwell, B. and Thompson, C. R. (1997), Theory and simulation on the threshold of water breakdown induced by focused ultrashort laser pulses, *IEEE J. Quantum Electron* **33**, 127–137. 34
- Fortes, F. J., Guirado, S., Metzinger, A. and Laserna, J. J. (2015), A study of underwater stand-off laser-induced breakdown spectroscopy for chemical analysis of objects in the deep ocean, *J. Anal. At. Spectrom.* **30**, 1050–1056. 15
- Fortes, F. J., Moros, J., Lucena, P., Cabalín, L. M., and Laserna, J. J. (2013), Laser-induced breakdown spectroscopy, *Appl. Spectrosc.* **85**, 640–669. 4, 15
- Fortov, V. E. and Iakubov, I. T. (2000), *The Physics of Non-Ideal Plasma*, World Scientific Publishing Co. Pte. Ltd. 42
- Franc, J.-P. and Michel, J.-M. (2004), *Fundamentals of Cavitation*, Kluwer Academic Publishers. 20, 22, 70, 98
- Gaitan, D. F. and Holt, R. G. (1999), Experimental observations of bubble response and light intensity near the threshold for single bubble sonoluminescence in an air-water system, *Phys. Rev. E* **59**, 5495–5502. 3
- Garcia-Giron, A., Sola, D. and Peña, J. (2016), Liquid-assisted laser ablation of advanced ceramics and glass-ceramic materials, *Appl. Surf. Sci.* **363**, 548–554. 14, 94
- Gaudiuso, R., DellAglio, M., De Pascale, O., Senesi, G. S. and De Giacomo, A. (2010), Laser induced breakdown spectroscopy for elemental analysis in environmental, cultural heritage and space applications: A review of methods and results, *Sensors* **10**, 7434–7468. 4
- Gavrilović, M. R., Cvejić, M., Lazic, V. and Jovićević, S. (2016), Secondary plasma formation after single pulse laser ablation underwater and its advantages for laser induced breakdown spectroscopy (LIBS), *Phys. Chem. Chem. Phys.* **18**, 14629–14637. 40, 62, 98
- Gavrilović, M. R., Lazic, V. and Jovićević, S. (2017), Influence of the target material on secondary plasma formation underwater and its laser induced breakdown spectroscopy (LIBS) signal, *J. Anal. At. Spectrom.* **32**, 345–353. 40, 62, 94

- Geiger, M., Becker, W., Rebhan, T., Hutfless, J. and Lutz, N. (1996), Increase of efficiency for the xecl laser ablation of ceramics, *Appl. Surf. Sci.* **96–98**, 309–315. 96
- Gigosos, M. A., González, M. A. and Cardenoso, V. (2003), Computer simulated balmer-alpha, -beta and -gamma stark line profiles for non-equilibrium plasmas diagnostics, *Spectrochimica Acta Part B* **58**, 1489–1504. 85
- Gladush, G. G. and Smurov, I. (2011), *Physics of Laser Materials Processing*, Springer-Verlag Berlin Heidelberg. 14
- Gregorčič, P., Jezeršek, M. and Možina, J. (2012), Optodynamic energy-conversion efficiency during an er:yag-laser-pulse delivery into a liquid through different fiber-tip geometries, *J. Biomed. Opt.* **17**, 075006, 9pp. 21
- Gregorčič, P., Lukač, N., Možina, J. and Jezeršek, M. (2016), Synchronized delivery of er:yag-laser pulses into water studied by a laser beam transmission probe for enhanced endodontic treatment, *Appl. Phys. A* **122**, 459, 7pp. 71
- Gregorčič, P., Petkovšek, R. and Možina, J. (2007), Investigation of a cavitation bubble between a rigid boundary and a free surface, *J. Appl. Phys.* **102**, 094904, 8pp. 21, 71
- Gregorčič, P., Petkovšek, R., Možina, J. and Močnik, G. (2008), Measurements of cavitation bubble dynamics based on a beam-deflection probe, *Appl. Phys. A* **93**, 901–905. 71
- Griem, H. (1974), *Spectral line broadening by plasmas*, Academic Press, inc. (London) ltd. 42, 85, 87
- Griem, H. (2000), Stark broadening of the hydrogen balmer-a line in low and high density plasmas, *Contrib. Plasma Phys.* **40**, 46–56. 43
- Griem, H. R. (2001), Comment on highly nonlinear, sign-varying shift of hydrogen spectral lines in dense plasmas, *Phys. Rev. E* **64**, 058401, 2pp. 43
- Griem, H. R., Halenka, J. and Olchawa, W. (2005), Comparison of hydrogen balmer-alpha stark profiles measured at high electron densities with theoretical results, *J. Phys. B: At. Mol. Opt. Phys.* **38**, 975–1000. 43

- Guirado, S., Fortes, F., Lazic, V. and Laserna, J. (2012), Chemical analysis of archeological materials in submarine environments using laser-induced breakdown spectroscopy. on-site trials in the mediterranean sea, *Spectrochim. Acta Part B* **74–75**, 137–143. 15, 40
- Hahn, D. W. and Omenetto, N. (2010), Laser-induced breakdown spectroscopy (libs), part i: Review of basic diagnostics and plasmaparticle interactions:still-challenging issues within the analytical plasma community, *Appl. Spectrosc.* **64**, 335A–366A. 4
- Hahn, D. W. and Omenetto, N. (2012), Laser-induced breakdown spectroscopy (libs), part ii: Review of instrumental and methodological approaches to material analysis and applications to different fields, *Appl. Spectrosc.* **66**, 347–419. 4
- Halenka, J. (2004), Comment on highly nonlinear, sign-varying shift of hydrogen spectral lines in dense plasmas, *Phys. Rev. E* **69**, 028401, 3pp. 43
- Hammer, D. X., Jansen, E. D., Frenz, M., Noojin, G. D., Thomas, R. J., Noack, J., Vogel, A., Rockwell, B. A. and Welch, A. J. (1997), Shielding properties of laser-induced breakdown in water for pulse durations from 5 ns to 125 fs, *Appl. Opt.* **36**, 5630–5640. 12
- Harilal, S. S., Bindhu, C. V., Tillack, M. S., Najmabadi, F., and Gaeris, A. C. (2003), Internal structure and expansion dynamics of laser ablation plumes into ambient gases, *J. Appl. Phys.* **93**, 2380–2388. 4
- Harilal, S. S., Bindhu, C. V., Tillack, M. S., Najmabadi, F. and Gaeris, A. C. (2002), Plume splitting and sharpening in laser-produced aluminium plasma, *J. Phys. D: Appl. Phys.* **35**, 2935–2938. 4
- Harilal, S. S., OShay, B., Tao, Y. and Tillack, M. S. (2006), Ambient gas effects on the dynamics of laser-produced tin plume expansion, *J. Appl. Phys.* **99**, 083303, 10 pp. 3
- He, H., Li, W., Zhang, X., Xia, M. and Yang, K. (2012), Light scattering by a spheroidal bubble with geometrical optics approximation, *J. Quant. Spectrosc. Radiat. Transfer.* **113**, 1467–1475. 31

- Heisterkamp, A., Ripken, T., Mamom, T., Drommer, W., Welling, H., Ertmer, W. and Lubatschowski, H. (2002), Nonlinear side effects of fs pulses inside corneal tissue during photodisruption, *Appl. Phys. B* **74**, 419–425. 12
- Holt, R. G. and Crum, L. A. (1990), Mie scattering used to determine spherical bubble oscillations, *Appl. Opt.* **29**, 4182–4191. 30
- Hooper Jr, C. (1968), Low-frequency component electric microfield distribution in plasmas, *Phys. Rev.* **165**, 215–222. 86
- Hopp, B., Smausz, T., T.Wittmann and Ignácz, F. (2000), Comparative time-resolved study of solid-state and liquid ablation of polyethylene-glycol 1000: temperature, viscosity and surface tension dependence, *Appl. Phys. A* **71**, 315–318. 14
- Huber, P., Jöchle, K. and Debus, J. (1998), Influence of shock wave pressure amplitude and pulse repetition frequency on the lifespan, size and number of transient cavities in the field of an electromagnetic lithotripter, *Phys. Med. Biol.* **43**, 3113–3128. 26, 30
- Hutson, M. S. and Ma, X. (2007), Plasma and cavitation dynamics during pulsed laser microsurgery in vivo, *Phys. Rev. Lett.* **99**, 158104, 4pp. 13
- Hwang, Z.-W., Teng, Y.-Y., Li, K.-P. and Sneddon, J. (1991), Interaction of a laser beam with metals. part i: Quantitative studies of plasma emission, *Appl. Spectrosc.* **45**, 435–441. 3
- Ibrahimkutty, S., Wagener, P., dos Santos Rolo, T., Karpov, D., Menzel, A., Baumbach, T., Barcikowski, S. and Plech, A. (2015), A hierarchical view on material formation during pulsed-laser synthesis of nanoparticles in liquid, *Sci. Rep.* **5**, 16313, 11pp. 5, 13, 27, 69
- Ibrahimkutty, S., Wagener, P., Menzel, A., Plech, A. and Barcikowski, S. (2012), Nanoparticle formation in a cavitation bubble after pulsed laser ablation in liquid studied with high time resolution small angle x-ray scattering, *Appl. Phys. Lett.* **101**, 103104, 4pp. 21, 27
- Isselin, J.-C., Alloncle, A.-P., and Autric, M. (1998), On laser induced single bubble near a solid boundary: Contribution to the understanding of erosion phenomena, *J. Appl. Phys.* **84**, 5766–5771. 2

- Jomni, F., Denat, A. and Aitken, F. (2009), The dynamics of microscopic bubbles in viscous insulating liquids, *J. Appl. Phys.* **105**, 053301, 9pp. 3
- Kannatey-Asibu, E. (2009), *Principles of laser materials processing*, John Wiley & Sons, Inc. 14
- Kennedy, P., Hammer, D. and Rockwell, B. (1997), Laser induced breakdown in aqueous media, *Prog. Quant. Electr.* **21**, 155–248. 12, 30, 32, 33, 44, 61, 78, 82
- Kennedy, P. K. (1995), A first-order model for computation of laser-induced breakdown thresholds in ocular and aqueous media: Part i-theory, *IEEE J. Quantum Electron* **31**, 2241–2249. 1, 34, 35
- Kennedy, P. K., Boppart, S. A., Hammer, D. X., Rockwell, B. A., Noojin, G. D. and Roach, W. P. (1995), A first-order model for computation of laser-induced breakdown thresholds in ocular and aqueous media: Part ii-comparison to experiments, *IEEE J. Quantum Electron* **31**, 2250–2257. 1
- Kielkopf, J. F. (1995), Spectroscopic study of laser-produced plasmas in hydrogen, *Phys. Rev. E* **52**, 2013–2024. 43
- Kielkopf, J. F. (2000), Laser-produced plasma bubble, *Phys. Rev. E* **63**, 016411, 6pp. 5
- Kielkopf, J. F. and Allard, N. F. (2014), Shift and width of the balmer series ha line at high electron density in a laser-produced plasma, *J. Phys. B: At. Mol. Opt. Phys.* **747**, 155701, 6pp. 43
- Kim, K. K., Roy, M., Kwon, H., Song, J. K. and Park, S. M. (2015), Laser ablation dynamics in liquid phase: The effects of magnetic field and electrolyte, *J. Appl. Phys.* **117**, 074302, 7pp. 55
- Koch, S. (2012), *Qualitative and quantitative trace analysis on liquids and solid samples by laser-induced breakdown spectroscopy (LIBS)*, Von der Fakultät für Mathematik und Naturwissenschaften der Carl von Ossietzky Universität Oldenburg, Dissertation. 41
- Koch, S., Garen, W., Hegedüs, F., Neu, W., Reuter, R. and Teubner, U. (2012), Time-resolved measurements of shock-induced cavitation bubbles in liquids, *Appl. Phys. B* **108**, 345–351. 71

- Koch, S., Garen, W., Müller, M. and Neu, W. (2004), Detection of chromium in liquids by laser induced breakdown spectroscopy (libs), *Appl. Phys. A* **79**, 1071–1073. 15
- Kohsakowski, S., Gökce, B., Tanabe, R., Wagener, P., Plech, A., Ito, Y. and Barcikowski, S. (2016), Target geometry and rigidity determines laser-induced cavitation bubble transport and nanoparticle productivity a high-speed videography study, *Phys.Chem.Chem.Phys.* **18**, 16585–16593. 14
- Konjević, N. (1999), Plasma broadening and shifting of non-hydrogenic spectral lines: present status and applications, *Phys. Rep.* **316**, 339–401. 86
- Konjević, N., Ivković, M. and Jovićević, S. (2010), Spectroscopic diagnostics of laser-induced plasmas, *Spectrochim. Acta Part B* **65**, 593–602. 4
- Konjević, N., Ivković, M. and Sakan, N. (2012), Hydrogen balmer lines for low electron number density plasma diagnostics, *Spectrochim. Acta Part B* **62** **76**, 16–26. 83, 84
- Koren, G. (1987), Observation of shock waves and cooling waves in the laser ablation of kapton films in air, *Appl. Phys. Lett.* **51**, 569–571. 70
- Kou, L., Labrie, D. and Chylek, P. (1993), Refractive indices of water and ice in the 0.65– to 2.5- μm spectral range, *Appl. Opt.* **32**, 3531–3540. 46
- Kovalchuk, T., Toker, G., Bulatov, V. and Schechter, I. (2010), Laser breakdown in alcohols and water induced by $\lambda = 1064$ nm nanosecond pulses, *Chem. Phys. Lett.* **500**, 242–250. 3, 36
- Kramida, A., Yu. Ralchenko and NIST ASD Team, J. R. (2015), NIST Atomic Spectra Database (ver. 5.3), [Online]. Available: <http://physics.nist.gov/asd> [2017, February 28]. National Institute of Standards and Technology, Gaithersburg, MD. 85
- Krieger, J. R. and Chahine, G. L. (2005), Acoustic signals of underwater explosions near surfaces, *J. Acoust. Soc. Am.* **118**, 2961–2974. 3
- Krstulović, N., Shannon, S., Stefanuik, R. and Fanara, C. (2013), Underwater-laser drilling of aluminum, *Int. J. Adv. Manuf. Technol.* **69**, 1765–1773. 15

- Kruusing, A. (2004a), Underwater and water-assisted laser processing: Part 1 general features, steam cleaning and shock processing, *Optics and Lasers in Engineering* **41**, 307–327. 14
- Kruusing, A. (2004b), Underwater and water-assisted laser processing: Part 2 etching, cutting and rarely used methods, *Optics and Lasers in Engineering* **41**, 329–352. 14
- Kruusing, A. (2008), *Handbook of Liquids-Assisted Laser Processing*, Elsevier Ltd. 14
- Kumar, B. and Thareja, R. K. (2010), Synthesis of nanoparticles in laser ablation of aluminum in liquid, *J. Appl. Phys.* **108**, 064906, 6pp. 42, 82
- Lam, J. (2015), *Pulsed laser ablation in liquid: towards the comprehension of the growth processes*, These de l'Universite de Lyon. 27, 83
- Lam, J., Amans, D., Chaput, F., Diouf, M., Ledoux, G., Mary, N., Masenelli-Varlot, K., Motto-Ros, V. and Dujardin, C. (2014), γ - Al_2O_3 nanoparticles synthesised by pulsed laser ablation in liquids: a plasma analysis, *Phys. Chem. Chem. Phys.* **16**, 963–973. 3, 42, 56, 58
- Lam, J., Lombard, J., Dujardin, C., Ledoux, G., Merabia, S. and Amans, D. (2016), Dynamical study of bubble expansion following laser ablation in liquids, *Appl. Phys. Lett.* **108**, 074104, 5pp. 13, 42
- Langley, D. S. and Marston, P. L. (1991), Forward glory scattering from bubbles, *Appl. Opt.* **630**, 3452–3458. 29, 65
- Lazic, V., Colao, F., Fantoni, R. and Spizzicchino, V. (2005), Recognition of archaeological materials underwater by laser induced breakdown spectroscopy, *Spectrochim. Acta Part B* **60**, 1014–1024. 15
- Lazic, V., Colao, F., Fantoni, R., Spizzicchino, V. and Jovićević, S. (2007), Underwater sediment analyses by laser induced breakdown spectroscopy and calibration procedure for fluctuating plasma parameters, *Spectrochim. Acta Part B* **62**, 30–39. 15
- Lazic, V. and Jovićević, S. (2014), Laser induced breakdown spectroscopy inside liquids: Processes and analytical aspects, *Spectrochim. Acta, Part B* **104**, 288–311. 10, 11, 29, 40, 42, 46, 58

- Lazic, V., Jovicevic, S. and Carpanese, M. (2012), Laser induced bubbles inside liquids: Transient optical properties and effects on a beam propagation, *Appl. Phys. Lett.* **101**, 054101, 4pp. 29, 65, 66, 67
- Lazic, V., Jovievic, S., Fantoni, R. and Colao, F. (2007), Efficient plasma and bubble generation underwater by an optimized laser excitation and its application for liquid analyses by laser-induced breakdown spectroscopy, *Spectrochim. Acta Part B* **62**, 1433–1442. 26, 31
- Lazic, V., Laserna, J. and Jovicevic, S. (2013a), Insights in the laser-induced breakdown spectroscopy signal generation underwater using dual pulse excitation part i: Vapor bubble, shockwaves and plasma, *Spectrochim. Acta Part B* **82**, 42–49. 5, 27, 40, 56, 58, 65, 93
- Lazic, V., Laserna, J. and Jovicevic, S. (2013b), Insights in the laser induced breakdown spectroscopy signal generation underwater using dual pulse excitation part ii: Plasma emission intensity as a function of interpulse delay, *Spectrochim. Acta Part B* **82**, 50–59. 27, 73
- Lentz, W. J., Atchley, A. A. and Gaitan, D. F. (1995), Mie scattering from a sonoluminescing air bubble in water, *Appl. Opt.* **34**, 2648–2654. 30, 75
- Lo, K. M. and Cheung, N. H. (2002), Arf laser-induced plasma spectroscopy for part-per-billion analysis of metal ions in aqueous solutions, *Appl. Spect.* **56**, 682–688. 82
- Margulis, M. A. and Margulis, I. M. (2006), Luminescence mechanism of acoustic and laser-induced cavitation, *Acoust. Phys.* **52**, 283–292. 3, 21
- Martí-López, L., Ocaña, R., Piñeiro, E. and Asensio, A. (2011), Laser peening induced shock waves and cavitation bubbles in water studied by optical schlieren visualization, *Physics Procedia* **12**, 442–451. 15, 19
- Matsumoto, A., Tamura, A., Fukami, K., Ogata, Y. H. and Sakka, T. (2013a), Single-pulse underwater laser-induced breakdown spectroscopy with nongated detection scheme, *Anal. Chem.* **85**, 3807–3811. 16, 62, 93
- Matsumoto, A., Tamura, A., Fukami, K., Ogata, Y. H. and Sakka, T. (2013b), Two-dimensional space-resolved emission spectroscopy of laser ablation plasma in water, *J. Appl. Phys.* **113**, 053302, 7pp. 62

- Matsumoto, A., Tamura, A., Kawasaki, A., Honda, T., Gregorčič, P., ichi Amano, N. N. K., Fukami, K. and Sakka, T. (2016), Comparison of the overall temporal behavior of the bubbles produced by short- and long-pulse nanosecond laser ablations in water using a laser-beam-transmission probe, *Appl. Phys. A* **122**, 234, 6pp. 71, 72
- Matula, T. J., Hilmo, P. R., Storey, B. D. and Szeri, A. J. (2002), Radial response of individual bubbles subjected to shock wave lithotripsy pulses *in vitro*, *Phys. Fluids* **14**, 913–921. 21, 31
- Mätzler, C. (2002), *MATLAB Functions for Mie Scattering and Absorption*, IAP Res. Rep. No. 02-08,. 31
- McK. Ellison, J. and Peetz, C. V. (1959), The forward scattering of light by spheres according to geometrical optics, *Proc. Phys. Soc.* **74**, 105–123. 31
- Menéndez-Manjón, A., Wagener, P. and Barcikowski, S. (2011), Transfer-matrix method for efficient ablation by pulsed laser ablation and nanoparticle generation in liquids, *J. Phys. Chem. C* **115**, 5108–5114. 13
- Michel, A. P. M. and Chave, A. D. (2008), Double pulse laser-induced breakdown spectroscopy of bulk aqueous solutions at oceanic pressures: interrelationship of gate delay, pulse energies, interpulse delay, and pressure, *Appl. Opt.* **47**, G131–G143. 5, 15
- Mie, G. (1908), Beiträge zur optik trüber medien, speziell kolloidaler metallösungen, *Annalen der physik* **330**, 377–445. 30
- Miziolek, A., Palleschi, V. and Schechter, I. (2006), *Laser-Induced Breakdown Spectroscopy (LIBS)*, Cambridge University Press. 4
- Musazzi, S. and Perini, U. (2014), *Laser-Induced Breakdown Spectroscopy - Theory and Applications*, Springer-Verlag Berlin Heidelberg. 4, 10, 38, 91
- Muñoz, M. P., Luengo, M. C. L., Llorente, J. M. S., Sánchez, M. P., García, A. A. . A. and Pedraz, P. M. (2010), Morphological alterations in dentine after mechanical treatment and ultrashort pulse laser irradiation, *Lasers Med. Sci.* **27**, 53–58. 12
- Nath, A. and Khare, A. (2008), Measurement of charged particles and cavitation bubble expansion velocities in laser induced breakdown in water, *Laser Part. Beams* **26**, 425–432. 71

- Nath, A. and Khare, A. (2011), Transient evolution of multiple bubbles in laser induced breakdown in water, *Laser Part. Beams* **29**, 1–9. 21, 71
- Nguyen, T. T. P., Tanabe, R. and Ito, Y. (2013), Influences of focusing conditions on dynamics of laser ablation at a solid-liquid interface, *Appl. Phys. Express* **6**, 122701(4pp). 38, 45
- Niemz, M. H. (2004,2007), *Laser-Tissue Interactions, Fundamentals and Applications*, Springer-Verlag Berlin Heidelberg. 1, 2, 7, 8, 9, 11, 12, 13
- Noack, J., Hammer, D. X., Noojin, G. D., Rockwell, B. A. and Vogel, A. (1998), Influence of pulse duration on mechanical effects after laser-induced breakdown in water, *J. Appl. Phys.* **83**, 7488–7495. 20
- Noll, R. (2012), *Laser-Induced Breakdown Spectroscopy - Fundamentals and applications*, Springer-Verlag Berlin Heidelberg. 4, 37, 39, 91
- Nuzzo, V., Savoldelli, M., Legeais, J.-M. and Plamann, K. (2010), Self-focusing and spherical aberrations in corneal tissue during photodisruption by femtosecond laser, *Journal of Biomedical Optics* **15**, 038003, 8pp. 12
- Nyga, R. and Neu, W. (1993), Double-pulse technique for optical emission spectroscopy of ablation plasmas of samples in liquids, *Opt. Lett.* **18**, 747–749. 5
- Oguchi, H., Sakka, T. and Ogata, Y. H. (2007), Effects of pulse duration upon the plume formation by the laser ablation of cu in water, *J. Appl. Phys.* **102**, 023306, 6pp. 56, 58, 62
- Ohata, M., Iwasaki, Y., Furuta, N. and Brenner, I. B. (2002), Studies on laser defocusing effects on laser ablation inductively coupled plasma-atomic emission spectrometry using emission signals from a laser-induced plasma, *Spectrochim. Acta Part B* **57**, 1713–1725. 3
- Ohl, C.-D., Kurz, T., Geisler, R., Lindau, O. and Lauterborn, W. (1999), Bubble dynamics, shock waves and sonoluminescence, *Phil. Trans. R. Soc. Lond. A* **357**, 269–294. 21, 28
- Ornstein, L. S. and Brinkman, H. (1931), Temperature determination from band-spectra. i. vibrational energy distribution and vibrational transition probabilities in the cyanogen $^2 \sum - ^2 \sum$ bandsystem., *Communication from the Physical Institute of the University of Utrecht* pp. -. 88

- Parigger, C., Woods, A., Surmick, D., Gautam, G., Witte, M. and Hornkohl, J. (2015), Computation of diatomic molecular spectra for selected transitions of aluminum monoxide, cyanide, diatomic carbon, and titanium monoxide, *Spectrochim. Acta, Part B* **107**, 132–138. 87, 88
- Peel, C. S., Fang, X. and Ahmad, S. R. (2011), Dynamics of laser-induced cavitation in liquid, *Appl Phys A* **103**, 1131–1138. 21
- Peter Schaaf, e. (2010), *Laser Processing of Materials Fundamentals, Applications and Developments*, Springer-Verlag Berlin Heidelberg. 14
- Petkovšek, R. and Gregorčič, P. (2007), A laser probe measurement of cavitation bubble dynamics improved by shock wave detection and compared to shadow photography, *J. Appl. Phys.* **102**, 044909, 9pp. 71
- Petkovšek, R., Gregorčič, P. and Možina, J. (2007), A beam-deflection probe as a method for optodynamic measurements of cavitation bubble oscillations, *Meas. Sci. Technol.* **18**, 2972–2978. 21
- Peyre, P., Berthe, L., Scherpereel, X. and Fabbro, R. (1998), Laser-shock processing of aluminium-coated 55c1 steel in water-confinement regime, characterization and application to high-cycle fatigue behaviour, *J. Mater. Sci.* **33**, 1421–1429. 15
- Pichahchy, A., Cremers, D. and Ferris, M. (1997), Elemental analysis of metals under water using laser-induced breakdown spectroscopy, *Spectrochim. Acta Part B* **52**, 25–39. 15
- Plesset, M. (1949), The dynamics of cavitation bubbles, *J. Appl. Mech.* **16**, 277–282, 21
- Plesset, M. S. and Prosperetti, A. (1977), Bubble dynamics and cavitation, *Ann. Rev. Fluid. Mech.* **9**, 145–185, 21
- Povarnitsyn, M. E., Itina, T. E., Levashov, P. R. and Khishchenko, K. V. (2013), Mechanisms of nanoparticle formation by ultra-short laser ablation of metals in liquid environment, *Phys.Chem. Chem. Phys.* **15**, 3108–3114. 13
- Pu, X. Y. and Cheung, N. H. (2003), Arf laser induced plasma spectroscopy of lead ions in aqueous solutions: Plume reheating with a second nd : Yag laser pulse, *Appl. Spectrosc.* **57**, 588–590. 5

- Rai, N. K. and Rai, A. (2008), Libsan efficient approach for the determination of cr in industrial wastewater, *J. Hazard. Mater.* **150**, 835–838. 15
- Rayleigh, L. (1917), The pressure developed in a liquid during the collapse of a spherical cavity, *Philos. Mag.* **34**, 94–98,. 2, 21
- Reich, S., Schönfeld, P., Wagener, P., Letzel, A., Ibrahimkutty, S., Gökce, B., Barcikowski, S., Menzel, A., dos Santos Rolo, T. and Plech, A. (2017), Pulsed laser ablation in liquids: Impact of the bubble dynamics on particle formation, *J. Coll. Int. Sci.* **489**, 106–113. 13
- Rekhi, S., Tempere, J. and Silvera, I. F. (2003), Temperature determination for nanosecond pulsed laser heating, *Rev. Sci. Instrum.* **74**, 3820–3825. 80
- Saito, K., Takatani, K., Sakka, T. and Ogata, Y. H. (2002), Observation of the light emitting region produced by pulsed laser irradiation to a solidliquid interface, *Appl. Surf. Sci.* **197–198**, 56–60. 55
- Sakka, T., Oguchi, H., Masai, S., Hirata, K., Ogata, Y. H., Saeki, M. and Ohba, H. (2006), Use of a long-duration ns pulse for efficient emission of spectral lines from the laser ablation plume in water, *Appl. Phys. Lett.* **88**, 061120, 3pp. 16
- Sakka, T., Saito, K. and Ogata, Y. H. (2005), Confinement effect of laser ablation plume in liquids probed by self-absorption of c2 swan band emission, *J. Appl. Phys.* **97**, 014902,4pp. 42
- Sakka, T., Takatani, K., Ogata, Y. H. and Mabuchi, M. (2002), Laser ablation at the solidliquid interface: transient absorption of continuous spectral emission by ablated aluminium atoms, *J. Phys. D: Appl. Phys.* **35**, 65–73. 55
- Sakka, T., Tamura, A., Matsumoto, A., Fukami, K., Nishi, N. and Thornton, B. (2014), Effects of pulse width on nascent laser-induced bubbles for underwater laser-induced breakdown spectroscopy, *Spectrochim. Acta Part B 97 (2014) 9498* **97**, 94–98. 21
- Sakka, T., Tamura, A., Nakajima, T., Fukami, K. and Ogata, Y. H. (2012), Synergetic effects of double laser pulses for the formation of mild plasma in water: Toward non-gated underwater laser-induced breakdown spectroscopy, *J. Chem. Phys.* **136**, 174201, 5pp. 27

- Salminen, T. (2013), *Production of Nanomaterials by Pulsed Laser Ablation*, Thesis, Tampere University of Technology, Publication 1121. 13
- Samant, A. N. and Dahotre, N. B. (2009), Laser machining of structural ceramics – a review, *J. Eur. Cer. Soc.* **29**, 969993. 94
- Sasaki, K., Nakano, T., Soliman, W. and Takada, N. (2009), Effect of pressurization on the dynamics of a cavitation bubble induced by liquid-phase laser ablation, *Appl. Phys. Express* **2**, 046501, 3pp. 70, 98
- Sasaki, K. and Takada, N. (2010), Liquid-phase laser ablation, *Pure Appl. Chem.* **82**, 1317–1327. 5, 13
- Sell, J. A., Heffelfinger, D. M., Ventzek, P. and Gilgenbach, R. M. (1989), Laser beam deflection as a probe of laser ablation of materials, *Appl. Phys. Lett.* **55**, 2435–2437. 70
- Settles, G. (2006), *Schlieren and Shadowgraph techniques: Visualizing Phenomena in transparent media*, Springer-Verlag Berlin Heidelberg. 47, 48
- Shangguan, H., Casperson, L. W., Paisley, D. L. and Prahl, S. A. (1998), Photographic studies of laser-induced bubble formation in absorbing liquids and on submerged targets: implications for drug delivery with microsecond laser pulses, *Opt. Eng.* **37**, 2217–2226,. 13
- Shangguan, H., Casperson, L. W., Shearin, A., Paisley, D. L. and Prahl, S. A. (1997), Effects of material properties on laser-induced bubble formation in absorbing liquids and on submerged targets, *Proc. SPIE* **2869**, 783–791. 1
- Shen, Y. R. (1984), *The Principles of Nonlinear Optics*, John Wiley and Sons, New York. 35
- Shockley, W. (1961), Problems related to p - n junction, *Solid-State Electron.* **2**, 35–67. 33
- Singh, J. P. and Thakur, S. N. (2007), *Laser-Induced Breakdown Spectroscopy*, Elsevier B.V. 4
- Sola, X., Ignatiev, M., Flamant, G., Smurov, I. and Konstantinov, S. (1997), Monitoring of melting and solid state phase transformation induced by pulsed laser action on pure zirconium, *Appl. Surf. Sci.* **109–110**, 106–112. 96

- Soliman, W., Takada, N. and Sasaki, K. (2010), Growth processes of nanoparticles in liquid-phase laser ablation studied by laser-light scattering, *Appl. Phys. Express* **3**, 035201, 3pp. 13, 63, 70
- Sriramachandran, P., Viswanathan, B. and Shanmugavel, R. (2013), Occurrence of atomic molecular lines in sunspot umbral spectra, *Solar Phys.* **286**, 315–326. 88
- Stambulchik, E., Fisher, D., Maron, Y., Griem, H. and Alexiou, S. (2007), Correlation effects and their influence on line broadening in plasmas: Application to h_{α} , *High Energy Density Phys.* **3**, 272–277. 42, 43
- Stehle, C., Caillol, J., Escarguel, A. and Gilles, D. (2000), Hydrogen lines in correlated plasmas, *J. Phys. IV France* **10**, 501–504. 43, 86
- Suzuki, H., Nishikawa, H. and Sandy Lee, I.-Y. (2002), Laser-induced breakdown spectroscopy at metal-water interfaces, *Phys. Chem. Comm.* **5**, 88–90. 41, 79, 93
- Tagawa, Y., Yamamoto, S., Hayasaka, K. and Kameda, M. (2016), On pressure impulse of a laser-induced underwater shock wave, *J. Fluid Mech.* **808**, 5–18. 19
- Takada, N., Nakano, T. and Sasaki, K. (2010), Formation of cavitation-induced pits on target surface in liquid-phase laser ablation, *Appl. Phys. A* **101**, 255–258. 2, 29, 40
- Tamura, A., Matsumoto, A., Fukami, K., Nishi, N. and Sakka, T. (2015), Simultaneous observation of nascent plasma and bubble induced by laser ablation in water with various pulse durations, *J. Appl. Phys.* **117**, 173304, 8pp. 6
- Tao, S., Zhou, Y., Wu, B. and Gao, Y. (2012), Infrared long nanosecond laser pulse ablation of silicon: Integrated two-dimensional modeling and time-resolved experimental study, *Appl. Surf. Sci.* **258**, 7766–7773. 58, 61
- Thornton, B., Sakka, T., Takahashi, T., Tamura, A., Masamura, T. and Matsumoto, A. (2013), Spectroscopic measurements of solids immersed in water at high pressure using a long-duration nanosecond laser pulse, *Appl. Phys. Express* **6**, 082401, 4pp. 70, 98
- Thornton, B., Takahashi, T., Sato, T., Sakka, T., Tamura, A., Matsumoto, A., Nozaki, T., Ohki, T. and Ohki, K. (2015), Development of a deep-sea laser-induced breakdown spectrometer for in situ multi-element chemical analysis, *Deep Sea Res. Part I* **95**, 20–36. 16

- Thornton, B. and Ura, T. (2011), Effects of pressure on the optical emissions observed from solids immersed in water using a single pulse laser, *Appl. Phys. Express* **4**, 022702, 3pp. 56
- Tian, Y., Xue, B., Jiaojian Song, Y. L. and Zheng, R. (2015), Non-gated laser-induced breakdown spectroscopy in bulk water by position-selective detection, *Appl. Phys. Lett.* **107**, 111107, 5pp. 37
- Tian, Y., Xue, B., Song, J., Lu, Y. and Zheng, R. (2016), Stabilization of laser-induced plasma in bulk water using large focusing angle, *Appl. Phys. Lett.* **109**, 061104, 5 pp. 37
- Tiwari, D., Bellouard, Y., Dietzela, A., Ren, M., Rubingh, E. and Meinders, E. (2010), Dynamical observation of femtosecond-laser-induced bubbles in water using a single laser source for probing and sensing, *Appl. Phys. Express* **3**, 127101, 3pp. 65
- Toker, G., Bulatov, V., Kovalchuk, T. and Schechter, I. (2009), Micro-dynamics of optical breakdown in water induced by nanosecond laser pulses of 1064 nm wavelength, *Chem. Phys. Lett.* **471**, 244–248. 36, 37
- Tomita, Y. and Kodama, T. (2003), Interaction of laser-induced cavitation bubbles with composite surfaces, *J. Appl. Phys.* **94**, 2809–2816. 21
- Totten, G. E. and MacKenzie, D. S. (2003), *Handbook of Aluminum, Volume 1, Physical Metallurgy and Processes*, Marcel Dekker, Inc. 94
- Tsai, C.-H. and Li, C.-C. (2009), Investigation of underwater laser drilling for brittle substrates, *Journal of materials processing technology* **209**, 2838–2846. 15
- T. Tsuji, Okazaki, Y., Tsuboi, Y. and Tsuji, M. (2007), Nanosecond time-resolved observations of laser ablation of silver in water, *Jpn. J. Appl. Phys.* **46**, 1533–1535. 19, 20, 55, 63, 78
- Ushida, H., Takada, N. and Sasaki, K. (2007), Diagnostics of liquid-phase laser ablation plasmas by spectroscopic methods, *J. Phys.: Conf. Ser.* **59**, 563–566. 41, 79
- Vadim A Petrov, A. Y. V. (2007), Spectral emissivity and radiance temperature plateau of self-supporting Al_2O_3 melt at rapid solidification, *High Temperatures-High Pressures* **35/36**, 321–329. 96

- Vasil'ev, L. (1971), *Schlieren methods*, Israel Program for Scientific translation. 48
- Venugopal Rao, S., Podagatlapalli, G. K. and Hamad, S. (2014), Ultrafast laser ablation in liquids for nanomaterials and applications, *Journal of Nanoscience and Nanotechnology* **14**, 1–25. 13
- Vitel, Y., Bezzari, M. E., Gavrilova, T., Skowronek, M., D'yachkov, L. and Kurilenkov, Y. (1996), Shift and width of the h_{α} line of hydrogen in dense plasmas, *Physica B* **228**, 161–165. 43
- Vogel, A. (1997), Nonlinear absorption: intraocular microsurgery and laser lithotripsy, *Phys. Med. Biol.* **42**, 895–912. 12
- Vogel, A. (1998), *Optical Breakdown in Water and Ocular Media, and its Use for Intraocular Photodisruption*, Habilitation dissertation, Medical University of Lübeck, Germany. 1, 17, 19
- Vogel, A., Busch, S. and Parlitz, U. (1996), Shock wave emission and cavitation bubble generation by picosecond and nanosecond optical breakdown in water, *J. Acoust. Soc. Am.* **100**, 148–165. 12, 19
- Vogel, A. and Lauterborn, W. (1988), Acoustic transient generation by laser-produced cavitation bubbles near solid boundaries, *J. Acoust. Soc. Am.* **84**, 719–731. 19
- Vogel, A., Lauterborn, W. and Timm, R. (1989), Optical and acoustic investigations of the dynamics of laser-produced cavitation bubbles near a solid boundary, *J. Fluid Meh.* **206**, 299–338. 2, 21, 26, 28
- Vogel, A., Noack, J., Nahen, K., Theisen, D., Busch, S., Parlitz, U., Hammer, D., Noojin, G., Rockwell, B. and R. Birngruber (1999), Energy balance of optical breakdown in water at nanosecond to femtosecond time scales, *Appl. Phys. B* **68**, 271–280. 78
- Vogel, A., Schweiger, P., Frieser, A., Asiyo, M. N. and Birngruber, R. (1990), Intraocular nd:yag laser surgery: light-tissue interaction, damage range, and reduction of collateral effects, *IEEE J. Quant. Electron.* **26**, 2240–2260. 12
- Vogel, A. and Venugopalan, V. (2003), Mechanisms of pulsed laser ablation of biological tissues, *Chem. Rev.* **103**, 577–644. 1, 12, 28

- Wagener, P., Ibrahimkuty, S., Menzel, A., Plech, A. and Barcikowski, S. (2013), Dynamics of silver nanoparticle formation and agglomeration inside the cavitation bubble after pulsed laser ablation in liquid, *Phys. Chem. Chem. Phys.* **15**, 3068–3074. 13, 63
- Wallace, J. M. and Hobbs, P. V. (2006), *Atmospheric Science, An Introductory Survey*, Elsevier Inc. 30
- Wen, S.-B., Mao, X., Greif, R. and Russo, R. E. (2007*a*), Expansion of the laser ablation vapor plume into a background gas.i. analysis, *J. Appl. Phys.* **101**, 023114, 13pp. 4
- Wen, S.-B., Mao, X., Greif, R. and Russo, R. E. (2007*b*), Laser ablation induced vapor plume expansion into a background gas. ii. experimental analysis, *J. Appl. Phys.* **101**, 023115, 14pp. 4
- Williams, F., Varma, S. P. and Hillenius, S. (1976), Liquid water as a lone-pair amorphous semiconductor, *J. Chem. Phys.* **64**, 1549–1554. 34
- Wiscombe, W. J. (1980), Improved mie scattering algorithms, *Appl. Opt.* **19**, 1505–1509. 31
- Wook Kang—, H., Lee, H. and Welch, A. J. (2008), Laser ablation in a liquid-confined environment using a nanosecond laser pulse, *J. Appl. Phys.* **103**, 083101, 6pp. 14, 41
- Yang, G. (2012), *Laser ablation in liquids, Principles and applications in the preparation of the nanomaterials*, Pan Stanford Publishing. 5, 13
- Yu, H., Shen, J. and Wei, Y. (2008), Geometrical optics approximation of light scattering by large air bubbles, *Particuology* **6**, 340–346. 30, 31
- Yueh, F.-Y., Sharma, R. C., Singh, J. P. and Zhang, H. (2002), Evaluation of laser-induced breakdown spectroscopy as technetium monitor, *J. Air Waste Manag. Assoc.* **52**, 1307–1315. 15
- Zel'dovich, Y. B., Raizer, Y. P., Hayes, W. D. and Probstein, R. F. (1966), *Physics of shock waves and high-temperature phenomena*, Academic press Inc. 17

- Zeng, H., Du, X.-W., Singh, S. C., Kulinich, S., Yang, S., He, J. and Cai, W. (2012), Nanomaterials via laser ablation/irradiation in liquid: A review, *Adv. Funct. Mater.* **22**, 1333–1353. 13
- Zhang, Z. and Modest, M. F. (1998), Temperature-dependent absorptances of ceramics for nd:yag and co2 laser processing applications, *J. Heat Transfer* **120**, 322–327. 96
- Zhong, P., Zhou, Y. and Zhu, S. (2001), Dynamics of bubble oscillation in constrained media and mechanisms of vessel rupture in swl, *Ultrasound Med. Biol.* **27**, 119–134. 2
- Zhou, Y., Tao, S. and Wu, B. (2011), Backward growth of plasma induced by long nanosecond laser pulse ablation, *Appl. Phys. Lett.* **99**, 051106, 3pp. 58, 61
- Zhu, S., Lu, Y. F., Hong, M. H. and Chen, X. Y. (2001), Laser ablation of solid substrates in water and ambient air, *J. Appl. Phys.* **89**, 2400–2403. 14

Biography

Marijana Gavrilović was born 12.06.1986 in Kragujevac. After graduating from the I Gymnasium in Kragujevac in 2005, she enrolled in the School of Electrical Engineering at the University of Belgrade. She graduated from the Department of Physical Electronics in 2009, with the GPA of 8.36 (out of 10.00). In 2011 she received her master degree from the Department of Physical Electronics of the School of Electrical Engineering. She entered the Nanoelectronics and Photonics Ph.D. program at the same university in 2011. She is currently at the third year of the Ph.D. program and she passed all the exams successfully

M. R. Gavrilović has been working as a research assistant in the Laboratory for the Plasma Spectroscopy and Lasers in Photonics Center at the Institute of Physics Belgrade since 2011, participating in the national research project “Spectroscopic diagnostics of low temperature plasma and gas discharges: spectral line shapes and interaction with surfaces” (OI171014).

She participated in bilateral project with France Pavle Savić (680-00-132/2012-09/03, (2012-2014)) and Slovakia (451-03-545/2015-09/12, 2015-2016).

She was one of the chosen candidates for the participation in conference and school at the International Center for Theoretical Physics (ICTP) in Trieste, organized jointly by the ICTP and IAEA (International Atomic Energy Agency) under the title “Modern methods in plasma spectroscopy”

As a guest researcher, she visited the laboratories of the Photonics Department at the Jagiellonian University, where she was involved in the experimental studies of laser induced plasma by Thomson scattering and optical emission spectroscopy.

The most important research results of the Ph.D. candidate Marijana R. Gavrilović are summarized in seven articles published in international journals. —————

List of publications

1. M. R. Gavrilović and M. Cvejić and V. Lazic and S. Jovićević, Secondary plasma formation after single pulse laser ablation underwater and its advantages for laser induced breakdown spectroscopy (LIBS), *Phys. Chem. Chem. Phys.* **18** 14629–14637 (2016) (ISSN: 1463-9076 doi: 10.1039/C6CP01515H Impact factor: 4.449)
2. M. R. Gavrilović and V. Lazic and S. Jovićević, Influence of the target material on secondary plasma formation underwater and its laser induced breakdown spectroscopy (LIBS) signal, *J. Anal. At. Spectrom.* **32** 345–353 (2017) (ISSN 0267-9477 DOI: 10.1039/c6ja00300a, Impact factor: 3.379)
3. M. Cvejić and M.R. Gavrilović and S. Jovićević and N. Konjević, Stark broadening of Mg I and Mg II spectral lines and Debye shielding effect in laser induced plasma, *Spectrochim. Acta Part B* **85** 20–33 (2013) (ISSN: 0584-8547 DOI:10.1016/j.sab.2013.03.011 Impact factor: 3.194)
4. M. Cirisan and M. Cvejić and M.R. Gavrilović and S. Jovićević and N. Konjević and J.Hermann, Stark broadening measurement of Al II lines in a laser-induced plasma, *J. Quant. Spectrosc. Radiat. Transfer.* **133** 652–662 (2014) (ISSN: 0022-4073 DOI: 10.1016/j.jqsrt.2013.10.002 Impact factor: 2.768)
5. M. Cvejić and E. Stambulchik and M.R. Gavrilović and S. Jovićević and N. Konjević, Neutral lithium spectral line 460.28 nm with forbidden component for low temperature plasma diagnostics of laser-induced plasma, *Spectrochim. Acta Part B* **100** 86–97 (2014) (ISSN: 0584-8547 DOI: doi:10.1016/j.sab.2014.08.007 Impact factor: 3.176)
6. Irene L. Epstein and Marijana Gavrilović and Sonja Jovićević and Nikola Konjević and Yuri A. Lebedev and Alexey V.Tatarinov, The study of a homogeneous column of argon plasma at a pressure of 0.5 torr, generated by means of

the Beenackers cavity, *Eur. Phys. J. D* **68** 334–343 (2014) (ISSN: 1434-6060 DOI:10.1140/epjd/e2014-50182-7 Impact factor: 1.24)

7. Olivera Ciraj-Bjelac, Marijana Gavrilovic, Danijela Arandjic, Milan Vujovic, Predrag Bozovic, Radiation exposure during x-ray examinations in a large paediatric hospital in Serbia, *Radiation Protection Dosimetry* **165** 220–225 (2015) (ISSN: 0144-8420 DOI: 10.1093/rpd/ncv084 Impact factor: 0.916)

Изјава о ауторству

Име и презиме аутора Маријана Гавриловић

Број индекса 5024/2011

Изјављујем

да је докторска дисертација под насловом

**Узајамно дејство кавитационог мехура и зрачења плазме код пробоја
индукованог једним ласерским импулсом на мети у течности**

**(Interplay of cavitation bubble and plasma emission during single pulse laser
induced breakdown on submerged target)**

- резултат сопственог истраживачког рада;
- да дисертација у целини ни у деловима није била предложена за стицање друге дипломе према студијским програмима других високошколских установа;
- да су резултати коректно наведени и
- да нисам кршио/ла ауторска права и користио/ла интелектуалну својину других лица.

Потпис докторанда

У Београду, _____

Маријана Гавриловић

Изјава о истоветности штампане и електронске верзије докторског рада

Име и презиме аутора Маријана Гавриловић

Број индекса 5024/2011

Студијски програм Наноелектроника и фотоника

Наслов рада Узајамно дејство кавитационог мехура и зрачења плазме код пробоја индукованог једним ласерским импулсом на мети у течности (Interplay of cavitation bubble and plasma emission during single pulse laser induced breakdown on submerged target)

Ментор проф. Др Јован Цветић

Изјављујем да је штампана верзија мог докторског рада истоветна електронској верзији коју сам предао/ла ради похрањена у **Дигиталном репозиторијуму Универзитета у Београду**.

Дозвољавам да се објаве моји лични подаци везани за добијање академског назива доктора наука, као што су име и презиме, година и место рођења и датум одбране рада.

Ови лични подаци могу се објавити на мрежним страницама дигиталне библиотеке, у електронском каталогу и у публикацијама Универзитета у Београду.

Потпис докторанда

У Београду, _____

Маријана Гавриловић

Изјава о коришћењу

Овлашћујем Универзитетску библиотеку „Светозар Марковић“ да у Дигитални репозиторијум Универзитета у Београду унесе моју докторску дисертацију под насловом:

Узајамно дејство кавитационог мехура и зрачења плазме код пробоја индукованог једним ласерским импулсом на мети у течности

(Interplay of cavitation bubble and plasma emission during single pulse laser induced breakdown on submerged target)

која је моје ауторско дело.

Дисертацију са свим прилозима предао/ла сам у електронском формату погодном за трајно архивирање.

Моју докторску дисертацију похрањену у Дигиталном репозиторијуму Универзитета у Београду и доступну у отвореном приступу могу да користе сви који поштују одредбе садржане у одабраном типу лиценце Креативне заједнице (Creative Commons) за коју сам се одлучио/ла.

1. Ауторство (CC BY)
2. Ауторство – некомерцијално (CC BY-NC)
3. Ауторство – некомерцијално – без прерада (CC BY-NC-ND)
4. Ауторство – некомерцијално – делити под истим условима (CC BY-NC-SA)
5. Ауторство – без прерада (CC BY-ND)
6. Ауторство – делити под истим условима (CC BY-SA)

(Молимо да заокружите само једну од шест понуђених лиценци.
Кратак опис лиценци је саставни део ове изјаве).

Потпис докторанда

У Београду, _____

Маријана Тодоровић

1. **Ауторство.** Дозвољаваате умножавање, дистрибуцију и јавно саопштавање дела, и прераде, ако се наведе име аутора на начин одређен од стране аутора или даваоца лиценце, чак и у комерцијалне сврхе. Ово је најслободнија од свих лиценци.

2. **Ауторство – некомерцијално.** Дозвољаваате умножавање, дистрибуцију и јавно саопштавање дела, и прераде, ако се наведе име аутора на начин одређен од стране аутора или даваоца лиценце. Ова лиценца не дозвољава комерцијалну употребу дела.

3. **Ауторство – некомерцијално – без прерада.** Дозвољаваате умножавање, дистрибуцију и јавно саопштавање дела, без промена, преобликовања или употребе дела у свом делу, ако се наведе име аутора на начин одређен од стране аутора или даваоца лиценце. Ова лиценца не дозвољава комерцијалну употребу дела. У односу на све остале лиценце, овом лиценцом се ограничава највећи обим права коришћења дела.

4. **Ауторство – некомерцијално – делити под истим условима.** Дозвољаваате умножавање, дистрибуцију и јавно саопштавање дела, и прераде, ако се наведе име аутора на начин одређен од стране аутора или даваоца лиценце и ако се прерада дистрибуира под истом или сличном лиценцом. Ова лиценца не дозвољава комерцијалну употребу дела и прерада.

5. **Ауторство – без прерада.** Дозвољаваате умножавање, дистрибуцију и јавно саопштавање дела, без промена, преобликовања или употребе дела у свом делу, ако се наведе име аутора на начин одређен од стране аутора или даваоца лиценце. Ова лиценца дозвољава комерцијалну употребу дела.

6. **Ауторство – делити под истим условима.** Дозвољаваате умножавање, дистрибуцију и јавно саопштавање дела, и прераде, ако се наведе име аутора на начин одређен од стране аутора или даваоца лиценце и ако се прерада дистрибуира под истом или сличном лиценцом. Ова лиценца дозвољава комерцијалну употребу дела и прерада. Слична је софтверским лиценцама, односно лиценцама отвореног кода.